Spin Dynamics of ^{3}He and ^{3}He-^{4}He Mixtures

David Clubb, MPhys

Thesis submitted to the University of Nottingham
for the degree of Doctor of Philosophy, May 2003

Abstract

Experiments have been performed at high B/T to try to establish the existence and value of an anisotropy temperature T_a for pure ^{3}He, and for 6.2% and 0.7% ^{3}He-^{4}He mixtures. The anisotropy of diffusion in dilute Fermi gases as $T \rightarrow 0$ has been predicted, though experimental evidence for such anisotropy has not been universally accepted.

Finite size effects have required careful analysis of the theory of the cell for the 6.2% mixture. This alters the result as determined by the usual Leggett-Rice formula. Further investigation, beyond the scope of this thesis, is currently underway for the case of pure ^{3}He.

The possibility of using a quartz tuning fork as a viscometer has also been investigated. It is shown that tuning forks can be used field-independently above 3 mK in saturated ^{3}He-^{4}He mixtures, and to detect the superfluid A and B-phase transitions in pure ^{3}He. It is strongly suggested from the data that the tuning fork has great potential as a high-field viscometer; however further experiments are required to fully appreciate its useful range, in both normal and superfluids.

Acknowledgements

The three years I spent at Nottingham were hugely enjoyable for the most part, although hellishly difficult in places. Some people may breeze through their Ph.D's with a minimum of effort; I was one of those who thrived on the support given to me by friends, family and colleagues.

So the first thanks go to Dad and Cath, for giving me the "base camp" of somewhere to go, safe from the perils of Physics, and for all they've done in the past. However you can't hide from Physics for ever, and when you must turn to face this dreaded monster, there are some people who are suitably equipped to help you defeat it. These are the people in your research group, who slave with you night and day as your fridge demands ever-more sacrifices of Nitrogen, Helium and free time. Thus my huge thanks go to all in the group, and particularly to John, my supervisor. Equally responsible for the smooth running of experiments are the technical staff who create masterpieces, only for us to callously destroy them. My gratitude to you all, particularly Malcolm and Rick. The Helium suppliers are another vital link in the chain; for the most part this was John Dennis, though he sadly died soon after I finished at Nottingham.

Also qualified to roam the corridors of Physics Central are such mighty types as:

Andy Martin, boffin in the theory group, who also does a good line in accommodation for visiting friends; Laura, climber and wine connoisseur extraordinaire; Stu, resident AoE expert; Said, hardworking and putting the

rest of us to shame.

Luckily, when you manage to slip away from the department, there are many fine people to spend time with and to help rearrange your brain cells into a more relaxed pattern. The first people who you get into contact with are your housemates. If they're anything like mine were, you will never lack for tea or fun times. I will always appreciate the privilege of living with such types as Monster, Beck* and Emma, and of course Laurie. The next types are randomly connected, though you sometimes wonder how. Into this category I gratefully put Caz and Linda. But a large part of my free time was spent in the company of surfer types, and half of that was organising them on trips etc. So I hereby thank: Chad, The; Cheese, The; Surfer Bob; Cath; Blenko; Jim; Liz; Marie Trent; Mad Emma; Tux; Roop; Paul C; Andy W; Phil.

For friendship above and beyond the call of duty I call on Sara P (crazy, fun, and accommodation in London), Tom and Mav (the near-fatal call of the 18ft waves in Gran Canaria), Rick (muppet), and my twin brother Butt (for being me and me being him).

But most of all, this thesis is for Laurie. Housemate, partner in crime in Physics, teamaker, companion in trips to the peaks and beyond, best friend....I couldn't have done it without you.

Contents

Chapter 1

Introduction

1.1 General Ideas

The satisfactory understanding of experimental data for the transport properties of ^{3}He and ^{3}He-^{4}He mixtures has nominally been possible since the 1980's as the experimental conditions have become more attainable. The main difficulty involved with the study of spin-polarised Fermi liquids has been to create the high magnetic field and low temperature necessary to force the Fermi liquid out of the hydrodynamic (collision-dominated) regime. In fact, the low temperatures had been available for some time prior to the 1980's, but it was not until later that the more powerful ($\sim$ 10 Tesla) magnets, which are necessary for "brute force" polarisation, became more widely available.

^{3}He, and in particular its dilute solutions, can be considered to very closely resemble an ideal Fermi gas. If the Fermi gas is forced into the degenerate regime its Fermionic behaviour can be empirically demonstrated. Other Fermi systems (e.g. conduction electrons in metals, white dwarf stars) are difficult to examine across the whole region of $T < T_F < T$, as the Fermi temperature for a metal is typically $\sim 10^4$-10^5 K, while that for white dwarf stars is of the order 10^9 K (not to mention the difficulty in terms of physical accessibility!). Thus ^{3}He systems provide the opportunity to study experi-

mentally the behaviour of a Fermi gas as its temperature is reduced from far above its Fermi temperature, to far below it.

In order to properly examine the transport properties of these Fermi liquids, it is necessary to understand why they exhibit such extraordinary behaviour under certain conditions. Quantum theory provides the fundamental result that all particles are either fermions or bosons. In the classical regime their behaviour is very similar. This regime corresponds to the situation where the concentration is small compared with the quantum concentration:

$$n \ll n_Q \equiv \left(\frac{M\tau}{2\pi\hbar^2}\right)^{\frac{3}{2}}$$

where M is the particle mass and $\tau = k_B T$. If $n \geq n_Q$ the fluid is said to be in the quantum regime and is called a quantum fluid. In the quantum regime the differences between the behaviour of a fermion and a boson are marked, and both types of particle behave very differently to those in the classical regime. Fermi liquids have, comparatively, high kinetic energy, a low interparticle collision rate and exert a finite pressure on their confining walls even as $T \to 0$. A Bose liquid can have a very high population density in its lowest energy state as $T \to 0$. This low-energy population is called the Bose condensate and is the reason for the existence of, for example, the superfluid properties of ^{4}He at low temperature. Usually the quantum concentration remains fixed leaving the temperature as the most significant variable. Thus the temperature onset for the quantum regime can be defined by

$$\tau < \tau_0 \equiv \left(\frac{2\pi\hbar^2}{M}\right) n^{\frac{2}{3}}$$

Fermions and bosons are distinguished by their spin numbers, specifically, fermions have half-integer spin and bosons whole-integer spin. In a Fermionic gas, the Pauli exclusion principle limits the occupancy of each energy eigenstate to zero or one. At $T = 0$ all the eigenstates with energies less than the Fermi energy (ε_F) will be occupied by a single particle, whilst those above

the Fermi energy will be unoccupied. As the temperature of the experimental systems under consideration is finite, there is an average occupancy of nearly one just below ε_F and nearly zero just above it. This excludes most particles from the scattering process, except perhaps for the case of transverse diffusion. This special case will be covered in some depth at a later point (see section 2.3) but it is worth noting here that the NMR experiments detailed in this thesis were specifically designed to investigate further the controversial case of transverse spin transport.

The knowledge of the behaviour of fermions can be applied to the specific example of mixtures of ^{3}He -^{4}He. Solutions of ^{3}He in ^{4}He at low temperatures (< 0.5 K) exhibit behaviour much more closely related to that of pure ^{3}He than that of ^{4}He. At low mK temperatures, the superfluid ^{4}He is virtually devoid of excitations. It acts as an inert background in which the ^{3}He demonstrates the behaviour of delocalized slow particles with a large de Broglie wavelength ($\lambda = h/p$). The only excitations in the mixture are those due to the thermal motion of the ^{3}He particles. The viscosity, entropy and specific heat of the ^{4}He goes to zero and its contribution to the physical properties of the mixture is largely in terms of volume and to the effective mass (m^*) of the ^{3}He component. This effective mass is caused by the backflow of ^{4}He as the ^{3}He atom moves through it, and is about $2.3\mathrm{m}_3$, where m_3 is the mass of the ^{3}He atom (the quasiparticle interactions increase m^* as the ^{3}He concentration increases: $m^*/m = 1 + \frac{1}{3}F_1$, F_1 being a Landau Fermi-liquid parameter). This leads to the idea of the ^{3}He atom as a quasiparticle with different mass and energy to that of the free particle kinetic energy. This Fermi gas has a corresponding Fermi temperature which can be varied according to the concentration of the ^{3}He, thus enabling the momentum dependence of the quasiparticles to be investigated. With zero applied magnetic field the Fermi temperature varies approximately as:

$$T_F \simeq 2.6 x_3^{\frac{2}{3}} K$$

In the case of an experiment with a 6.2% ^{3}He concentration, this gives a Fermi temperature of $\sim$ 420 mK, indicating departures from degenerate behaviour above $\sim$ 40 mK, or $\sim$ 0.1 T_F [1]. Pure ^{3}He has a Fermi temperature of $\sim$ 1 K and a 0.5% mixture has $T_F \sim 29.2$ mK [2], so different concentrations may be used to examine the same phenomena at different temperatures.

Thus ^{3}He liquids can be used to confirm experimentally the theoretical predictions of the Fermi theory, which has had an impressive track record in its accuracy. There is, however, a far more complex and interesting regime in which to investigate ^{3}He liquids, namely that of a spin-polarised system. There are several different polarisation techniques available. The most conceptually simple technique is "brute force" , whereby a large magnetic field is applied. If the ratio of magnetic energy to thermal energy $\mu B/k_B T$ is high enough, the spins in the system will find it energetically favourable to align themselves in the direction of the field. Thus (assuming a field in the z-direction, where the positive z-direction is taken by convention to indicate an up-spin) the up-spins and down-spins will have different populations.

A very important parameter in spin-transport, whether polarised or not, is the relaxation time τ. This is the time between scattering events, and in the general case it increases with decreasing temperature. In a Fermi gas, the scattering particle requires an empty state to scatter into: the probability of there being such an empty state is proportional to $k_B T$. Likewise, the probability that a particle has sufficient thermal energy to become scattered is also proportional to $k_B T$. Thus the total probability of a scattering event occurring is proportional to the square of temperature:

$$\tau \propto T^{-2}$$

It is the scattering time which governs the mechanics of many transport properties, and it is easy to confirm experimentally this behaviour for such

factors as viscosity, diffusive thermal conductivity and longitudinal spin diffusion (strictly speaking, this is quantitatively true only for very dilute mixtures, further modifications to the simple theory need to be made for greater concentrations of ^{3}He. These are considered further in section 2.2).

Consider the Fermi gas in the case of high polarization; large departures from the behaviour of the unpolarized system are seen. At low temperatures the de Broglie wavelength becomes large in comparison with the particle interaction distance. Under circumstances of particle collision, the atomic wavefunctions of the particles overlap and, due to the Fermionic nature of the particles, the total wavefunction must be antisymmetric. Thus at low temperatures and low ^{3}He concentration the Pauli exclusion principle can operate due to the short range of the repulsive forces: this favours 's-wave' scattering which means that particles require spins of opposite sign to interact with one another. The amount of 'p-wave' scattering is dependent upon the momentum p_F of the particles, which is low in a dilute mixture $\left(p_F = \hbar\sqrt[3]{3\pi^2 n_3}\right)$. Polarising the system has the effect of removing one complete set of spins (e.g. down-spins). As opposite signs are needed for the favoured interaction this has the effect of drastically reducing the number of interactions which can take place, increasing the mean free path. Experiments have been performed [3] which show this effect as an increase in the viscosity of the ^{3}He, demonstrating the exclusion principle on a macroscopic level.

There are two further important consequences of applying a magnetic field to Fermi liquids. The first is the well-known Larmor precession, whereby the nuclear magnetic moments experience a torque which is perpendicular to both the external applied field and the magnetic moment itself. This causes the spin to precess about the external field (a more complete description of this process is given in section 2.1). The second effect is the appearance of an internal molecular field which is induced by the magnetization. This

internal field ($B_{int} = \omega_0\lambda$) arises from the quasiparticle interactions. The ^{3}He magnetic moments precess about the sum of the externally applied field and the internal molecular field. This precession is the called the spin rotation effect, and is responsible for the existence of spin waves. The spin rotation caused by the molecular field competes with three other effects. These are:

i. The rotation due to the instantaneous applied field

ii. The effect of the motion of the quasiparticles in the applied field gradient

iii. The effect of quasiparticle collisions.

The internal field can have a significant effect on the spin dynamics of the system. A "spin-rotation" parameter can be defined in such a way as to measure the magnitude of this effect. As the effects of spin precession are measured in the transverse plane, it is useful to consider separately the transverse relaxation time, thus the spin-rotation parameter can be written

$$\mu M_0 \equiv \Omega_{int}\tau_\perp \equiv -\lambda\omega_0\tau_\perp$$

Ω_{int} represents the precession frequency of the spin current about the sum of the molecular field and applied field; $\tau_\perp$ is the transverse quasiparticle relaxation time; M_0 is the bulk liquid magnetisation and $\mu = -\gamma^2\hbar\lambda\tau_\perp/\chi(0)$; $\chi(0)$ is the static susceptibility. λ is defined as a combination of Fermi-liquid parameters

$$\lambda = \frac{1}{1+F_0^a} - \frac{1}{1+\frac{1}{3}F_1^a}$$

The conventional Landau parameters

$$F_l^s \equiv N(0)f_l^s \qquad\qquad F_l^a \equiv N(0)f_l^a$$

demonstrate the link with concentration: the f function is related to the strengths of the quasiparticle interactions on the Fermi surface, and the $N(0)$ is related to the number density. ω_0 is the Larmor frequency, which is modified by the Fermi liquid parameters to give the 'internal' precession frequency Ω_{int}.

There are several observable consequences of the existence of an internal field, which become increasingly significant as the magnitude of the spin-rotation parameter increases. In practice these phenomena require that the Landau molecular field $\lambda\omega$ exceeds the transverse relaxation time (or that $\mu M_0 \geq 1$) to be observed. This regime is known as the "collisionless regime", as the predominant effect on the quasiparticles is from the molecular field rather than quasiparticle collision. In the hydrodynamic regime ($\mu M_0 \leq 1$), the rotation of spin is sufficiently small that there is a negligible result of spin rotation before quasiparticle-quasiparticle collisions restore thermal and magnetic equilibrium. The observable consequences of the molecular field include the Leggett-Rice effect (which is responsible for the anomalous decay of spin-echoes) and the creation of spin waves, which are propagating waves of spin angular momentum or magnetisation [4]. Spin waves are also known as Silin spin waves, after the person who postulated their existence under an applied field at low temperatures [5]. Silin showed that applying a magnetic field to ^{3}He allowed the propagation of collisionless transverse spin waves. Further work by several workers [6], [7], [8] developed further the theory, demonstrating that the molecular field rotates a spin current, arising from a gradient in transverse magnetisation, into a direction perpendicular to the gradient

The anomalous behaviour of spin-echoes relates specifically to the non-exponential decay of the echo, as opposed to the exponential behaviour of the hydrodynamic regime; and to the phase shift of the echo. These effects can be experimentally measured to give a value for the diffusion coefficient and the spin-rotation parameter. The spectrum of the spin wave modes can also be used to determine the spin rotation parameter and diffusion coefficient. The Landau field is proportional to the polarisation, so a high degree of polarisation should produce a near-maximum manifestation of these unusual types of behaviour. Further details of spin waves and spin echoes are provided in

sections 2.5 and 2.6 respectively.

As an aside, it should be noted that a similar type of effect to the rotation caused by the molecular field can also be observed in polarised but non-degenerate Bose or Fermi gases. This is termed "identical spin rotation", and requires that the product of the fractional polarisation and the de Broglie wavelength be greater than the range of the interatomic interaction.

The relevant point at this stage of the discussion is how the information provided by spin echoes and spin waves can be used to derive information about the spin diffusion. Leggett and Rice [7] predicted that the effect of the spin current upon the diffusion coefficient, measured in a spin-echo experiment with small angle tipping pulses, would be to cause the apparent diffusion coefficient (D_e, eq. 1.1), determined from the attenuation of the spin echoes, to have a maximum at which $\omega_0\tau_D \sim 1$. In further work [8], Leggett suggested a non-exponential spin echo attenuation which depended on initial pulse angle and external field (see section 4.1). Further consequences of the non-linearities predicted by Leggett include the existence of weakly-damped spin waves, and the presence of Multiple Spin Echoes (MSE's). Despite the observation of MSE's in solid and superfluid ^{3}He in the 70's, it was not until 1984 [9] when MSE's were observed in normal ^{3}He. Observations of this phenomenon in ^{3}He-^{4}He mixtures followed several years later [10]. Both spin waves and MSE's are important proof of the non-linearities of the system being studied, and both were observed during experimental runs in this project.

The work in this thesis is particularly concerned with the phenomenon which has caused the most controversy in the topic, namely the anisotropy of spin diffusion as $T \rightarrow 0$, originally postulated for dilute Fermi gases in 1985 by Meyerovich [11].

In terms of quasiparticle relaxation, this means that the evolution of the gra-

dient in spin density magnitude is governed by the longitudinal relaxation time, which is predicted to decrease as T^{-2} in line with Fermi liquid theory. The transverse relaxation time, which determines the rate of decay of the transverse component of spin density, is predicted to reach a low-temperature limit, beyond which the quasiparticle lifetime, and hence diffusion coefficient, remains constant ($D_{||} \propto \tau_{||}$ and $D_{\perp} \propto \tau_{\perp}$). The prediction of the relaxation time of the transverse spins $\tau_{\perp}$ to saturate was made by Meyerovich and Musaelian [12]. This saturation varies as $1/(T_a^2 + T^2)$, where T_a is called the anisotropy temperature. Conversely, Fomin [13] has argued that there is no saturation of the relaxation times at $T = 0$. The logical extension of Fomin's argument is that the excitations in the system become increasingly undamped as $T \rightarrow 0$, precluding the existence of an anisotropy temperature. As there has been no extension of the theory to include finite temperatures, it is impossible to test the theory explicitly (it has, however, been suggested recently that the two theories would be compatible at $T > 0$ [14]). An experiment which detected no saturation of diffusion as $T \rightarrow 0$ would demonstrate an implicit agreement with Fomin's theory. It is symptomatic of the controversy of this subject that there should be experimental evidence supporting both contrary theories; further experimental and theoretical work needs to be pursued to resolve this argument, and the work contained herein is a part of this ongoing study.

1.2 Previous Experiments

The background to the work contained in this thesis is heavily influenced by the results obtained by other groups performing similar experiments. Although the experimental conditions used herein were different to those previously used, the differences are largely in terms of the magnitude of the applied field and the temperature range investigated. It is, therefore, very useful to provide an overview of the results obtained by others working in

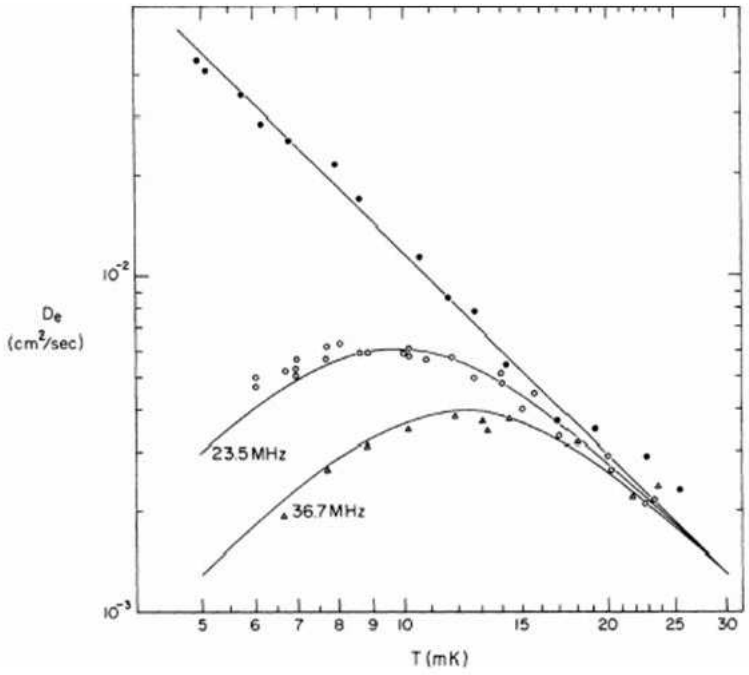

Figure 1.1: First experimental confirmation of the Leggett-Rice effect. Values of the effective diffusion coefficient D_e. Open circles and triangles correspond to $18^0-\pi-$echo sequences at different fields, the solid line is calculated from Leggett's equation. Filled circles represent the diffusion coefficient measured in 90^0-180^0-echo sequence to demonstrate the dependence of the Leggett-Rice effect on tipping angle (after Corruccini *et al.* [15])

the same topic.

It was not until several years after the prediction by Leggett and Rice [7], of distinctive non-linear behaviour under certain conditions, that the first experiments were performed to verify the existence of the Leggett-Rice effect. In 1971, using spin-echo techniques (see section 2.6), the most common form of experiment for spin-diffusion experiments, Corruccini *et al.* [15] produced the first experimental confirmation of the Leggett-Rice effect in pure ^{3}He. Their data showed a maximum for the effective diffusion coefficient D_e (eq. 1.1) at the temperature for which $\omega_0\tau_D \sim 1$, a fundamental prediction of the Leggett-Rice effect (see fig. 1.1). The effective diffusion coefficient is a measure of the transverse diffusion rate, modified by the spin-rotation parameter, μM_0, which is itself a measure of the scale of departure from diffusion in the collision-dominated regime.

$$D_e = \frac{D_\perp}{1 + (\mu M cos\theta)^2} \tag{1.1}$$

Here θ is the tipping angle, which can take any value in this experiment (for much higher polarisations other effects may render the spin-echo equations invalid). The shape of the curves in the figure can easily be explained by the equation above. Both $D_\perp$ and μM_0 are proportional to T^{-2}, so the curve follows T^{-2} whilst $\mu M_0 < 1$, and follows T^2 as μM_0 increases significantly beyond unity. There is no sign in figure 1.1 that the effective diffusion coefficient D_e (and hence the transverse relaxation time) saturates at the lowest temperatures. The magnetic field of 1.15 T was insufficient to create the large values of μM_0 required to view such a saturation; nonetheless, the separation of the curves for the effective diffusion coefficient and the hydrodynamic diffusion coefficient $D_\perp$ is a demonstration of the Leggett-Rice effect. Qualitative confirmation of the Leggett-Rice effect in saturated ^{3}He-^{4}He mixtures followed shortly thereafter [16].

The second common method of determining the diffusion coefficient is by measuring the damping of spin wave modes. This is the method used by Vermeulen and Roni [17]. In principle the experiments performed at Nottingham could also use this technique to confirm the results obtained from spin-echo analysis. There were, however, experimental reasons why this was not possible. These reasons are described in section 4.2.2.

Twenty years after Silin's prediction, the first experiments to show spin waves in pure ^{3}He [18], [19] took place, with equivalent measurements in ^{3}He-^{4}He taking place shortly thereafter [20]. A summary of the results of previous experiments is listed in table 1.1.

The wide range of possible measured and calculated values of T_a are an indication of the controversy which this topic can still arouse, with work on the experimental and theoretical aspects ongoing.

Reference	x_3	Field (T)	Method	T_a(10 T)
Candela *et al.* [3]	6.3×10^{-4}	7.96	spin waves	< 7.5mK[a]
Nunes *et al.* [21]	1.94×10^{-4}	9.2	spin echoes	< 5.5mK
Mullin *et al.* [22]	dilute limit		theory	2.5mK[b]
Wei *et al.* [23]	1	8.0	spin echoes	20.5mK[a]
	10.0×10^{-4}			9.1mK
Ager *et al.* [24]	38.0×10^{-4}	8.8	spin echoes	14.8mK
	64.0×10^{-4}			21.6mK
Owers-Bradley *et al.* [25]	62.0×10^{-4}	11.3	spin echoes	12.1mK
Candela *et al.* [26]	1	11.3	spin echoes	13.2mK
Vermeulen *et al.* [17]	93.0×10^{-4}	5×10.54[c]	spin waves	< 3mK
Akimoto *et al.* [27]	9.0×10^{-4}	14.74	spin echoes	11.5mK[d]
Buu *et al.* [14]	62.0×10^{-4}	11.3	spin echoes	5.5mK

Table 1.1: (a) The data of references [3] and [23] are compared by Candela *et al* [28] to give the values indicated. (b) The calculation of Mullin *et al.* [22] is limited to s-wave collisions, and is hence valid only in dilute mixtures (c) The experiment of Vermeulen *et al.* [17] uses a technique which enhances the polarisation by a factor 5 from its equilibrium value. (d) The value of T_a here is obtained from a fit of the data assuming $\Omega_{int}\tau_\perp \propto 1/(T^2 + T_a^2)$, and not from the reference itself.

1.3 Scope of Thesis

This thesis presents data obtained during several experiments to try to determine the existence and value of an anisotropy temperature T_a in the Fermi liquids ^{3}He, and two different concentrations of ^{3}He-^{4}He. The magnetic field used ($\sim$ 11 T) was greater than had previously been applied in other like experiments at low temperatures, and as T_a is expected to scale with the polarisation, it was expected that data could be produced to clarify the argument. The subject is fairly complicated, and a basic understanding of the Fermi liquid theory is required. The theory behind the two investigative techniques employed, spin waves and spin echoes, is also presented: these subjects are covered in Chapter 2. In addition, work performed over the course of this project has indicated that the initial method of analysis used on the data was incomplete. An overview of the reasons for this, and of the methods used to reanalyse the data, is included here.

The experimental set-up and the NMR techniques used are detailed in Chap-

ter 3. The analysis of the data obtained from the original (cylindrical) cell was relatively complicated, and it was therefore decided to alter the experiment to use a spherical quartz cell to simplify the analysis. The helium reservoir/thermometry chamber was also modified to allow for more straightforward repairs to the cell on breakage. Despite several attempts to assemble this experiment the results were ultimately unsuccessful; the design and the reasons for the lack of success are also explained here. The data obtained from the cylindrical cell, in pure ^{3}He, 6.2% ^{3}He-^{4}He and 0.7% ^{3}He-^{4}He, are presented in Chapter 4, along with both the original analysis of the data, and that produced by the numerical simulations of the exact experimental conditions for the 6.2% mixture.

The second series of experiments performed was to investigate the suitability of quartz tuning forks and plastic film capacitors as thermometers. There are considerable difficulties associated with thermometry at low-millikelvin temperatures and high (> 10 T) magnetic fields, and any increase in the choice available to experimentalists would be advantageous. A review of some of the current available choices of thermometer is presented in Chapter 5, along with the data collected and its analysis.

Chapter 6 concludes the thesis, presents a discussion of the results, and describes some possible directions for future work.

Chapter 2

Theory

2.1 NMR

Nuclear magnetic resonance (NMR) is a very useful experimental tool which makes use of the intrinsic spin angular momentum of atomic nuclei. On application of an external magnetic field, an interaction occurs between the nuclear magnetic moment and the field, which gives rise to a splitting of the associated nuclear energy states. The energy separation of the two states is known as the Zeeman energy. Transitions between these energy states can be induced by absorption and emission of photons of the correct frequency. The nuclear magnetic moments also interact with other magnetic nuclei and electrons, and this can be used to build up a picture of the magnetic environment of the sample. The use of NMR is a major theme in this thesis, and it is useful to provide a basic overview of the fundamental principles.

Nuclei with non-zero nuclear spin quantum numbers possess angular momentum, the magnitude of which is determined by the value of the spin quantum number I:

$$P = \hbar \left[I \left(I + 1 \right) \right]^{1/2}$$

Since the nucleus has a charge and angular momentum, it creates a magnetic field known as the nuclear magnetic moment μ, typically with a value of several mT. The ratio of the magnetic moment to the angular momentum

(**P**) is called the magnetogyric ratio, γ. Each species of nucleus has a unique magnetogyric ratio associated with it:

$$\mu = \gamma\hbar\mathbf{I} = \gamma\mathbf{J}$$

where $|\mathbf{I}|$ and its component I_Z (along, say, the z-axis) are related to the quantum numbers I and m by

$$|\mathbf{I}|^2 = I(I+1)$$

$$I_Z = m_I$$

where $\mathbf{I}$ is the dimensionless angular momentum operator, and $m_I = -I, -I+1, ..., I-1, I$. A spin-1/2 particle such as ^{3}He has two quantum states which relate to $m = +1/2$ and $m = -1/2$ (spin-up and spin-down). In the absence of a magnetic field, the energy of an isolated nucleus is independent of the quantum number m_I. However, in the presence of an applied external field $\mathbf{B}_0$ (which is conventionally directed along the $z-$axis) the states lose their degeneracy, as each state now corresponds to a different energy

$$E = \gamma m_I \hbar \mathbf{B}_0$$

In a sample containing a large number of spins, a net magnetisation $\mathbf{M}$ can be induced. The populations of the two energy levels are proportional to $\exp(-E/k_BT)$, and for low temperatures and high fields the polarisation, and hence magnetisation, can reach a significant value (100% for low concentrations). For ^{3}He the difference between energy levels is given by

$$\Delta E = \gamma\hbar\mathbf{B}_0 = \hbar\omega_L$$

showing the relationship between the energy gap and the magnetogyric ratio. The Larmor frequency $\omega_L = \gamma\mathbf{B}_0$, and this is the frequency required to excite the transition between the two energy states. For the experiments carried out during this work the field used was 11.3 T, corresponding to a Larmor

frequency of 367 MHz. In order to derive the Bloch equations, which are used as the starting point for describing the evolution of magnetisation in a sample, the behaviour of a macroscopic sample needs to be considered. The particles are considered to be identical, and the magnetisation $\mathbf{M}$ is the resultant of the nuclear magnetic moments μ:

$$\mathbf{M} = \sum_j \mu_j = \gamma \mathbf{P}$$

For a macroscopic system, classical mechanics can be used to describe the effect of the applied field $\mathbf{B}_0$:

$$\text{Torque} = \frac{d\mathbf{P}}{dt} = \mathbf{M} \times \mathbf{B}_0$$

Thus, the time variation of magnetisation can be written

$$\frac{d\mathbf{M}}{dt} = \gamma \mathbf{M} \times \mathbf{B}_0 \tag{2.1}$$

For spin -1/2 nuclei, the magnitude of the magnetisation can be calculated directly [29], using an equation analogous to the Curie equation:

$$M_0 = \frac{1}{4} \frac{N \left(\gamma \hbar\right)^2 B_0}{k_B T}$$

The equation of motion representing the magnetisation must be modified to allow for thermal equilibrium (relaxation). Bloch's assumption [30], was that the magnetisation would recover with an exponential timeframe, but the longitudinal and transverse relaxation processes were given different time constants, T_1 and T_2 respectively. The separate equations are written

$$\frac{dM_z}{dt} = -\frac{(M_z - M_0)}{T_1} \tag{2.2}$$

$$\frac{dM_{xy}}{dt} = -\frac{M_{xy}}{T_2} \tag{2.3}$$

T_1 is also known as the spin-lattice relaxation time, with T_2 being the spin-spin relaxation time. The rate of recovery of the magnetisation along the $z-$axis, M_Z, is given by

$$M_z = M_0 \left(1 - e^{-t/T_1}\right)$$

defining T_1 as the time required to change M_Z by a factor e. The time constant T_2 governing the relaxation of magnetisation along the $x-y$ plane is determined by

$$M_{xy} = M_{xy_0}\left(e^{-t/T_2}\right)$$

The value of T_2 is always the same or less than that of T_1.

In an NMR experiment, an r.f. field is applied to the sample. The r.f. field has a frequency which corresponds to the Larmor frequency, in order to excite changes in the energy state of the atoms. The field can be written $2B_1\cos(\omega t)$, and consists of two counter-rotating components, of angular velocity ω. The component rotating opposite to the Larmor frequency can be neglected, due to the relative lack of influence it exerts on the energy of the atoms. The resultant field acting on the sample is

$$\mathbf{B} = B_1\cos(\omega t)\mathbf{i} - B_1\sin(\omega t)\mathbf{j} + B_0\mathbf{k} \tag{2.4}$$

The Bloch equations derive from combining equation 2.1 with equations 2.2, 2.3 and 2.4:

$$\frac{dM_z}{dt} = \gamma\left[B_1\cos(\omega t)M_y + B_1\sin(\omega t)M_x\right] - \frac{(M_z - M_0)}{T_1}$$

$$\frac{dM_{xy}}{dt} = \gamma\left[B_1\sin(\omega t)M_z + B_0M_y\right] - \frac{M_{xy}}{T_2} \tag{2.5}$$

The Bloch equations govern how the magnetisation in the cell evolves after being displaced from its equilibrium position. Under application of the relevant boundary conditions, further relationships, which enable data to be correctly analysed, can be deduced. The modification of the Bloch equations by Leggett and others, to allow for actual experimental conditions, is covered in section 2.4.

2.2 Fermi Liquids

One of the reasons for carrying out experiments in ^{3}He-^{4}He mixtures is because the thermodynamic properties of dilute mixtures can be calculated in a straightforward way using statistical mechanics. The Landau model of such a system is that of the Fermi gas theory, modified in several ways. For dilute mixtures the ^{4}He acts as a background with phonon and roton excitations (which are essentially non-existent below 100 mK), with a ^{3}He impurity depending on the concentration of the mixture x. The first modification made was to consider the ^{3}He atoms as a weakly-interacting gas of quasiparticles, with the ^{4}He contributing only to the effective mass of the quasiparticle.

Strongly-interacting fluids are more complicated, and this was acknowledged by Landau who included a second modification to the Fermi gas theory. This was an interaction which depends upon the configuration of nearby atoms. The interaction of those nearby atoms changes the overall energy of the system of volume V by an amount

$$\delta U = V \int \epsilon_\sigma(p) \delta n_\sigma(p) d\tau$$

for a quasiparticle of spin σ, momentum p and energy ϵ, with $d\tau = d^3p/h^3$. The quasiparticle distribution $n_\sigma(p)$ is the usual ideal gas distribution function

$$n_\sigma(p) = \frac{1}{\exp\left[\left(\epsilon_\sigma(p) - \mu_3\right)/k_B T\right] + 1}$$

where μ_3 is the ^{3}He chemical potential and δn_σ is the shift in distribution function attributed to the interactions. The change in energy for a momentum p due to all other excitations can be written

$$\delta\epsilon_\sigma(p) = V \sum_{\sigma'} f_{\sigma\sigma'}(p, p') \delta n_{\sigma'}(p') d\tau'$$

where the function $f\,(p, p')$ is the Landau forward scattering amplitude. This corresponds to the change in one quasiparticle energy level resulting from

the change in occupation of all other energy levels. The Landau model is accurate enough in ^{3}He that, once the Landau parameters F_n^a (which can be determined from the sound velocity, heat capacity and spin susceptibility) are known, predictions can be made with great accuracy regarding many different properties of the liquid. An example of this is the diffusion coefficient D which, at low field (such that $\Omega_{int}\tau_\perp \ll 1$), can be calculated using equation 2.6:

$$D = \frac{1}{3} v_F^2 \left(1 + F_0^a\right) \tau_D \tag{2.6}$$

Relevant modifiers, to the mass, and to the value of the Landau parameters, allow a similar analysis for mixtures of ^{3}He-^{4}He. Further successes of Landau's theory were the predictions of a new form of sound (zero sound) and spin waves (see section 2.4).

^{3}He-^{4}He is the only neutral Fermion gas which can be cooled below the Fermi temperature without condensing into its ground state. This means that the theoretical predictions can be directly compared with experiment. The fact that ^{3}He has spin, which lends itself to the use of NMR, and that it can be polarised with relative ease, are additional advantages. The rest of the chapter deals with some of the consequences of this Fermionic behaviour in the regimes of interest, and outlines some of the interesting non-linear behaviour which occurs as a result.

2.2.1 Spin-polarized Fermi Liquids

When a magnetic field B is applied to a degenerate gas of fermions it tends to polarise the gas; that is, the number of spins parallel to B increase at the expense of those antiparallel (the equivalent of this behaviour in metals is known as Pauli paramagnetism). The energy supplied to each spin is μB, and at the Fermi surface the energy difference between the spin distributions is $\Delta E = 2\mu B$. On equilibrium there is now an energy difference between the two sets of spins which gives a net resultant magnetisation [32], assuming

$T \ll T_F$

$$M = \mu^2 B D(\varepsilon_F)$$

where $D(\varepsilon_F)$ is the density of states (the number of eigenstates per unit energy interval $d\varepsilon$). For a fully polarised gas there is no $s-$wave interaction; this has an impact on several parameters, for example, the effective mass m^* which decreases to ~ 0.92 from 2.3, and the Landau parameters which scale by a comparable factor [32]. Both pure ^{3}He, and its mixtures with ^{4}He, exhibit rich non-linear effects under conditions of full or partial polarisation. These effects include spin waves, multiple spin echoes and zero sound.

To completely polarise ^{3}He by brute force requires magnetic fields which are presently unattainable ($\sim$ 400 T [33]). Alternative methods include:

Rapidly melting a highly polarised solid sample (used in, for example, lung-imaging MRI systems)
Optical polarisation (also used in lung-imaging techniques)
Circulating ^{3}He in ^{4}He in a magnetic field (as used by Roni and Vermeulen [34])

The first effect of the application of a polarising magnetic field, which is responsible for the existence of the other non-linear effects, is the presence of a molecular field. This is a result of the strong magnetic interactions between ^{3}He quasiparticles. The molecular field exists in any polarised, strongly interacting Fermi system [8]. Each spin will now precess around the total field, which is a vector sum of the external and molecular fields.

Meyerovich [11] states that the cross-over between the strongly and weakly-interacting gas occurs at $x \approx 0.01$. In practice, the cross-over is a gradual one, and, despite the presence of slight interactions for concentrated mixtures, the Landau model is still a reasonable first approximation. For a dilute mixture,

the quasiparticles have an energy

$$\epsilon = -E_3(x) + p^2/2m \tag{2.7}$$

For a quasiparticle in a magnetic field B in the $z-$direction, the energy is modified from that given by equation 2.7 to

$$\epsilon_\sigma(p) = -E_3 + \frac{p^2}{2m} - \hbar\gamma B\sigma_z \tag{2.8}$$

where $\sigma_z = \pm\frac{1}{2}$. On application of a magnetic field the energy of the up-spin states is lowered with respect to the down-spin states. To equalize the chemical potential of $\uparrow$and$\downarrow$ states, the $\downarrow$ spins flip to $\uparrow$, thus the populations of states differ with $\mathrm{n}_+ > n_-$. Equation 2.8 becomes

$$\epsilon_\sigma(p) = -E_3 + \frac{p^2}{2m} \mp \frac{\hbar\gamma B}{2}$$

It has already been stated that for weakly-interacting Fermi liquids $p-$wave interactions (i.e. parallel spins) are much weaker than $s-$wave (antiparallel) interactions. For a system with a polarisation of 100% this raises an interesting point: the transport properties (e.g. mean free path, viscosity) which depend upon the scattering probability are substantially increased, and only limited by the $p-$wave scattering cross-section.

The knowledge of the behaviour of spin-polarised Fermi liquids is important in understanding the spin-transport mechanisms for the systems examined over the course of this work. The following sections provide details of the spin-transport mechanisms encountered.

2.3 Spin Diffusion

The spin diffusion coefficient D of ^{3}He-^{4}He mixtures was first measured in 1959 [35]. At the temperatures investigated (> 500 mK) there are several features which can be determined. Firstly, above ~ 1 K the diffusion coefficients of mixtures of different concentration become equal, indicating that the thermal excitations in the ^{4}He have become the dominant scattering mechanism.

Below 1 K and above $\sim 2T_F$, the diffusion coefficient varies proportional to n_3^{-1}, indicating the scattering mechanism is now ^{3}He-^{3}He events [36]. Boltzmann statistics can be used to analyse the behaviour of the system in this regime. Further consideration of the Landau model led Hone [37] to predict a $D \sim 1/T^2$ dependence for ^{3}He for $T \ll 50$ mK, a prediction which was later confirmed experimentally [38].

It was Meyerovich [11] who, in 1985, showed that linear spin diffusion in highly polarised systems could be anisotropic. If the components of the transverse magnetisation are grouped into a complex number, $m_- = m_x - im_y$, and M_z is the spin density along the polarisation, the corresponding spin currents, arising from small deviations from equilibrium, can be written

$$\mathbf{J}_z = -D_{||}\nabla M_z \qquad\qquad \mathbf{J}_- = -\frac{D_\perp}{1+(\mu M_0)^2}\nabla m_-$$

The two diffusion coefficients are proportional to distinct relaxation times, $D_{||} \propto \tau_{||}$ and $D_\perp \propto \tau_\perp$. As the temperature of a polarised ^{3}He system decreases, so $D_{||}$ is expected to increase as T^{-2}, in line with the predictions of Fermi theory. This increase is mirrored in other transport properties, e.g. viscosity and diffusive thermal conductivity. $D_\perp$ diverges from the T^{-2} relationship, and this divergence can be accounted for in several ways. Experimentally, it could be due to finite size effects (where the effect of restricted diffusion can be to mimic the effects of a saturation of the transverse relaxation time [39]), or, for example, second-order field gradients in the experimental cell. The important physical reason, however, is due to non-linear effects (e.g. the Leggett-Rice effect), though the precise behaviour of $D_\perp$ as $T \to 0$ is still very much in dispute (see section 2.3.2).

2.3.1 Longitudinal Diffusion $D_{||}$

Longitudinal diffusion refers to the case where the gradient in magnetisation, which is responsible for driving the diffusion of spins, is parallel to the

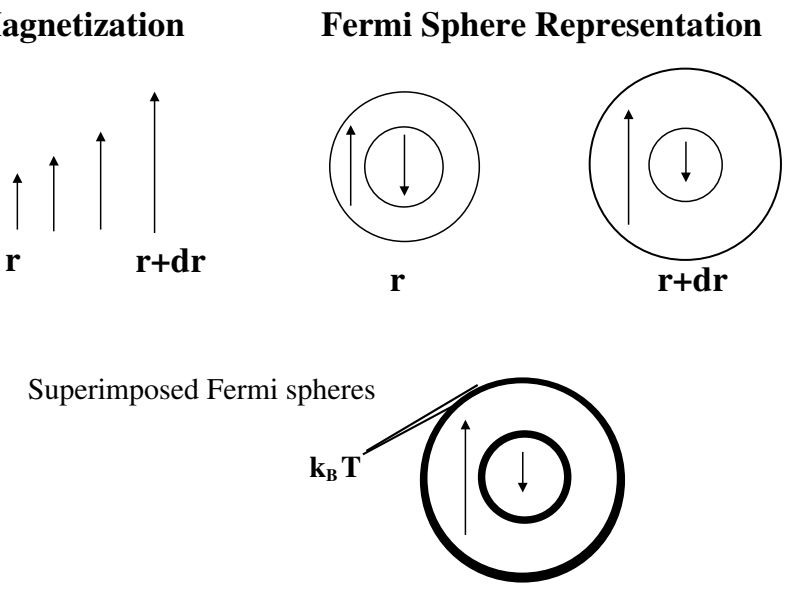

Figure 2.1: Fermi sphere representation of longitudinal spin diffusion

magnetisation. Although the mechanics of longitudinal spin transport are relatively straightforward, it is useful to present them, as they help with understanding the situation for transverse diffusion.

The magnetisation of the spins can be written as $\mathbf{M}=M\hat{\mathbf{e}}$, with M representing the magnitude of the magnetisation and $\hat{\mathbf{e}}$ its direction. Thus

$$\nabla\mathbf{M} = \hat{\mathbf{e}}\nabla M + M\nabla\hat{\mathbf{e}} \tag{2.9}$$

The first of these terms describes the longitudinal spin current whilst the second denotes the transverse current. The longitudinal term contains a varying magnitude, but has a direction which is static and parallel to $\mathbf{M}$. The longitudinal case is considered here, and the use of Fermi spheres (see fig. 2.1) can help with the visualisation of the transport processes. If the magnetisation of the ^{3}He is decreased by, for example, a $\pi/2$ pulse, a gradient in the magnitude of the magnetisation across the cell, from **r** to **r+dr,** can be created. The resultant magnetisation magnitude at any point in the cell can be considered to be a combination of up-spins and down-spins, both of which will diffuse at the same rate, despite having different Fermi velocities [40]. At

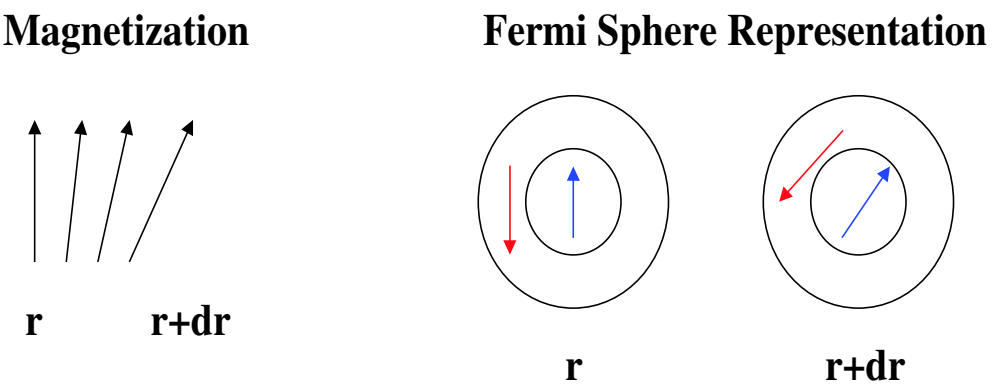

Figure 2.2: Fermi sphere representation of transverse spin diffusion

position **r**, the up-spin sphere is slightly larger than the down-spin sphere. At **r+dr**, the up-spin sphere is significantly greater in size than the down-spin sphere. When the two spheres are superimposed a narrow annular region of width $\sim k_B T$ can be seen, which represents the difference between the two up-spin spheres at different points across the cell. Any spin in this region is unstable when it reaches **r+dr** and must scatter to regain its equilibrium. At low momenta (low mixture concentration or low temperature) any scattering must take place between quasiparticles of opposite spin; hence there is also the factor $k_B T$ from the difference in sizes of the down-spin fermi spheres across the cell. Spins from low energy states deep in the Fermi surface will remain in equilibrium and will not scatter. The quasiparticle lifetime is therefore a product of the probability that there is a spin in the region $k_B T$ to scatter initially, and the probability of there being an empty state in the corresponding region $k_B T$ at **r+dr** to scatter into; namely $\tau_{||} \propto D_{||} \propto T^{-2}$.

2.3.2 Transverse Diffusion $D_\perp$

From equation 2.9, the gradient in transverse magnetisation is denoted by the second part of the r.h.s., $M\nabla\hat{\mathbf{e}}$; that is, constant magnitude but varying direction. Again, the Fermi sphere formalism can be useful to give a simplistic view of the mechanism of transport (fig. 2.2). When the spins are 'tipped' across the whole cell they start to precess at different rates across that cell

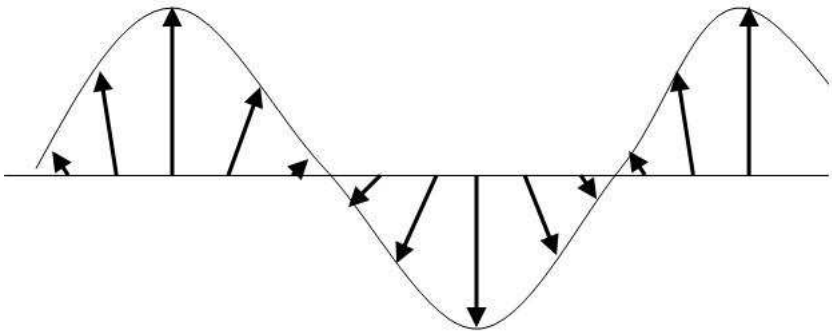

Figure 2.3: For a uniform displacement from equilibrium, the spins form a spiral under a gradient field

due to the applied field gradient. The rate of precession is determined by the applied magnetic field B and the gyromagnetic ratio γ, and is given by the product $\omega = \gamma B$. With different rates of precession, the tips of the spins tend to trace out a spiral (fig. 2.3). A transverse spin current along the direction $\nabla\hat{\mathbf{e}}$, perpendicular to $\mathbf{M}$, is formed. As demonstrated in figure 2.2, the direction of magnetisation is different between spins at different displacements from the origin of coordinates in the experimental cell. This is more usefully portrayed as the quasiparticle being in a superposition of up and down-spin states. Thus spins diffusing between $\mathbf{r}$ and $\mathbf{r}+\mathbf{dr}$ become out of equilibrium, and must scatter to return to local equilibrium. In the picture of Meyerovich and Mullin, the whole of the phase space between the two Fermi spheres is available for this, and thus the relaxation time for the transverse scattering has the potential to be far smaller than that of the longitudinal scattering mechanism. It is only in the limit of low polarisation, where the Fermi spheres for both spin-up and spin-down are approximately the same

size, that there is no appreciable difference between the two relaxation times.

The real controversy comes for the limit as $T \rightarrow 0$. In this regime, the prediction of Meyerovich [12], and Mullin and Jeon [41], is for the diffusion coefficient to saturate as $T \rightarrow 0$. They state that the transverse relaxation time should vary as $\tau_\perp \propto 1/(T_a^2 + T^2)$, where T_a is the so-called 'anisotropy temperature'. The contradictory theory of Fomin [13] suggests that the diffusion should become increasingly undamped, that is, $\tau_\perp \propto 1/T^2$ as $T \rightarrow 0$. Fomin derives the equations of spin dynamics directly for $T = 0$, using the condition that variations of the Landau field are slow, and of low amplitude. His conclusion is that the equations governing the evolution of spin waves do not contain any dissipative terms, and hence that there is no damping of spin waves at $T = 0$. The model produced is one whereby the quasiparticle does not scatter between points in the cell, but changes its momentum adiabatically as it moves through the cell. Fomin argues, by symmetry, that a Fermi liquid with 'frozen' (constant) polarisation is similar to an isotropic ferromagnet, and that the spin dynamics are governed by the analogous equations for a ferromagnet. As work has yet to be performed on extending Fomin's theory to finite temperatures, there is considerable difficulty with checking his hypothesis experimentally.

The first experiments to observe the saturation of the diffusion coefficient were carried out in pure ^{3}He. This was because it was believed that the anisotropy temperature scaled with the applied field, and also with the molecular field (which is higher in pure ^{3}He). The enhancement of the anisotropy temperature was put at a factor 3.3 by Wei *et al.* [23], though, as this value depends on knowing the Fermi liquid parameter F_0^a with a high degree of accuracy, its magnitude is open to some question. It has also been pointed out [42] that the factor 3.3, deriving from the Fermi liquid parameter, has already been taken into account for the effective mass, and that it is therefore being counted twice for the above argument. Krotkov *et al.* [43] suggest that

the attenuation onset for the case of damping of spin-wave modes should occur at higher temperatures for strong polarisations, lending weight to the experimental evidence of Vermeulen and Roni, which does not detect damping of spin-wave modes despite a very high level of polarisation. They also state that the value of the molecular field is further increased by polarisation, which scales by the ratio M/M_0, with M the absolute value of the static magnetisation, and M_0 the equilibrium magnetisation. The current state of experimental results demonstrates no significant enhancement of the anisotropy temperature due to the molecular field (see table 1.1).

The equation of spin-motion is covered in the next section, though the work performed on its analysis assumes the inclusion of a damping term, in line with Meyerovich's model.

2.4 The Equation of Spin-Motion

It has already been shown (section 2.1) that the evolution of magnetisation in the cell can be calculated using the Bloch equations. These equations do not, however, allow for the diffusion of spin-bearing particles. In 1956, Torrey [44] included the effects of diffusion due to a field gradient. This allowed for the displacement of the magnetisation from equilibrium, and the possibility of building up significant magnetisation gradients from the cumulative effects of spin precession. Assuming the validity of the classical diffusion equation

$$D\nabla^2 M + \left(\frac{\partial M}{\partial t}\right) + \gamma\left(M \times H\right) = 0 \tag{2.10}$$

he derived an equation relating the height of a spin echo to the diffusion coefficient:

$$A(t) = \exp(-\frac{1}{12} D\gamma^2 G^2 t_0^3) \tag{2.11}$$

where A is the echo amplitude, G the applied field gradient and t_0 the delay between the initial pulse and the π-pulse. A series of spin-echo experiments

could therefore be carried out in order to ascertain the diffusion coefficient of a given degenerate Fermi liquid. After including the self-diffusion of ^{3}He [37], the agreement of experimental results [45] with the Landau Fermi liquid theory, produced the belief that eq. 2.10 could describe accurately the diffusion in such systems. Thus it was thought that the diffusion of ^{3}He increased without limit as $T \rightarrow 0$, and that the echo attenuation would likewise increase as the temperature decreased.

This view was challenged by Leggett and Rice [7],[8]. Their core argument was that a strongly interacting Fermi liquid could not obey equation 2.10, and that the resulting expression relating echo amplitude to the diffusion coefficient (eq. 2.11) was invalid. Using the kinetic equation for the quasiparticle distribution, an equation describing the spin current, which included the effect of the molecular field, was derived. The starting point of the derivation is the continuity equation

$$\frac{\partial M}{\partial t} + \nabla \cdot \mathbf{J} = 0$$

which needs to be modified, to account for the coupling between $\mathbf{M}$ and $\mathbf{J}$ in the external field $\mathbf{B}$:

$$\frac{\partial M}{\partial t} + \nabla \cdot \mathbf{J} - \gamma \times \mathbf{B} = 0 \tag{2.12}$$

The spin current $\mathbf{J} = D\nabla M$ is modified to include the molecular field, giving

$$\mathbf{J}_i = -\frac{D_\perp}{1 + (\mu M_0)^2} \left\{ \nabla^2 M + \mu \left(\mathbf{M} \times \nabla M \right) \right\} \tag{2.13}$$

Combining equations 2.12 and 2.13 gives an expression for the time evolution of the spin density $\mathbf{M(r,}t)$ to be produced.

$$\frac{\partial \mathbf{M}}{\partial t} = \gamma \mathbf{M} \times \mathbf{B}_0 + \frac{D_\perp}{1 + (\mu M_0)^2} \left[\nabla^2 \mathbf{M} + \mu \left(\mathbf{M} \times \nabla^2 \mathbf{M} \right) \right]$$

For conditions where the longitudinal gradients can be neglected, this reduces

[4] to

$$\frac{\partial m_-}{\partial t} = i\gamma B(\mathbf{r})m_- + \frac{D_\perp}{(1+i\mu M_0)}\nabla^2 m_- \tag{2.14}$$

where $m_- = m_x - im_y$ is a single complex number grouping together the components of the transverse magnetisation and $B(\mathbf{r})$ is the $z-$component of the applied magnetic field (Note that the assumption of a small tipping angle is implicit in the above equations where $cos\theta$ is assumed to be very close to unity). This equation is analogous to the Schrödinger wave equation, whereby it describes the motion of a particle with mass $(i-\mu M_0)/D_\perp$ in a potential $-\gamma B(\mathbf{r})$. Under conditions of high μM_0 (extreme collisionless regime) the 'mass' tends to become purely real, and the spin-waves are undamped. This corresponds to the case of the Schrödinger equation for a particle in a box, where there is no energy loss as the particle oscillates. Conversely, for zero μM_0 the mass becomes purely imaginary, the equation reverts to its classical equivalent, and the diffusion of the spin waves is damped as normal. If the equation is solved for the boundary conditions appropriate for the experimental cell, the eigenvalues which correspond to the spin-wave mode frequencies are obtained. The sign of the spin-rotation parameter determines whether the modes seek a field maximum ($\Omega_{int}\tau_\perp < 0$) or field minimum ($\Omega_{int}\tau_\perp > 0$). In pure ^{3}He, μM_0 is negative, thus the standing spin-wave modes correspond to bound states at a maximum in the static field. A field maximum is impossible, so the edges of the experimental cell must be used to confine the spin-waves in directions along which the potential energy decreases.

2.5 Spin Waves

To solve equation 2.14 a solution of the form $m_-(\mathbf{r}) = \Phi(\mathbf{r})e^{\Omega t}$ is assumed. This produces the eigenvalues Ω and the eigenfunctions $\Phi(\mathbf{r})$. Under appli-

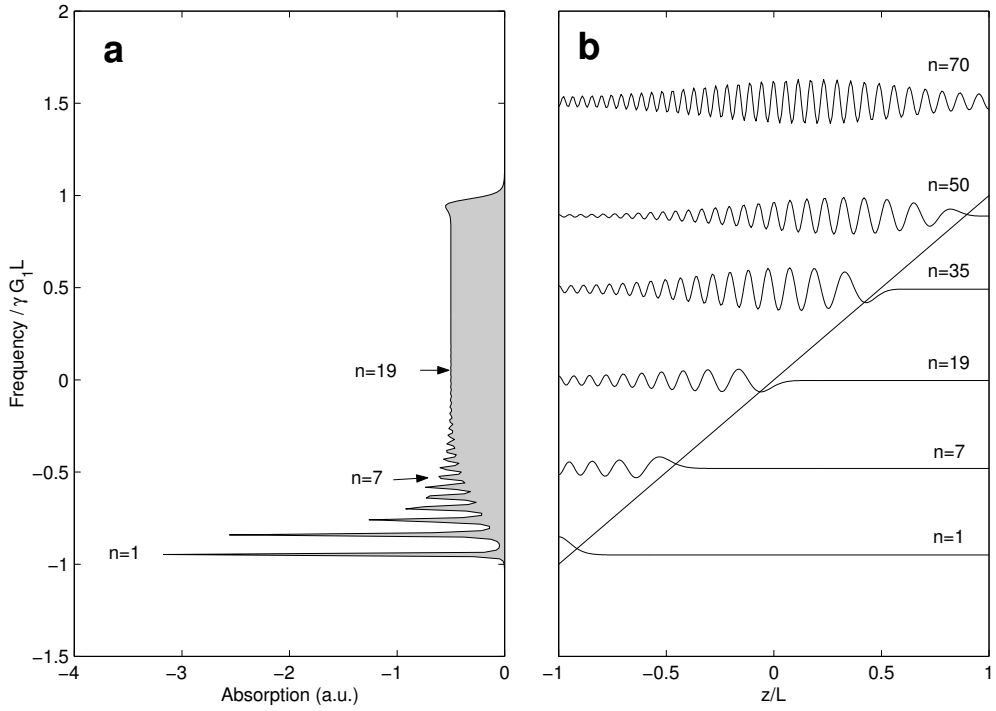

Figure 2.4: Numerical calculations of spin-wave modes calculated for $D_\perp = 0.375\text{cm}^2/\text{s}$, $\mu M_0 = 10$, $G_1 = 10$ G/cm and $2L$ =0.23cm. (**a**) NMR absorption spectrum. Frequencies are normalised by $\gamma G_1 L$. The spectrum extends from -$\gamma G_1 L$ to +$\gamma G_1 L$. The peaks represent weakly-damped spin-wave modes. (**b**) Real part of the wavefunctions, for the modes with $n = 1, 7, 19, 35, 50$ and 70. Wavefunctions are offset vertically by their respective normalised eigenfrequencies to render the comparison with quantum mechanical eigenstates. The straight line represents the confining potential of the linear field gradient.

cation of a linear field gradient the problem becomes one-dimensional:

$$\left\{ \frac{D_\perp}{(1 + i\mu M_0)} \frac{d^2}{dz^2} + i\gamma G_1 z \right\} \Phi_n = \Omega_n \Phi_n \tag{2.15}$$

with boundary conditions $d\Phi/dz = 0$ at $z = \pm L$. Examples of eigenmodes can be seen in figure 2.4. The numerical methods used to calculate the eigenmodes are described by Buu *et al.* [39]. The diagram shows the direct correlation between the spin-wave modes and the NMR lineshape produced. For a small linear gradient, fewer modes are trapped, giving a narrower lineshape. A very strong linear gradient will trap many modes, but compromises the quality of the NMR signal obtained, due to rapid dephasing of the spins. Exciting the spins with a single NMR pulse provides an FID, which renders the spin-wave modes after Fourier transform. The relationship between the

frequency and time domains is given by

$$F(\nu) = \int_{-\infty}^{\infty} f(t) \exp(-i2\pi\nu t) dt \qquad f(t) = \int_{-\infty}^{\infty} F(\nu) \exp(+i2\pi\nu t) d\nu$$

The magnetisation in the cell during an FID can be written

$$m_-(z,t) = \sum_n c_n \Phi_n(z) e^{\Omega_n t} \tag{2.16}$$

where Φ_n is the nth eigenmode with complex eigenfrequency Ω_n, the imaginary part of which produces the spin wave oscillations and the real part of which produces the damping. The mode amplitude is determined by the initial condition

$$c_n = \int_{-L}^{+L} m_-(z, t=0) \Phi_n(z)\, dz \tag{2.17}$$

For a uniform r.f. excitation field, the NMR signal $S(t)$ is the average of the magnetisation $m_-(z,t)$ over the sample, and the Fourier transform of $S(t)$ provides the NMR spectrum $S(\omega)$:

$$S(t) = \sum_n c_n d_n e^{\Omega_n t} \tag{2.18}$$

$$S(\omega) = \sum \frac{c_n d_n}{\Omega_n + i\omega} \tag{2.19}$$

where the weights of the modes are represented by

$$d_n = \int_{-L}^{+L} \Phi_n(z)\, dz \tag{2.20}$$

There are an infinite number of discrete spin-wave modes, but only those confined by the field gradient against the cell walls contribute significantly to the NMR spectrum. Those modes which have an exponentially decaying wave function contribute the greatest to the weight d_n: the "free states" have no turning point and, hence, an insignificant contribution to the spectrum. Thus there is a non-zero spectrum only for those frequencies in the bandwidth $\pm\gamma G_1 L$, as is the case for the high-temperature spectrum. There are poles at the eigenfrequencies $i\Omega_n$, thus allowing the spin-wave modes to be observed as peaks in the NMR spectrum. Numerical solution of the equation

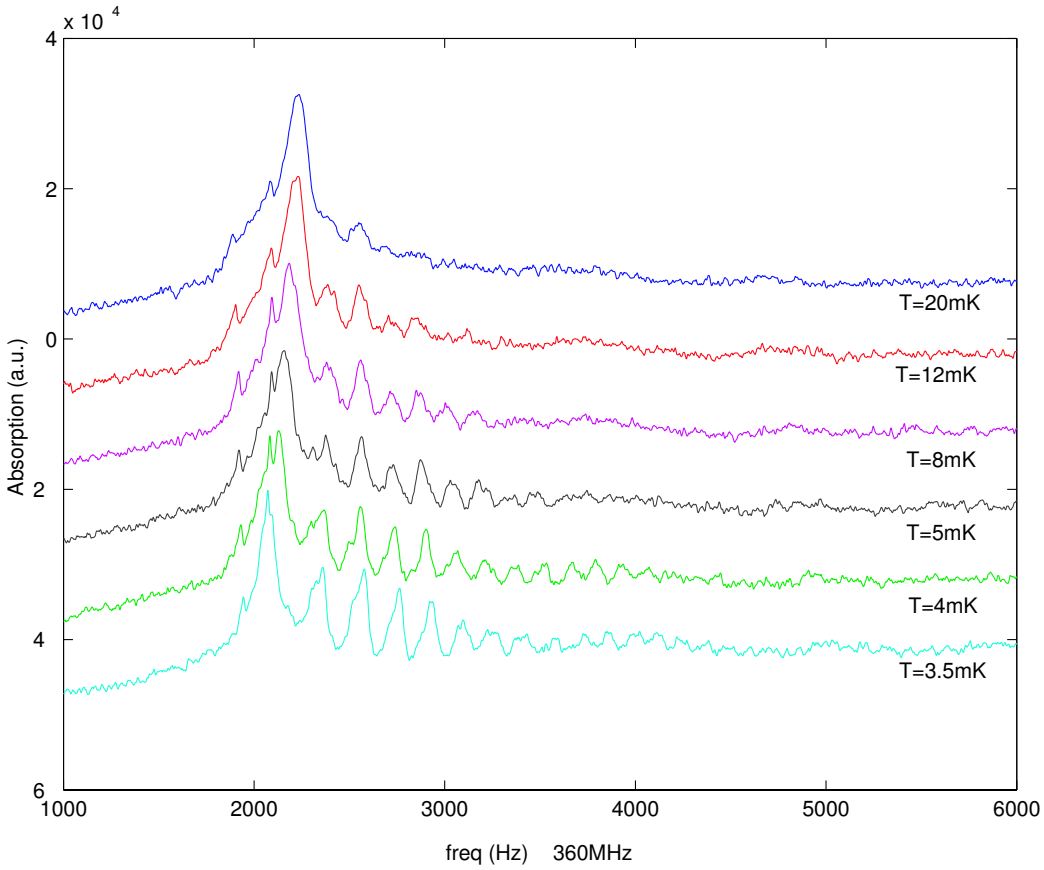

Figure 2.5: Mode spectra at different temperatures

of motion allows computation of the frequencies and widths expected for the spin wave modes. The position of the peaks, and hence their frequency, is given by the imaginary part of Ω_n and depends only on the real part of the 'mass' which is proportional to $\mu M_0/D_\perp$. The width of the peaks depends on the imaginary part of the mass and is proportional to $1/D_\perp$. In an experiment, the spin-wave mode peaks will become narrower as diffusion decreases, corresponding to a lack of damping. By comparing the simulation with experiment, it is theoretically possible to determine the diffusion coefficient. This is only possible qualitatively for our experiment, due to the presence of a stray quadratic field gradient across the experimental cell.

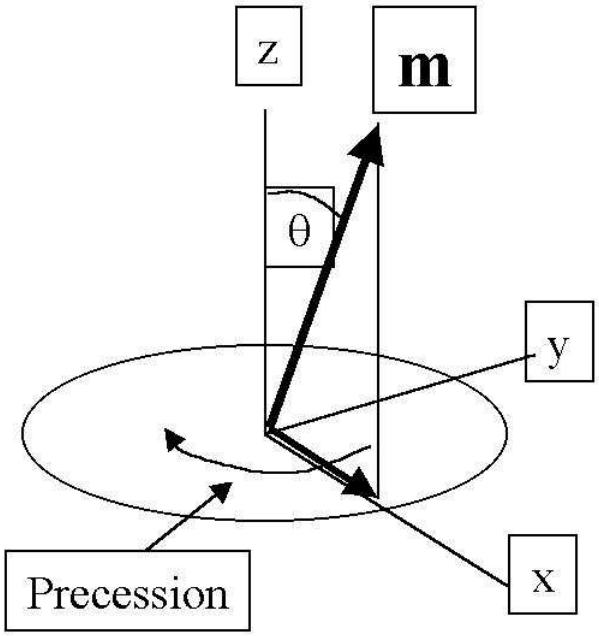

Figure 2.6: Schematic representation of spin precession

2.6 Spin Echoes

The pioneer of the spin echo technique was Hahn [46] who demonstrated experimentally the recovery of an echo signal in glycerine and water. A vast number of uses has followed from this initial experiment, and an outline of the theory behind the technique follows.

If an r.f. pulse is applied to the transverse $(x - y)$ plane at the Larmor frequency it will cause the magnetisation to be displaced an angle θ from equilibrium. The angle of displacement is dependent upon the duration of the applied r.f. pulse. On removal of the pulse, the tipped magnetisation vectors precess in the $x-y$ plane at the Larmor frequency, generating a signal in the receiver coil (fig.2.6). This signal is called a free induction decay (FID), and is used to excite spin-wave modes.

As thermal equilibrium is re-established the magnetisation will regrow along the $z-$ axis. This time is called the spin-lattice (longitudinal) relaxation time, or T_1. The equivalent equilibrium time in the $x - y$ plane is called the spin-spin (transverse) relaxation time, or T_2. This relaxation is due to

fundamental molecular processes, e.g. diffusion. In order to create a spin echo, a linear field gradient needs to be applied in the z- direction. The spins in the cell will now precess at different rates depending upon their displacement from the field centre. This causes different regions of spins (known as 'isochromats') to dephase from each other. If a π- pulse is applied at a time τ, the spins will be flipped through 180^0. They will then begin to precess in such a way that those spins which had previously experienced the highest net field, and hence frequency, now experience the opposite. The "slow" spins likewise change to a fast-frequency state. The spin system refocuses at $\sim 2\tau$ to produce an 'echo'. For ideal (uniform) tipping pulses carried out instantaneously, the result will be the equivalent of back-to-back FIDs (assuming no loss of signal between pulses). Any decrease in the echo amplitude with respect to the magnitude of the initial pulse will give a measure of the magnitude of diffusion in the experimental cell. In any experimental apparatus there will be a 'dead time' associated with the receiver, so the first portion of any FID will be lost from the data acquisition. A spin-echo eliminates this source of loss. An example of a typical spin-echo sequence obtained during the experiment is given in fig. 2.7. Spin echo signals have typically been analysed using Leggett's equations (eq.4.3), which allow one to calculate the diffusion coefficient and spin-rotation parameter from the phase shift and attenuation of a spin echo (see section 4.1). Leggett assumed a weakly spin-polarised system, and his equations are not valid for strongly polarised systems. Another difference between Leggett's model and experiment is his assumption of unbounded diffusion, and the inhomogeneity of the applied field gradient for these experiments. It will be shown that Leggett's assumptions are not completely valid for the experiments reported herein.

The starting point is the equation of spin motion, eq. 2.14, as written above. For the equation to be valid the following conditions apply: the sample size and the characteristic length scale of the magnetic field inhomogeneity must

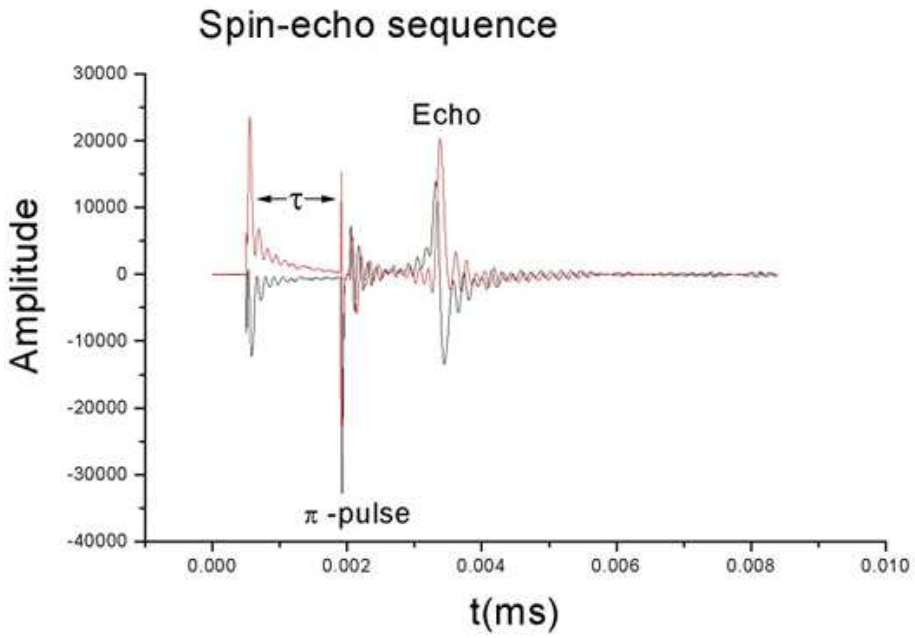

Figure 2.7: Typical spin-echo observed during experiment

be larger than the quasiparticle mean free path; a small tipping angle must be used for $|M_0|$ to be uniform throughout the sample and constant in time; the applied magnetic field must be very large compared with the local field variations. The exact analysis was performed by Buu *et al.* specifically for the experiments carried out in 6.2% mixture over the course of this work. The details can be found in reference [39]. The points relevant to the data analysis are given in section 4.2.2

The approximation of the cell is a one-dimensional slice, and solving equation 2.14 provides the linear combination of eigenmodes described in equation 2.16. Once the eigenmodes and eigenfrequencies are obtained, it is possible, providing the relevant initial conditions are followed, to simulate any behaviour of the spin evolution, including the spin waves from an FID (as described in the previous section). A spin echo is, in principle, nothing more than two FIDs back-to-back, and can also be simulated numerically. The incorrect use of an equation for analysis of spin-echo data can produce very disparate results. The analysis of data, both for this group, and a review of

the conditions for those of other groups, follows in section 4.2.2

2.6.1 Multiple Spin Echoes

The formation of multiple spin echoes has been an acknowledged consequence of the non-linearities of the equation of spin-motion governing the mechanics of spin evolution in the system. Although it has not been a major part of the experiment, MSE's were observed, in both pure ^{3}He and ^{3}He-^{4}He mixtures, and a brief comment is pertinent.

The nonlinearities lead to harmonics in the equation of motion. In a spin echo experiment, the first pulse causes a helical winding of the transverse magnetisation. After the second pulse at time τ, the helix unwinds, producing the first spin echo. The subsequent echoes are formed because the higher harmonics have their phase shifts exactly compensated for by the Larmor precession, leading to in-phase spins at times $n\tau$. In general, the pulses used will be large-angle, typically 90^0 for the initial and second pulses. This is because, for 90^0 initial pulses the molecular field is rotated perpendicular to the external field. This provides for the 'tightest' helix, which causes the maximum number of echoes. An example of a MSE produced during the experiment is shown in fig. 2.8.

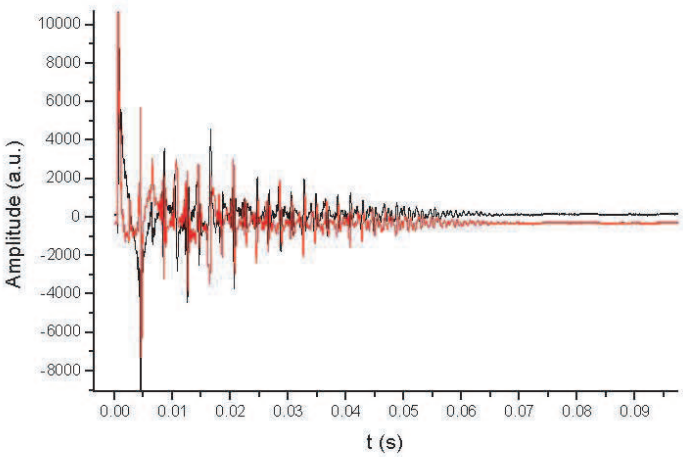

Figure 2.8: Sample MSE obtained during experiments

Chapter 3

Experimental Details

3.1 General Features of the Experiment

The experiment used three different Fermi liquids, pure ^{3}He (very strong quasiparticle interactions), a 6.2% ^{3}He-^{4}He mixture (milder interaction effects), and a 0.7% mixture (very weak interactions). For each case the basic setup was identical. The dimensions of the experimental cell plus heat exchanger are given in figure 3.1. The experimental cell itself was a 2.3 mm right cylinder constructed of Stycast 1266.

It was connected to the Helium reservoir by a Stycast 1266 channel with a diameter of 0.5 mm and a length of 10 mm. The Helium reservoir was filled through a 0.5 mm CuNi capillary, and parts of this capillary were quite close to the NMR region. It is not possible to rule out the fact that some of the experimental artifacts, e.g. the unusual asymmetric background lineshape of the NMR spectrum (sect. 4.2.2), are due to the relative proximity of this filling line to the NMR cell. Simple order-of-magnitude calculations [14] indicate that the field of $\sim$0.3 G produced by the filling line is a contender for the non-linear field gradient; a more realistic model is, however, beyond the scope of this thesis.

The NMR circuit was a saddle coil made of 600 μm diameter silver wire and tuned to 367 MHz. This formed a cylindrical 'cavity', 12 mm in length and

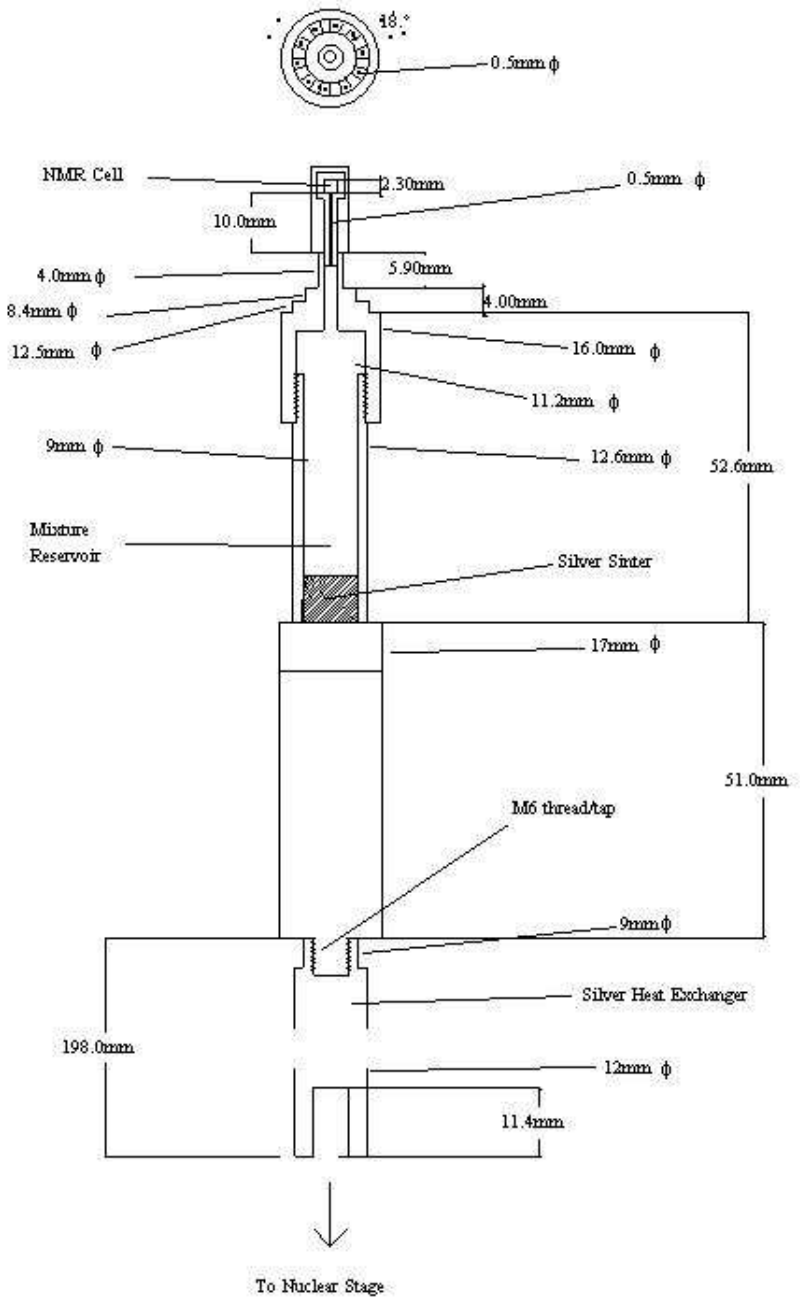

Figure 3.1: Dimensions of the experimental cell and heat exchanger

6 mm diameter within which the NMR cell was situated. Both the main polarising field and the linear field gradient were directed along the cell axis. The cell and channel were supported in an epoxy resin casing. The volume of the cell plus channel was 7.25 mm^3 and the volume of the reservoir was 1193.5 mm^3. The bottom part of the reservoir was a 212.1 mm^3 cylinder of silver sinter, of $\sim 40\%$ silver by volume. Also contained within the reservoir was a vibrating wire viscometer, a mylar capacitance thermometer and a CMN resistive thermometer. The silver sinters of the mixture cell and the heat exchanger were connected by a capillary. A simplified version of the experimental setup appears in figure 3.2.

The heat exchanger was screwed tightly to a copper demagnetisation stage, which was itself mounted onto a dilution refrigerator. The thermal contact provided by this attachment mechanism was tested indirectly by measuring the electrical conductivity between the copper stage and the silver heat exchanger. A 5 A current was applied between the top of the reservoir and the stage, allowing the voltages to be read across various points of the cell and heat-exchanger. A good benchmark for a tight thermal contact was a voltage of ~ 240 nV from the top of the reservoir to the copper stage, giving an electrical resistance of ~ 50 nΩ through three screw-joints.

The leads connecting the vibrating wires to the coaxial connecting cables were Niomax twisted pairs, and the capacitance and CMN thermometers used cupronickel twisted pairs. The coaxial cables were heatsunk by removing the plastic coating and using GE varnish to affix the outer to the stage. The twisted pairs were varnished to the stage and this was adjudged to provide sufficient heatsinking. All connections to the cell were also heatsunk at the 1 K pot.

The sample is cooled to ~ 15 mK at maximum field by the dilution refrigerator, before the superconducting heat switch is 'opened'. The heat switch is

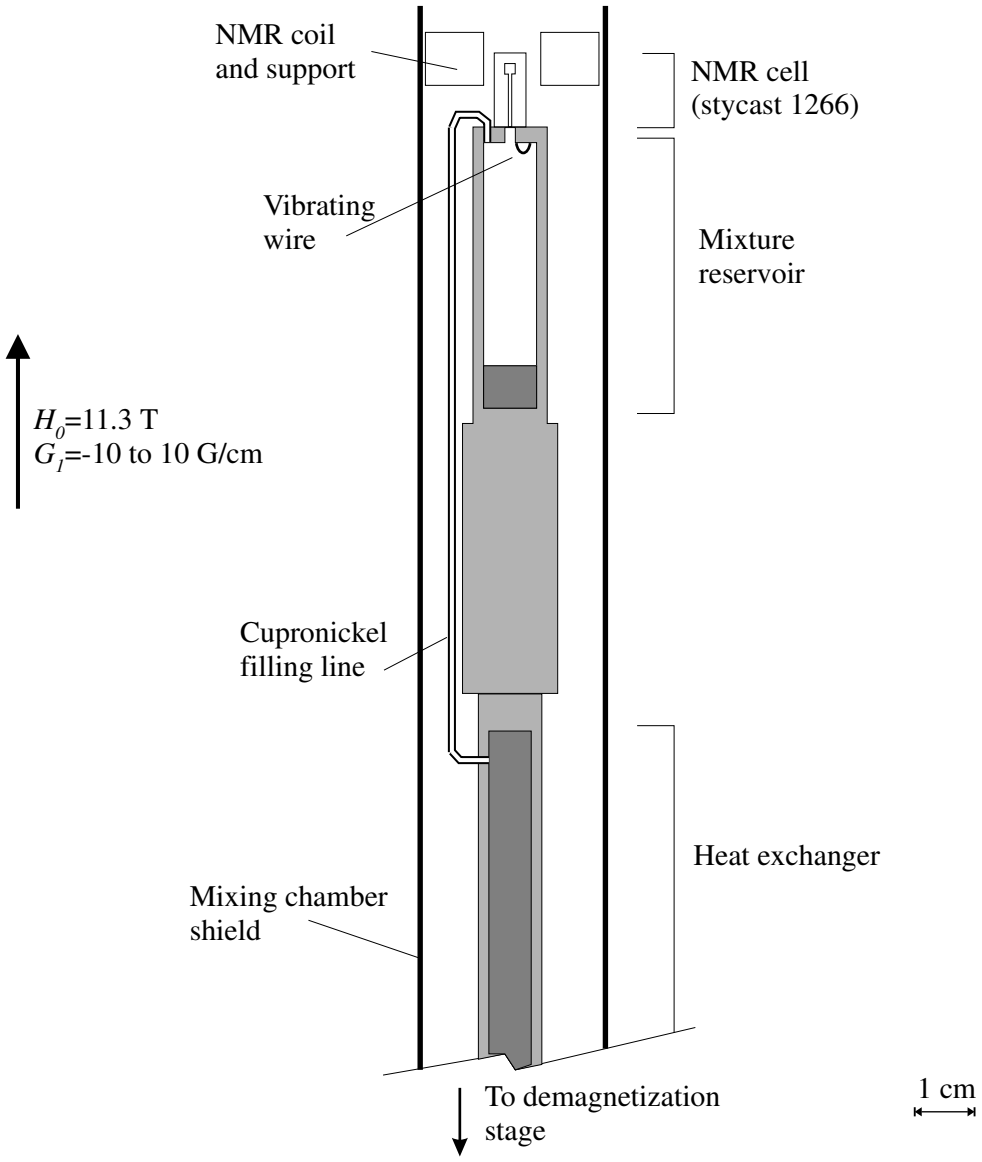

Figure 3.2: General overview of the cell, reservoir and heat exchanger

made of Aluminium, an element which has an intrinsically low thermal conductivity at low temperatures, and which conducts virtually no heat when in its superconducting state. From this point the only cooling available is from the adiabatic demagnetisation of the copper stage. There are 24 mol of copper in the demagnetisation region; the other significant source of heat capacity is provided by the 2.83 mol of silver which make up the cell and the heat exchanger (the 0.152 mol ^{3}He and 0.203 mol ^{4}He for a 6.2% mixture have an insignificant contribution to the total heat capacity). The electronic heat capacity of the copper is also insignificant. Despite the electronic heat capacity of the silver being more significant, the thermal resistance is sufficiently high to eliminate this as a major source of heat load. The copper stage is cut along most of its length to reduce eddy current heating during demagnetisation. The pattern of slits was chosen to provide the minimum area of bulk sections to minimise eddy current effects, whilst allowing a large total cross-sectional area to allow the maximum volume of copper.

After resetting the shim currents to obtain the narrowest NMR line, a set of FIDs were taken for each temperature, with sufficient time allowed between FIDs to allow full recovery of magnetisation. Finally, a set of spin-echoes was taken, with a time-delay τ_e between the tipping pulse and $\pi-$ pulse which varied from a fraction of a micro-second, up to the point where an echo was no longer discernible. This varied according to the sample. At the lowest temperatures, the cell was left for up to 12 hours to attain thermal equilibrium after a demagnetisation step. The $\pi-$ pulses caused significant heating at the lowest temperatures; the system was left for up to two hours to regain its equilibrium temperature before taking another measurement in these cases. The effect of heating from NMR pulses and any heat leaks has been discussed in some depth elsewhere [14], but a summary of the conclusions is pertinent.

There are thought to be four significant heating effects in the cell. These are

static temperature gradients, heating due to r.f. pulses, slow temperature drift and thermally-induced concentration gradients. The static temperature gradients caused by, for example, thermal relaxation of the stycast cell, are estimated to cause no more than a 2 μK temperature difference for the experiment. The thermal equilibrium time constant between the cell and the reservoir is calculated to be significantly lower than the time waited between each spin-echo measurement. The heating caused by r.f. pulses is a more complicated situation. This heat energy is dispersed via three different mechanisms. These are the heating of the sample due to transverse diffusion processes, the equivalent longitudinal processes, and joule heating of the silver walls of the reservoir. Calculations show that the last two mechanisms do not impinge on the temperature of the sample during the course of the NMR experiment. The effect of the first mechanism is presented in figure 3.3. A final thermal effect is that of heating causing a concentration gradient. This is not a problem for the ^{3}He and the 6.2% mixture. The 0.7% mixture should be more susceptible to this kind of effect, but no discontinuities in the value of the magnetisation were recorded, indicating no significant concentration gradients. This was not the case for a more dilute mixture examined during thermometric experiments (see section 5.3.3).

3.1.1 NMR Techniques

A superconducting magnet provided the main 11.3 T field for the experiment, with quadratic shim coils used to ensure a high degree of field homogeneity. Linear shim coils provided the linear field gradient, with values of -8.6 Gauss/cm producing the most consistent spin-echo data. This compromise minimised the effects of any stray gradient fields, whilst allowing for a uniform tipping angle. The π - pulses and 'tipping' pulses for the three different concentrations under observation varied slightly. The changing value of the $\pi-$ pulse is due to slightly different settings for the attenuation or

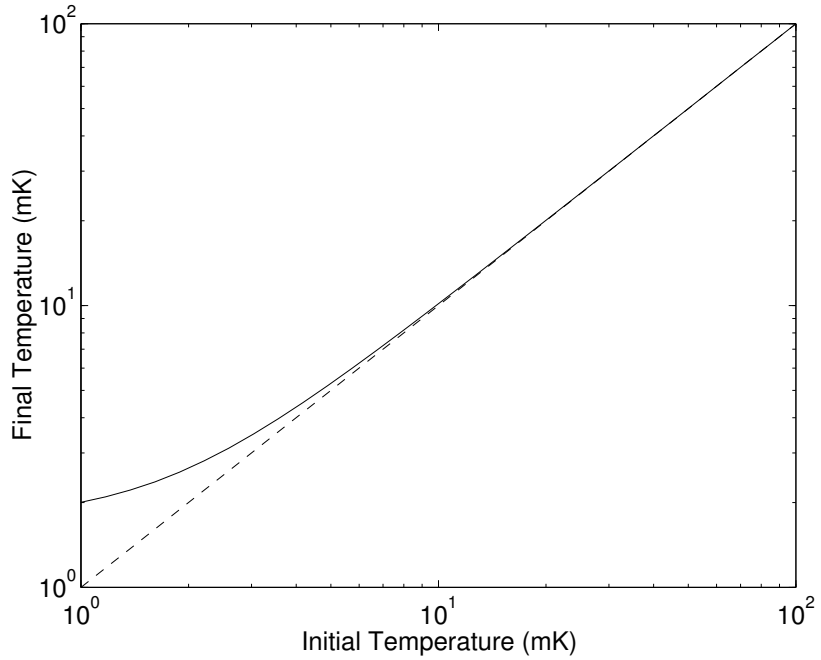

Figure 3.3: Temperature increase from transverse diffusion processes, calculated for T_F =407 mK and 11.3 T applied field

amplifiers between experimental runs. The tipping pulse lengths were chosen so as to maximise the signal-to-noise ratio, whilst maintaining linearity of the spin-motion equations. The spin echo signals were obtained by using a computer-controlled set of pulses, which sent the correct pulse sequence after allowing sufficient time to elapse between echoes. The delay time was automatically increased by increments, until there was no discernible echo. For pure ^{3}He this occurred at 20 ms, for the 6.2% mixture at 3 ms, and at 7 ms for the 0.7% mixture.

Sample	π - pulse	Tipping Pulse (FID)	Tipping Pulse (Echo Sequence)	τ_e
Pure ^{3}He	21 μs	1 μs	1 μs	2-20 ms
6.2% Mixture	26 μs	1 μs	3 μs	1-3 ms
0.7% Mixture	26 μs	2 μs	3 μs	2-7 ms

Free Induction Decay

The Free Induction Decay (FID) is the simplest method available to investigate the properties of a system using NMR. It involves applying a small

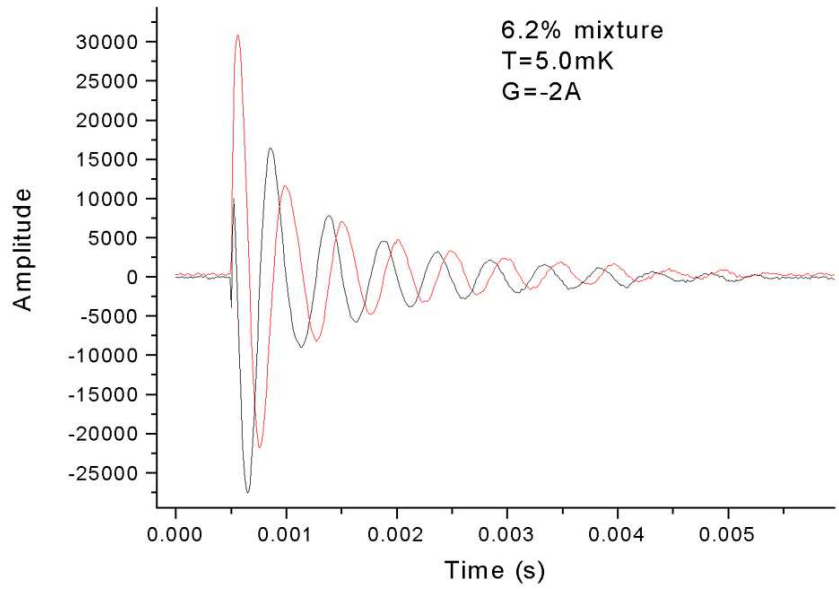

Figure 3.4: Typical FID obtained during experiment

'tipping' pulse in the $x-y$ axis, typically up to 10^0 in the presence of a linear field gradient. Small tipping pulses are used to maintain linearity conditions in the equations of motion. Standard practice was to detune the NMR frequency by 2 kHz to avoid 50 Hz noise and DC offsets. The FID can provide information about the NMR frequency spectrum, because the two are linked by Fourier transformation. Convention dictates naming the imaginary part of the spectrum as absorption, the real part as dispersion. The FID is of particular interest for the creation and analysis of spin waves. A single pulsed FID excites all the frequencies across the cell. The excitations show up as peaks in frequency on a Fourier transform (FT) of the signal. A typical FID signal can be seen in figure 3.4 , and an FT showing the frequency spectrum in figure 3.5

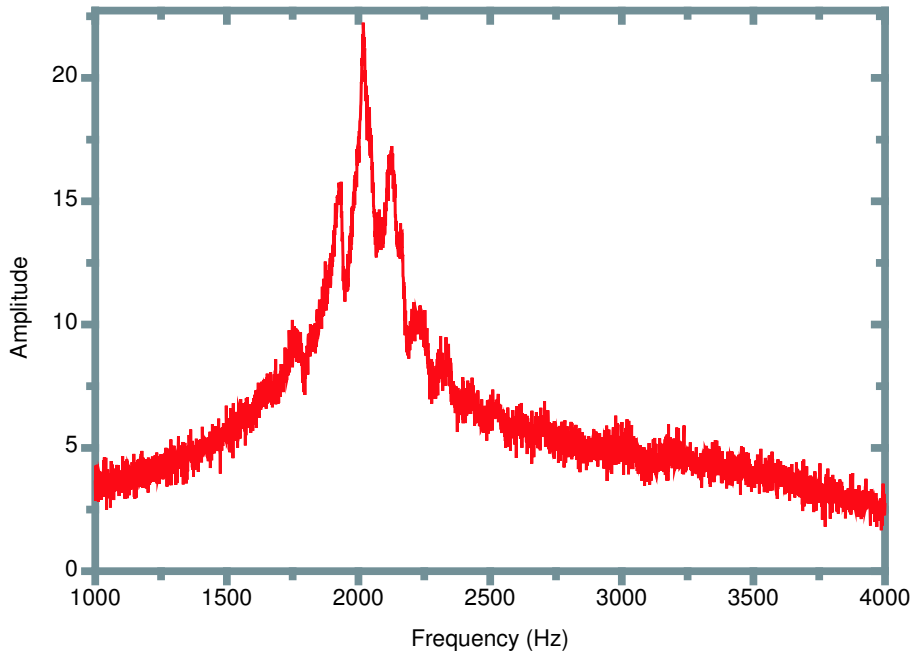

Figure 3.5: Fourier transform of an FID

3.1.2 Thermometry

Dilution Refrigerator and Stage

Ruthenium oxide thermometers are inexpensive and accurate. They are small and have high reproducibility on thermal cycling. They are commercially made thick-film resistors which are a mixture of metal and ceramic. The resistance curves have been fitted to the expression

$$R(T) = R_0 \exp\left[\left(\frac{T_0}{T}\right)^{0.345}\right]$$

to within 0.5% between 25 and 800 mK [52]. The RuO_2 thermometer on the stage is useful down to $\sim$ 20 mK, whereupon it begins to saturate, and other thermometric techniques are required.

Magnetic Thermometers

PdFe The PdFe thermometer is a widely used and well known low-temperature thermometer. The physical basis for its use is the fact that the nuclear magnetic susceptibility χ varies with temperature thus:

$$\chi = \frac{\lambda}{T}$$

where the Curie constant

$$\lambda = \frac{N_0 I(I+1)\mu_0 \mu^2 g^2}{3k_B} \tag{3.1}$$

with N_0 the Avogadro number and g the Landé splitting factor. For the Curie law to be valid there needs to be no changing internal fields due to the nuclear or electronic magnetic ordering in the relevant temperature range, and an absence of nuclear electric quadrupole interactions (which is a geometric factor which can be avoided by choice of a suitable material).

The sample used is a rod, 5 mm in diameter, with an iron content of 25 ppm. Slits are cut into the rod to reduce eddy current heating. The primary coil is made of 320 turns of 125 μm diameter NbTi in CuNi matrix wire, the secondary is 7270 turns of high purity 25 μm diameter silver. The sample is magnetically shielded from stray fields by a superconducting niobium cylinder. The excitation current used is 100 μA at 40 Hz. The changing flux of the excitation current induces a voltage in the secondary which is proportional to the susceptibility of the iron in the sample:

$$U_{ind} = A + B\chi$$

The PdFe is calibrated using the NBS (National Bureau of Standards, U.S.A) superconducting fixed-point device. The five superconducting samples in the device have known transition temperatures. These transitions are detected from the expellation of flux from the samples by the coils surrounding them.

Once the calibration is complete, the PdFe can be used over a wide range of temperature. Unfortunately, due to its sensitivity to magnetic fields it is inappropriate for use in our experimental cell, and is therefore confined to the 'continuous cooling' part of the fridge (i.e. the liquid-cooling part rather

than the magnetic-cooling part). It is also not useful below $\sim$ 15mK. This is due to the fact that, by this temperature, magnetic ordering is virtually complete, thus small changes in temperature no longer cause differences in the magnetisation.

The gold-erbium thermometer has been specifically designed to counter these difficulties at very low temperatures (< 10 mK). The method of measurement is identical to that of the PdFe. The Gold forms the magnetically inert matrix into which the Erbium atoms are scattered. Erbium is present in the ratio 20 ppm. Because of these low proportions, there should be no saturation until sub-millikelvin temperatures are attained. A very sensitive secondary coil is required to pick up the signal, which is proportional to the number of magnetic atoms present in the sample (equation 3.1). The secondary coil used was 10000 turns of ϕ25 μm copper wire, with a primary of 434 turns of ϕ60 μm wire NbTi in a copper matrix. Despite the positive results from other groups at low temperatures, this thermometer did not prove satisfactory, as it saturated at temperatures far above those required.

The thermometry readings for the experiment below $\sim$ 15 mK were based on a tantalum vibrating wire viscometer (vwr). The use of vwr's in low temperature work is widespread, and makes use of the fact that the viscosity of ^{3}He and its mixtures is well known ($\propto T^{-2}$) at low millikelvin temperatures. The physical premise behind its use is straightforward. Any wire which carries an alternating current in a magnetic field (B) experiences the Lorentz driving force. Thus, for an alternating current $I = I_0 e^{i\omega t}$ through a semicircular loop, the force produced is $F_D = BI_0 e^{i\omega t}$. For a wire which vibrates at its resonant frequency ω_{res}, the displacement from equilibrium can be written $y = y_0 e^{i\omega t}$, with y_0 the maximum displacement. As the wire vibrates, it cuts through lines of magnetic flux. This induces a voltage $V = V_0 e^{i\omega t}$. For a frequency sweep, the drive is a constant and the frequency varied by increment across

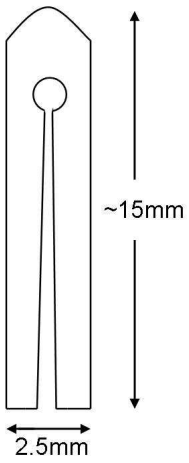

Figure 3.6: Schematic of the quartz spherical NMR cell

a given frequency range (standard practice for experiment was a factor 10 greater than the half-width). This produces a Lorentzian curve, from which the quality factor, and frequency shift from vacuum, can be extracted. These quantities can be used to determine the viscosity, and hence temperature, of liquid ^{3}He-based systems over the regime of interest (see sections 5.1.6 and 5.3.4 for details of analysis).

3.1.3 Spherical Cell

Although the original cell provided much useful data, the analysis proved to be complicated by the cylindrical geometry. Using samples sent by Don Candela, a new experiment using a spherical symmetry was constructed (fig. 3.6). The dimensions of the cells were difficult to measure accurately. To match the refractive index of the glass it was necessary to conduct the measurements whilst the cells were submerged in a bath of 2-Fluorotoluene at a temperature of 45^0C. The silver cap of the reservoir was redrilled to allow entry of the new cell. The length of the cell is approximate, as the length diminished each time the base of the cell was snapped off during a failed assembly of the experiment. After several breakages the design of the NMR resonator was altered, and a shield was used to attempt to protect the cell

during the delicate insertion process. Initially a shield of plastic was considered. As the design of the resonator changed, however, it was decided to use the shield to support the resonator and to ensure the cell would be placed in the centre of the resonator. The quartz cell needed to be thermally isolated from the rest of the cryostat, as the parts of the apparatus surrounding the cell are maintained at the base temperature of the dilution refrigerator ($\sim$ 10 mK), which can be significantly greater than that of the NMR cell. Once the heat switch between the dilution stage and the demagnetisation stage has been opened, heat transfer must be minimised, thus the material with the lowest thermal conductivity which can be easily machined should be used. Various materials were considered, but after some investigation it appeared that wood was the best option [53], the best choice being oak. A graph showing the relative thermal conductivities of different options can be seen in figure 3.7.

Despite incorporating the wooden shield, the quartz cell continued to be damaged on insertion. A slight bend at one of the joints of the heat exchanger caused additional problems with the cell being shifted several millimetres from its central position. It was decided that there was a fundamental problem with the design of the cell, and attempts to perform experiments on the cylindrical cell were halted. Work turned to the investigation of the tuning fork and plastic capacitor, as described in chapter 5.

NMR Resonator

An improvement over the saddle-coil NMR resonator is the birdcage resonator, as described by Akimoto *et al.* [54]. This design produces a more homogeneous r.f. field than the saddle coil if the number of 'legs' is greater than 6. The birdcage resonator constructed was an 8-leg model. By varying the length of the legs it is possible to vary the resonant frequency of the circuit to match the frequency at which the measurements occur. Each leg

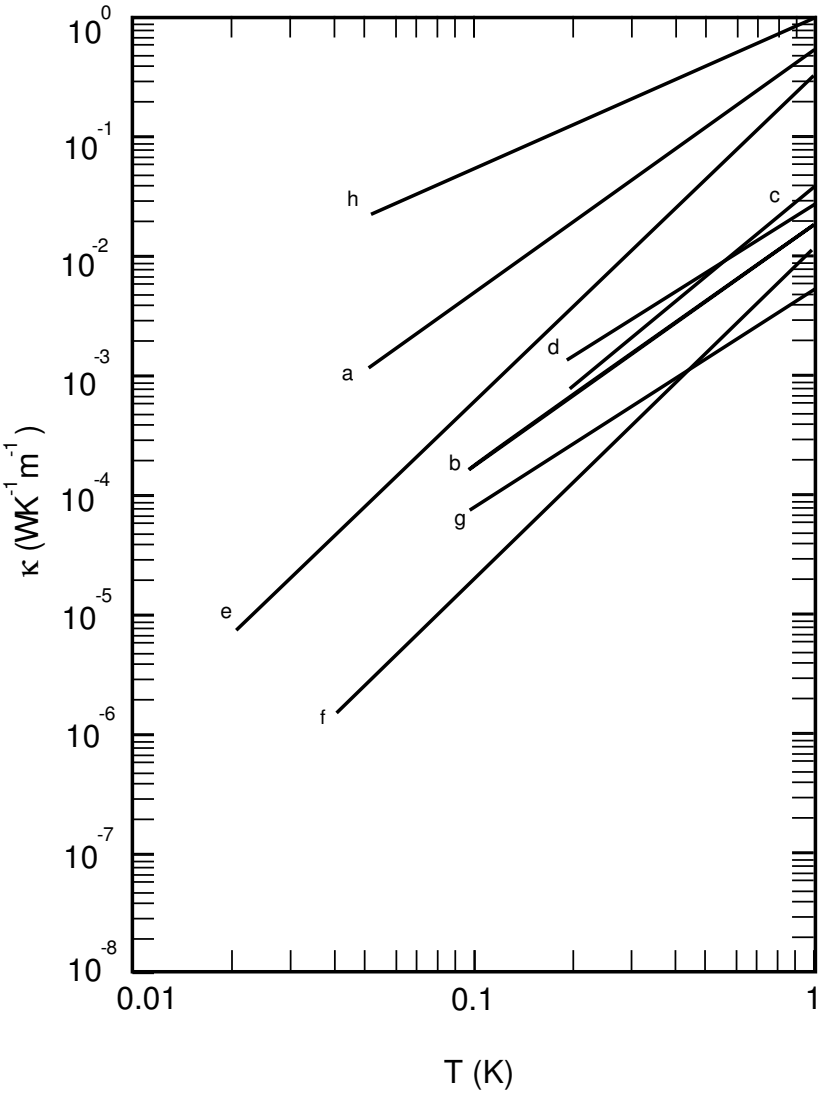

Figure 3.7: Thermal conductivities of different materials: a, Stycast 1266; b, Vespel SP22; c, Teflon; d, nylon; e, sintered Al_2O_3; f, wood (oak and maple); g, AGOT graphite; h, Cu-Ni alloy (after Wagner *et al.* [53])

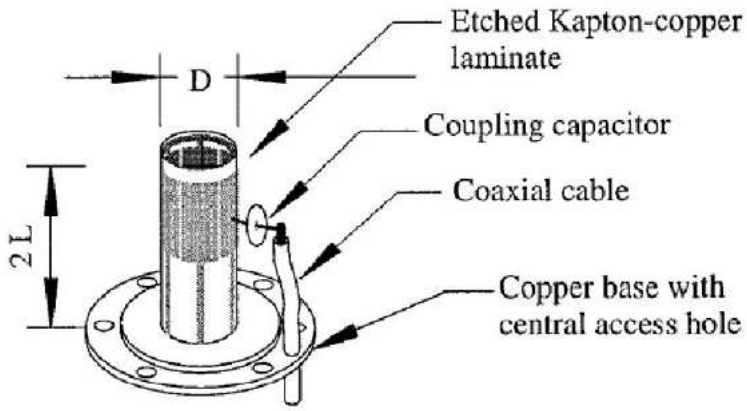

Figure 3.8: Diagram of a 6-legged birdcage NMR resonator (after Akimoto *et al.* [54])

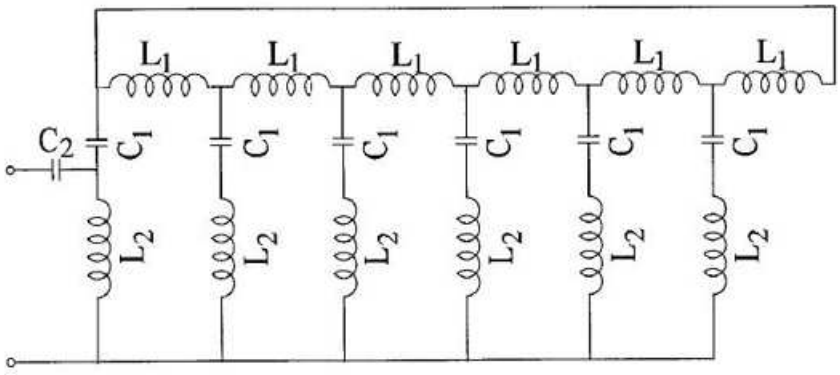

Figure 3.9: Equivalent circuit for the birdcage resonator (after Akimoto *et al.* [54])

of the resonator consists of a thin piece of copper, which forms the 'inductor', and a connecting thicker piece, which forms the 'capacitor'. All the legs are connected at the base (see fig. 3.8). Thus an equivalent L-C circuit is formed, as seen in figure 3.9. A second advantage of this design is the shielding of the resonators from stray r.f. due to the copper shield around the resonator. There is also no thermal link to the cell, thus the r.f. pulse energy is taken up by other, warmer, parts of the cryostat.

Chapter 4

NMR Results

4.1 Data Analysis

Longitudinal Diffusion $D_{||}$

Longitudinal diffusion occurs when the orientation of the magnetic moments remains unchanged but the magnitude is altered. The experimental cell is connected to a large ^{3}He (or mixture) reservoir by a capillary. In order to equalise the chemical potentials inside the reservoir and the NMR cell, a gradient of magnetisation is set up which drives diffusion. Knowing the dimensions of the cell and the linking capillary, the time constant of the re-magnetisation may be determined. If L and A are the length and area of the capillary, and V is the volume of the experimental cell, the time constant is given by $\tau_{||} = LV/AD_{||}$. The situation has the potential to be complicated by the effects of bulk (intrinsic) and surface relaxation, as discussed later. This provides an overall time constant of the form

$$\tau \sim \left[\left(\frac{LV}{AD_{||}} \right)^{-1} + \frac{1}{T_{Bulk}} + \frac{1}{T_S} \right]^{-1} \tag{4.1}$$

The bulk relaxation has a timescale of the order $\sim 10^4$ s, and may be neglected. The surface relaxation is likewise insignificant compared to the relaxation due to diffusion.

The technique used for measuring longitudinal diffusion is that most commonly used, that is, to invert the magnetisation of the spins in the experi-

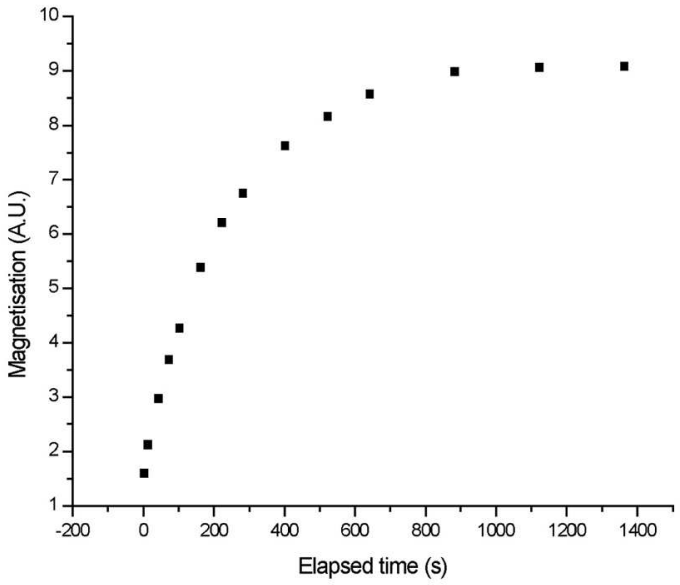

Figure 4.1: Typical recovery sequence for longitudinal magnetisation recovery

mental cell, and to sample the magnetisation at time intervals as it regrows along the $z-$axis. To invert the spins a 180^0 r.f. pulse is applied. The magnetisation then regrows along the axis of magnetisation exponentially, until the equilibrium value is restored, with a time constant T_1. To determine the value of the magnetisation, the spins need to be rotated away from the $z-$axis. Thus, small tipping pulses are applied at various times after the initial $\pi-$pulse. These give rise to FIDs, the signal of which is integrated to produce the value of magnetisation. An example of a magnetisation recovery curve can be seen in figure 4.1.

Imperfections in the 180^0 pulse ensure that a small component of transverse magnetisation is excited. This is a small effect, due to the precession frequencies varying across the field gradient, and relaxation time constants are of the order milliseconds, rather than the seconds over which the longitudinal magnetisation changes. Thus there is a negligible effect on the results of the experiment in determining the diffusion coefficient.

A problem which manifested itself at very low ($\leq$ 2 mK) temperatures was

the very rapid recovery of magnetisation. This had two effects. Firstly it made the determination of the magnetisation difficult, as fewer pulses could be used before recovery, causing greater uncertainty in the fitting algorithm. Secondly, there was a potential conflict with the transient state which exists immediately following an inversion pulse. This is the state which exists prior to the steady-state magnetisation gradient, and during which it is not possible to determine the time constant from equation 4.1. This enhances the problems of a very rapid recovery, as it limits the time at which tipping pulses may start to be applied. In general this has not caused problems, as the published data does not extend below 3 mK, where there are, additionally, problems with the thermometry.

The general idea of longitudinal diffusion has been outlined in section 2.3.1, but the experimental implementation is a little bit more sophisticated: after destruction (or inversion) of the magnetization in the cell by NMR, we measure how it recovers by diffusion through the channel from the Helium reservoir. There are several stages in the process. Initially, a quasi-stationary magnetisation profile is created in the filling channel. This process has a timescale of $t_{diff} = l^2/D_{||}$, approximately 0.16 s at 3.5 mK and 11.3 T [14]. Next, diffusion occurs from the reservoir to the NMR cell. As the magnetisation of the spins in the reservoir is still aligned along the $z-$axis, the chemical potential of the spins in the cell is different to that of those in the reservoir. To equalise the chemical potential, a gradient of magnetisation is formed. It is this gradient in magnetisation which drives the diffusion current. The final stage is the longitudinal relaxation in the reservoir, which takes place over roughly 10-100 s, a very large timescale compared with the first two processes.

Surface Relaxation When considering the relaxation of spins, it is important to realise that surface relaxation effects have the potential to complicate

the analysis of the spin-lattice relaxation time. This is because any observed relaxation time T_1 is a combination of the intrinsic relaxation, the time taken for spins to diffuse from the reservoir and the surface relaxation which occurs at the cell boundaries [47]. In the 'diffusion-limited' regime (where the interaction length of the quasiparticles is comparable to the cell length), for example, relaxation times are determined by the time taken for ^{3}He atoms to reach the walls. This time varies roughly as T^{-2} at low temperatures, giving a sizeable surface relaxation time T_s. Thus, whilst the diffusional relaxation time $T_{||}$ is predicted to vary as T^{-2} in the Fermi-liquid regime, in practice there is always a deviation due to the surface relaxation effects.

For pure ^{3}He, Hammel and Richardson [48] describe a model which accounts for the observed linear dependence for T_1 with magnetic field and temperature. Experiments have demonstrated [49], [50] that the first layer of the ^{3}He on a surface is immobile, acting as a solid layer with a density like that of solid ^{3}He at 100 bar. This solid-like layer is thought to facilitate the magnetic coupling to the bulk spins, enhancing the relaxation of magnetisation. The exact mechanism of this relaxation is not understood, but is believed to be an atomic exchange process occurring on a nanosecond timescale [51]. The proportionality of T_1 to temperature is due to the temperature-independent relaxation process to the surface layer. The efficiency of this process increases due to the equilibrium surface magnetisation becoming large, whilst the liquid polarisation remains constant.

This observed surface-dominated behaviour, which is contrary to that of bulk liquid, means that the experiments undertaken at low field and low temperature are those at greatest risk of suffering deviations due to surface relaxation. Thus in the pure ^{3}He data presented (fig. 4.2), the crossover to the T^{-2} regime, from the surface-dominated $D_{||} \propto T^{-1}$, occurs only at the lowest temperatures reached.

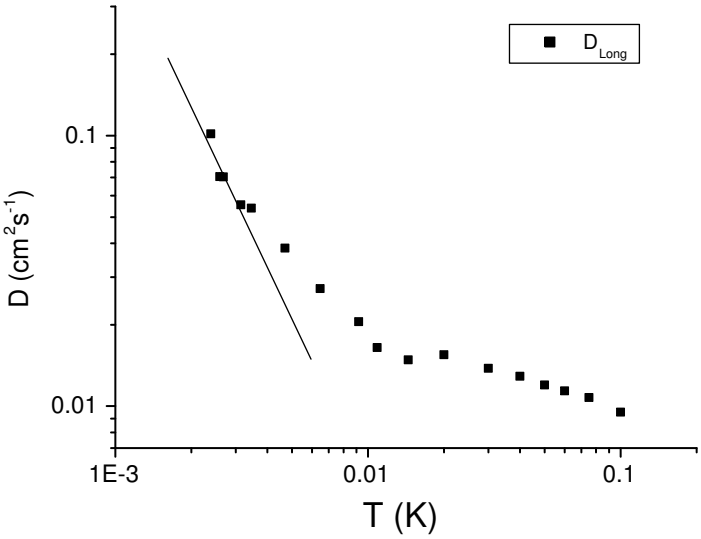

Figure 4.2: Longitudinal diffusion coefficient for pure ^{3}He. The line indicates a slope of T^{-2}

There is a significant difference between T_s for ^{3}He-^{4}He mixtures, and for pure ^{3}He. In mixtures, the surfaces tend to be coated by a layer of ^{4}He, which gives rise to a longer T_s than for pure ^{3}He, where a solid-like layer of ^{3}He covers the cell walls. For mixtures, including a 99.5% ^{3}He solution containing 0.5% ^{4}He, which acts as though it were a saturated mixture, the model of the surface relaxation process is one of diffusive motion of ^{3}He atoms in the surface layer of ^{4}He [47]. For this case, the surface relaxation time increases as B^2. For experiments carried out in mixtures at 11.3 T, it is therefore assumed that the dominant relaxation mechanism is the dipolar-interaction effect. Thus according to

$$\frac{1}{T_1} = \frac{1}{T_s} + \frac{1}{T_{bulk}} + \frac{1}{T_{||}}$$

the measurements of T_1 (and hence $\tau_{||}$) herein should be a true reflection of the longitudinal relaxation time ($T_{bulk} \sim 1000$ s [26]).

The data for the 0.7% mixture are presented in figure 4.3. The slope of the points at low temperature is close to unity, in contradiction to initial

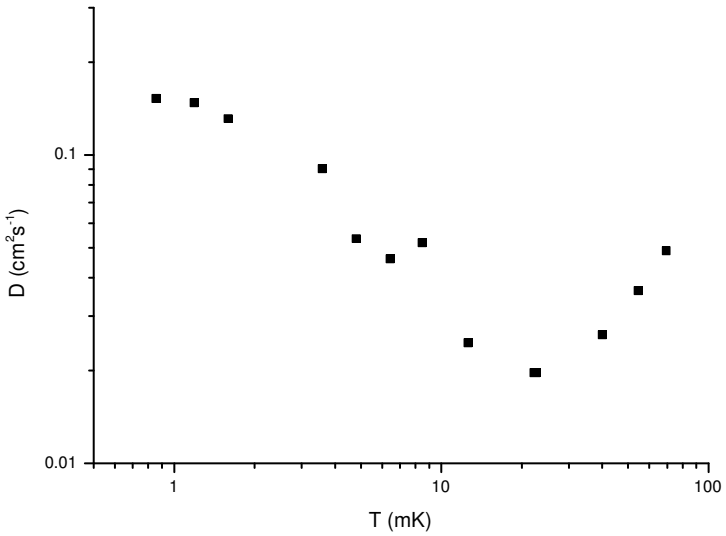

Figure 4.3: Longitudinal diffusion coefficient for 0.7% ^{3}He-^4He mixture

expectations. However, the Fermi temperature of such a mixture is $\sim$ 35 mK, and true Fermi-liquid behavior would not be expected until $\sim$ 4 mK or lower.

Spin-Echo Analysis

With his paper of 1970 [8], Leggett laid the foundations for the analysis of spin-echo data. Leggett demonstrated in his paper that, in the case of a strongly interacting Fermi liquid, the classical equation

$$D\nabla^2 M + \left(\frac{\partial M}{\partial t}\right) + \gamma\,(M \times H) = 0$$

could not be used, and that the corresponding equation for the echo attenuation

$$A(t) = \exp(-\frac{1}{12} D\gamma^2 G^2 t_0^3) \tag{4.2}$$

was incorrect for the general case. Although equation 4.2 is valid for some experimental conditions, in the collisionless regime the molecular field introduces non-linearities which result in a non-exponential envelope described by

$$\ln h - \frac{\frac{1}{2}(\mu M_0 \sin\phi)^2}{1 + (\mu M_0 \cos\phi)^2}(1 - h^2) = -\frac{2}{3} D_e \gamma^2 G^2 \tau^3 \tag{4.3}$$

where h is the ratio of echo height to initial pulse height, ϕ is the initial tipping angle, G is the linear field gradient, and τ the delay between the initial pulse and $\pi-$ pulse. The spin-rotation parameter, μM_0, was calculated to be related to the spin echo magnitude and phase shift $\Delta\theta$ between subsequent echoes by

$$\Delta\theta = \mu M_0 \cos\phi |\ln h| \tag{4.4}$$

Using these equations, and measuring both the phase shift and the echo height during the experiment, it is possible to determine the spin-diffusion parameter, and μM_0. The first published results to come from the experiments performed during this work ([25],[26]) used equations 4.3 and 4.4. The graphs in the following sections present the diffusion coefficient and spin-rotation parameter for pure ^{3}He, 6.2% mixture and 0.7% mixture (unpublished). The anisotropy temperature was determined from an empirical fit of the effective diffusion coefficient:

$$D_e = \frac{A}{(T_a^2 + T^2)}$$

and the value of μM_0 was likewise used:

$$\mu M_0 = \frac{B}{(T_a^2 + T^2)}$$

The value of T_a determined from the spin-rotation parameter was used as a qualitative check on the one obtained from the diffusion coefficient, as the uncertainties in μM_0 were greater. This is due to the fact that the phase determined from the spin-echo is very sensitive to the actual shape of the echo, which was distorted by the finite size of the cell, and the presence of spin-wave modes in the cell.

4.2 Results

4.2.1 Initial Analysis

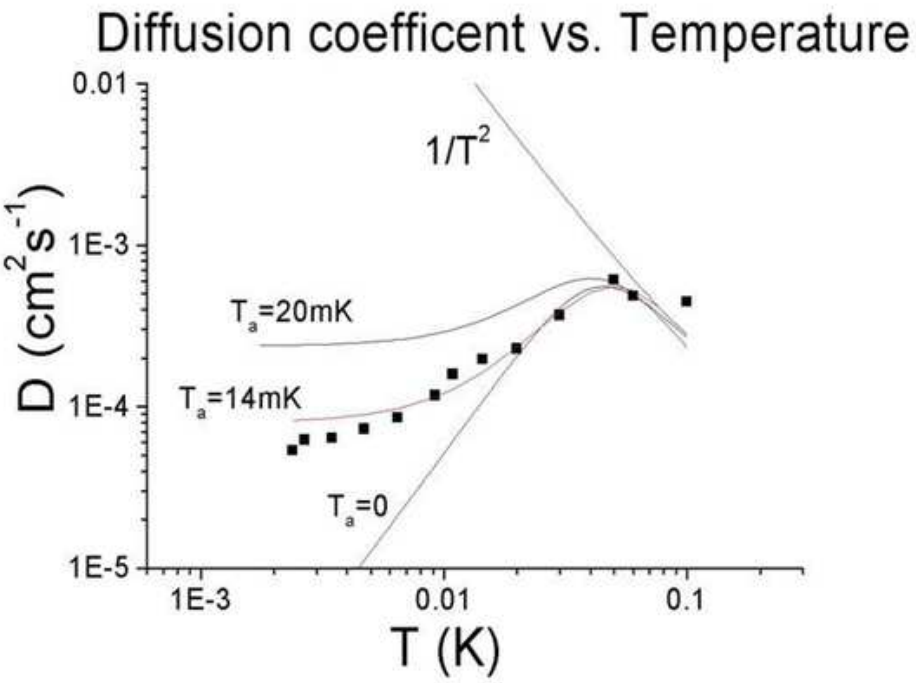

Figure 4.4: Effective transverse diffusion against temperature for pure ^{3}He. There appears to be clear saturation at low temperatures

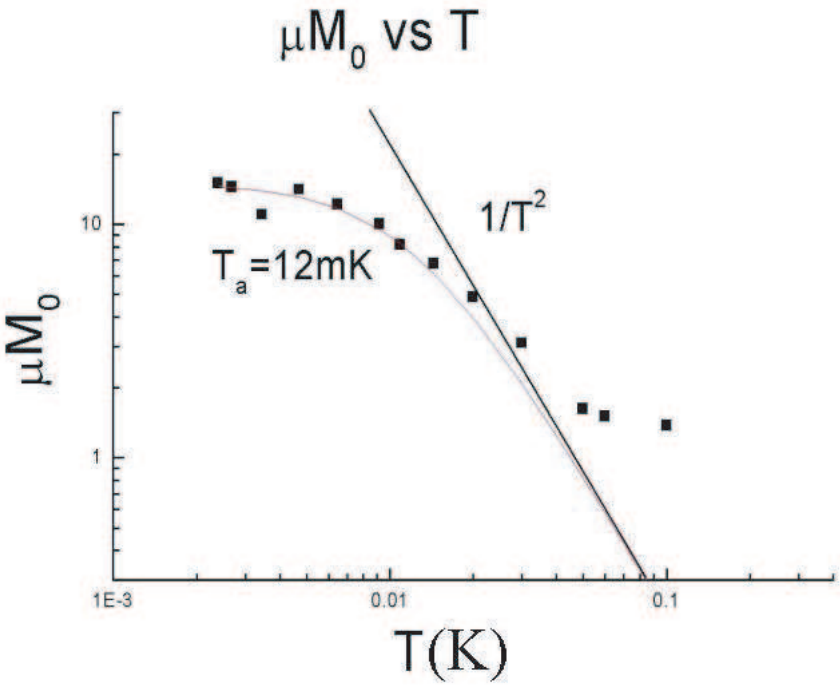

Figure 4.5: μM_0 against temperature for pure ^{3}He. Again, saturation is seen at low temperatures

Pure ^{3}He The effective diffusion coefficient is plotted in figure 4.4, with the corresponding spin-rotation parameter values in figure 4.5. In the absence of diffusion anisotropy, the behaviour of D_e is predicted to follow a T^{-2} law at high temperatures, and T^2 at low temperatures, due to the smallness of μM_0 at high temperatures, and its subsequent increase as $T \to 0$. Thus the saturation observed in the graphs gives a clear indication that such a saturation does exist. The fits on both graphs produce an anisotropy temperature $T_a = 12 \pm 2$ mK, which, despite being the lowest finite value measured, was contrary to the results of Vermeulen and Roni [17]. Perhaps this is not surprising, considering that the simple (and erroneous) analysis used neglected several factors which were later considered, and which lower the value of T_a. Incorrect thermometry would give a similar result. Careful analysis of the thermometry used, indicated that the temperature measured by the vibrating wire was an accurate one. Attention should again be drawn to the analysis subsequently performed by Buu *et al.* [14] on this subject, which goes into great detail, and produces an identical conclusion.

6.2% Mixture The data from this mixture suggests an anisotropy temperature of 13±2 mK. The experimental conditions are identical with the pure ^{3}He, apart from the concentration change. The thermometry and heating effects are assumed to be unaffected by this change in concentration.

0.7% Mixture The fits for this temperature are included for consistency only; there are much bigger problems with the fits for this dilute mixture than for the other cases. The Fermi temperature of a solution with this concentration is ~ 95 mK, which implies true Fermi behaviour only below ~ 10 mK. As there are only several points below this temperature, the uncertainty in the fit is considerable, which accounts for the different values obtained from the spin-rotation parameter and the diffusion coefficient. As with the 6.2%

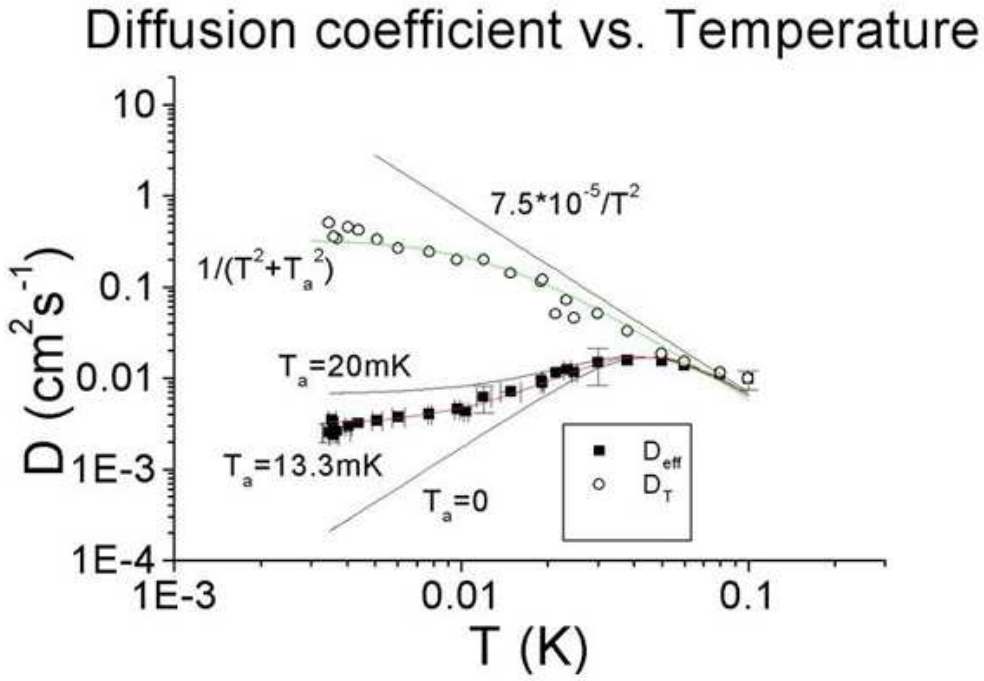

Figure 4.6: Diffusion coefficient against temperature for 6.2% mixture

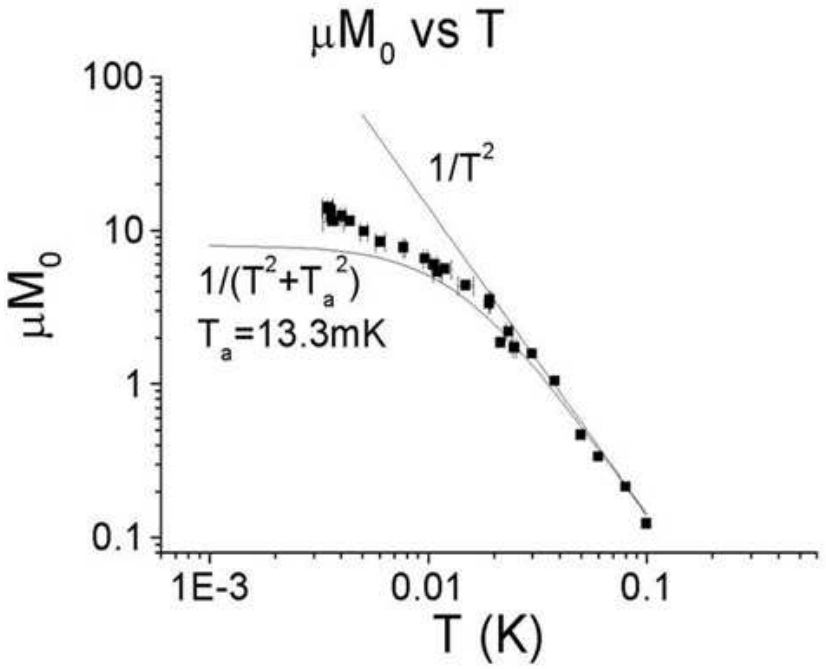

Figure 4.7: μM_0 against temperature, 6.2% mixture

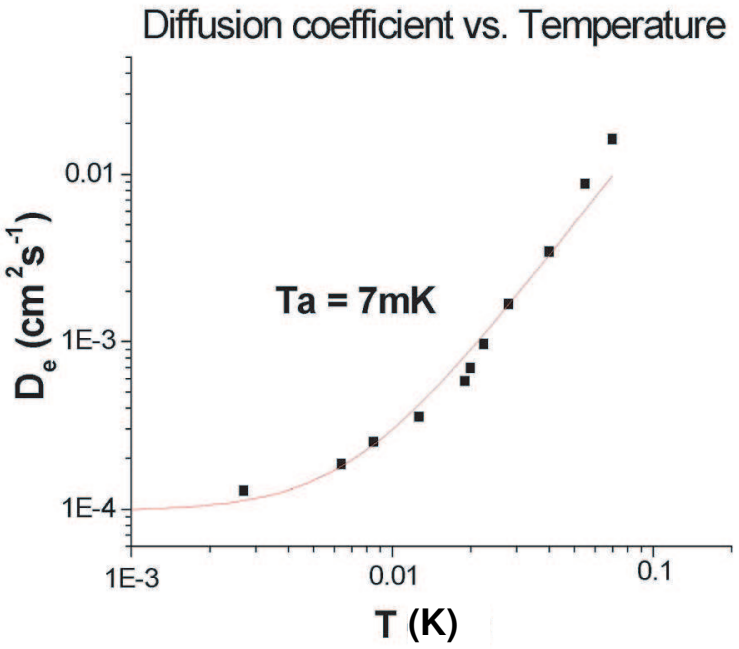

Figure 4.8: Diffusion coefficient against temperature, dilute (0.7%) mixture. The fit is for consistency with the previous graphs

mixture, there were no observable difficulties, specifically related to the low concentration, with the thermometry or heating effects of r.f. pulses. The vwr was still in the hydrodynamic regime, and as such could be used with confidence in the temperature ranges displayed in figures 4.8 and 4.9.

4.2.2 Modified Analysis

Spin-wave Spectra

The NMR spectrum of the cell is unchanged between 100 mK and 200 mK. At these temperatures the spectrum is that shown in the inset of figure 4.10. The broad peak on one side of the spectrum derives from the existence of a non-linear field gradient, which could not be compensated for by the use of shim coils. This is an unfortunate experimental artifact, which renders the analysis of the spectra significantly more complex. As the temperature of the cell is reduced, so peaks begin to appear in the spectra, as seen in figure 2.5. The width of these peaks diminishes as the temperature is reduced, whereas their spacing remains constant. The number of peaks in the spectrum increases

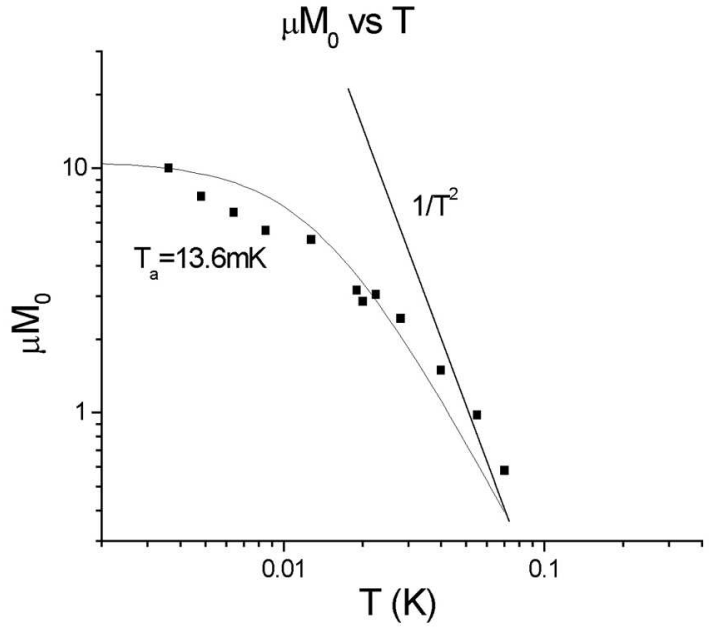

Figure 4.9: μM_0 against temperature, 0.7% mixture. The fit is for consistency with the previous graphs

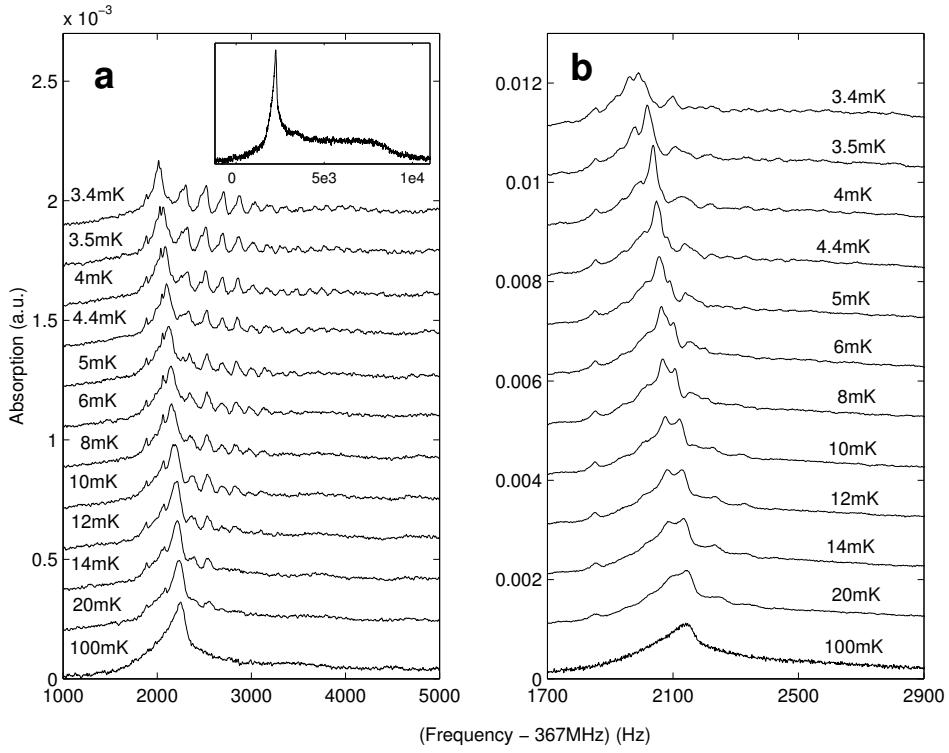

Figure 4.10: NMR absorption spectra. (**a**) 6.9 G/cm (**b**) +1.7 G/cm. Vertical shift is for clarity only. The insert is the lineshape for $T = 100$ mK

with the applied gradient. These facts imply that the peaks represent Silin spin-wave modes.

The analysis of these modes, in the Grenoble experiments, is what leads Vermeulen and Roni to determine that there is no spin wave damping due to the polarisation of ^{3}He-^{4}He mixtures [17], in agreement with Fomin, and in direct contrast to the data produced by several other experimental groups (see table 1.1). The analysis of Vermeulen and Roni uses the fact that the quality factor (Q) of the spin wave modes is a product of the Landau molecular field $\lambda\omega$, with the transverse quasiparticle collision time $\tau_\perp$. Similar methods have been attempted at Nottingham to analyse the spin-wave modes, but the conclusions are qualitative, rather than quantitative, due to the presence of the stray field gradient in the experimental cell.

A further difficulty particular to the Nottingham experiments is caused by the presence of the filling capillary. When the gradient is reversed from its 'normal' direction (i.e. in opposition to the main field), the spin-wave modes are partially suppressed. This indicates that, when the field gradient confines the spin wave modes to the bottom part of the cell, some transverse magnetisation leaves through the capillary. This effect can be seen graphically in figure 4.11.

Thus diffusion experiments for this particular case are restricted to one direction of field gradient only. For weak field gradients the data were less reproducible, implying that the stray field gradient was affecting the spin-wave modes to a relatively greater extent. Using strong field gradients minimised this problem; there is, however, no guarantee that the stray gradient did not cause inhomogeneous broadening of the spin-wave mode peaks. This limited the useful information that could be derived from the spin-wave spectra, as transverse relaxation time cannot be measured from the positions of the peaks, but only from their widths. Numerical solutions of eq. 2.14 can be

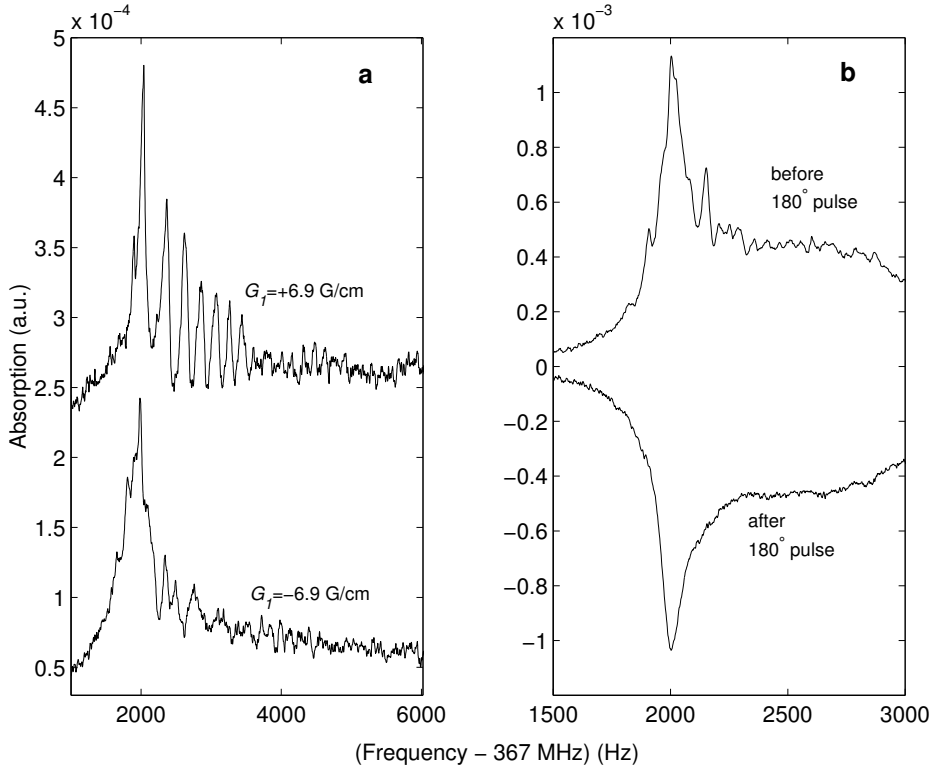

Figure 4.11: NMR absorption spectra at T =3.5 mK (vertical shift is for clarity only). (**a**) Opposite field gradients (**b**) $G = +1.7$ G/cm

used to determine a value for the spin diffusion coefficient. The solutions depend on the two dimensionless parameters μM_0 and $b_L = \gamma G_1 L^3 \mu M_0 / D_\perp$. b_L, G_1 (linear field gradient) and the Larmor frequency at the cell centre γB_0, were determined by a least-squares fitting of the frequencies of the first 14 modes to the experimental data. Reasonable fits were obtained, giving values of b_L=10592 Hz, G_1=10.5 G/cm and γB_0=5690 Hz. The value of G_1 was larger than that specified by the magnet manufacturer, but agreed with the value obtained from fitting the NMR lineshape at 100 mK.

A further improvement on this analysis was made by modelling the stray field gradient as a quadratic:

$$B(z, r) = B_0 + G_1 z + G_2(z^2 - \frac{1}{2}r^2)$$

The second-order term introduces radial eigenmodes. The longitudinal and radial degrees of freedom decouple, allowing a solution of the equation of spin-motion to be obtained. For further details, the reader is directed to

reference [58]. The result was an enhanced fit to the experimental data, providing values of b_L=5658, $b_2 = G_2L/G_1 = 0.23$, and $\gamma B_0 = 4877$ Hz. The fact that the exact field distribution in the cell was not known, however, prevents a quantitative analysis of the spin-wave spectra.

Spin Echoes

The initial analysis of the spin-echo data was flawed for several reasons. Leggett's equations are derived for the case of dilute mixtures, and assuming an infinite geometry. The geometry of the cell therefore becomes significant for circumstances where the length scale of the interactions becomes comparable to the dimensions of the cell: it has been shown that the effect of finite size in ^{3}He-^{4}He mixtures can be to mimic the saturation of transverse relaxation at low temperatures [39]. To correctly interpret the data a model has to be created which allows calculations of spin-wave spectra and spin-echo signals for a cylindrical geometry. In addition to the finite size corrections, work was performed on the stray field gradient to determine its significance on the results. The analysis of both effects, and the final result of that analysis, are covered in the following sections.

The starting point for this analysis is the usual linearised equation of spin-motion (eq. 2.14). Solutions of equation 2.14 are sought for a cylinder of radius R and length $2L$, where the axis is parallel to the applied field. For a 6.2% mixture the effects of the demagnetising field are assumed to be negligible. Thus, the local field in the Larmor frame of reference is simply $B(\mathbf{r}) = G_1 z$. The walls are assumed to be perfectly reflecting, giving a boundary condition $(\widehat{\mathbf{n}}.\nabla)\, m_- = 0$, with $\widehat{\mathbf{n}}$ the unit vector perpendicular to the wall. As has been mentioned previously, for a 6.2% mixture, the sign of the spin-rotation parameter is negative, corresponding to modes which seek a field maximum. The length scale relating to the equation of spin motion is the 'dephasing length', $L_g = \left[|D_e|/(\gamma G)\right]^{1/3}$, which is the distance over which

a spin must travel for a phase shift of 2π. The ratio of L/L_g delineates the boundary between the fast ($L/L_g \gg 1$) and the slow ($L/L_g \ll 1$) diffusion regimes in a classical ($\Omega_{int}\tau_\perp = 0$) gas. A positive value of $\mu M_0 = \Omega_{int}\tau_\perp$ means that the minimum field-seeking modes are favoured. Conversely, a negative value will favour maximum field-seeking modes.

There are three types of mode to consider in terms of the cell geometry: upper edge modes are confined near the upper wall and are unaffected by the lower; lower edge modes are confined close to the lower wall; and bulk modes, which are localised in the centre of the cell, and which are not influenced by either wall. In practice, this means that, for example, minimum-seeking modes have an oscillatory wave function between the boundary wall and the confining potential, and an exponentially-decaying wave function above the confining potential. A finite value of μM_0 has another effect upon spin echoes, namely that of shifting the phase of the echo. This is because, following the π pulse the molecular field is reversed ($M_0 \rightarrow -M_0$), and the isochromats 'see' a slightly different field to that before the π pulse. The timing of the echo is also slightly shifted in the case of our experiment. This is due to the presence of a second-order field gradient, and this effect has been confirmed by numerical studies. The echoes are delayed for a negative value of μM_0 (as obtained in pure ^{3}He, and 6.2% ^{3}He-^{4}He mixtures), and advanced for a positive value (as obtained with dilute mixtures). The variation of λ, and hence μM_0, with concentration x, is shown in figure 4.12. An example of delayed echoes due to the stray field gradient can be seen in figure 4.13.

Moving on to the specific case of a spin-echo experiment, it can be shown that there are three significant length scales, and three corresponding regimes. The dephasing length L_g is now compared with the diffusion length $L_d = (|D_e|\, t_e)^{1/2}$, and the length of the cell $2L$, where t_e is the time between the initial pulse and the π 'flipping' pulse. The three regimes are free diffusion ($L_d \ll L_g, L$), motional narrowing ($L \ll L_d, L_g$) and localisation ($L_g \ll$

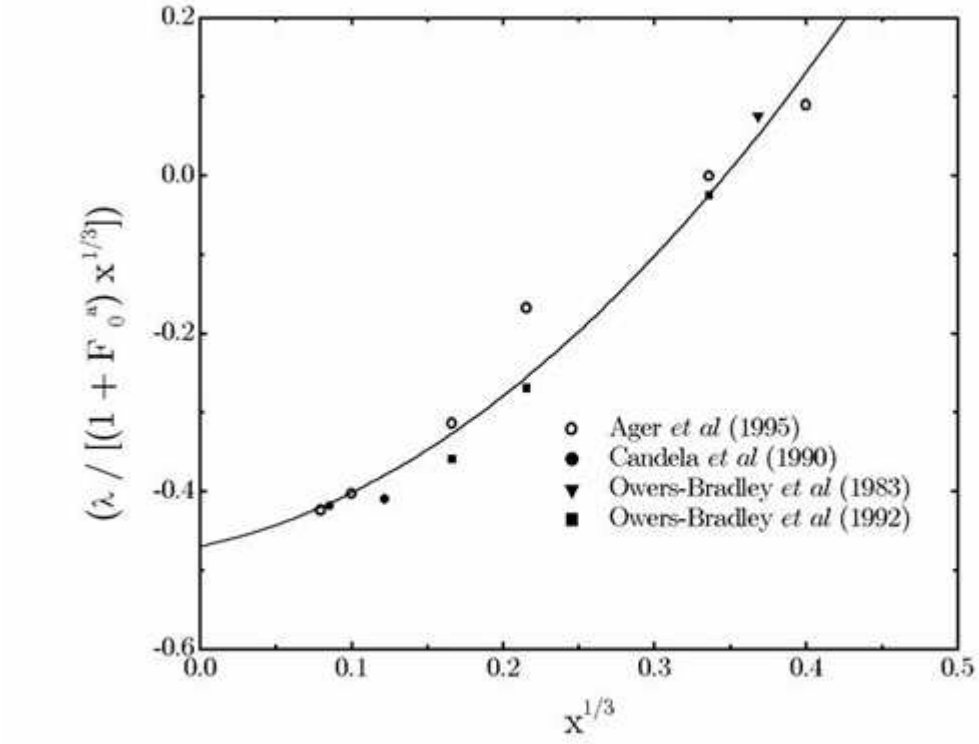

Figure 4.12: Concentration dependence of $\lambda/1 + F_0^a$ using values obtained from various authors (after *Naish* [52])

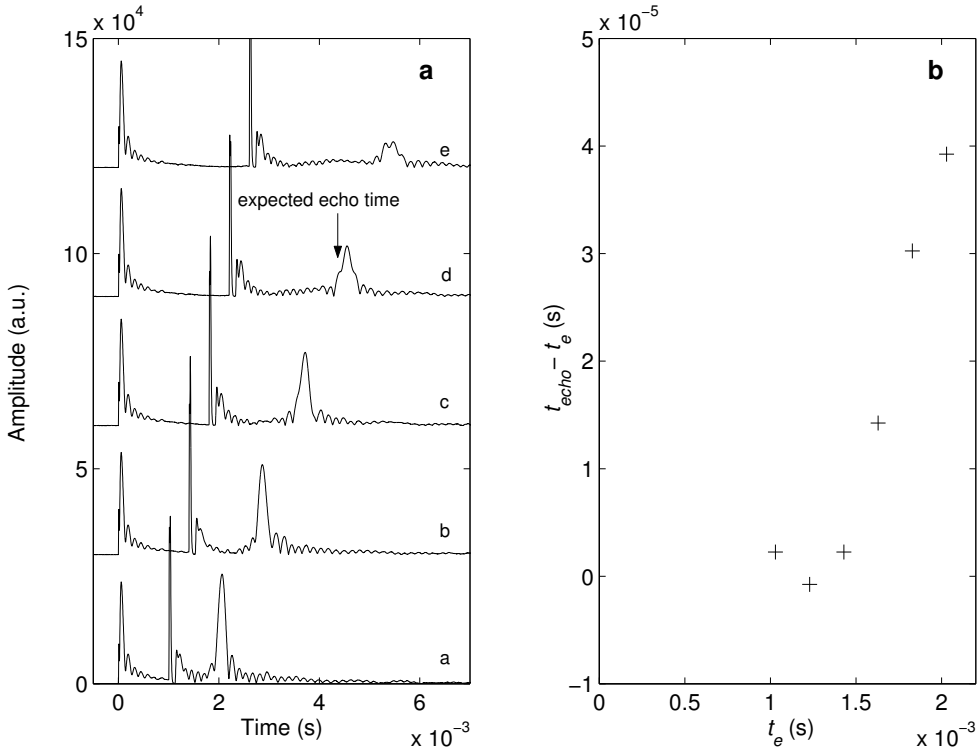

Figure 4.13: Graph demonstrating the delay of the echo with respect to the calculated echo time.

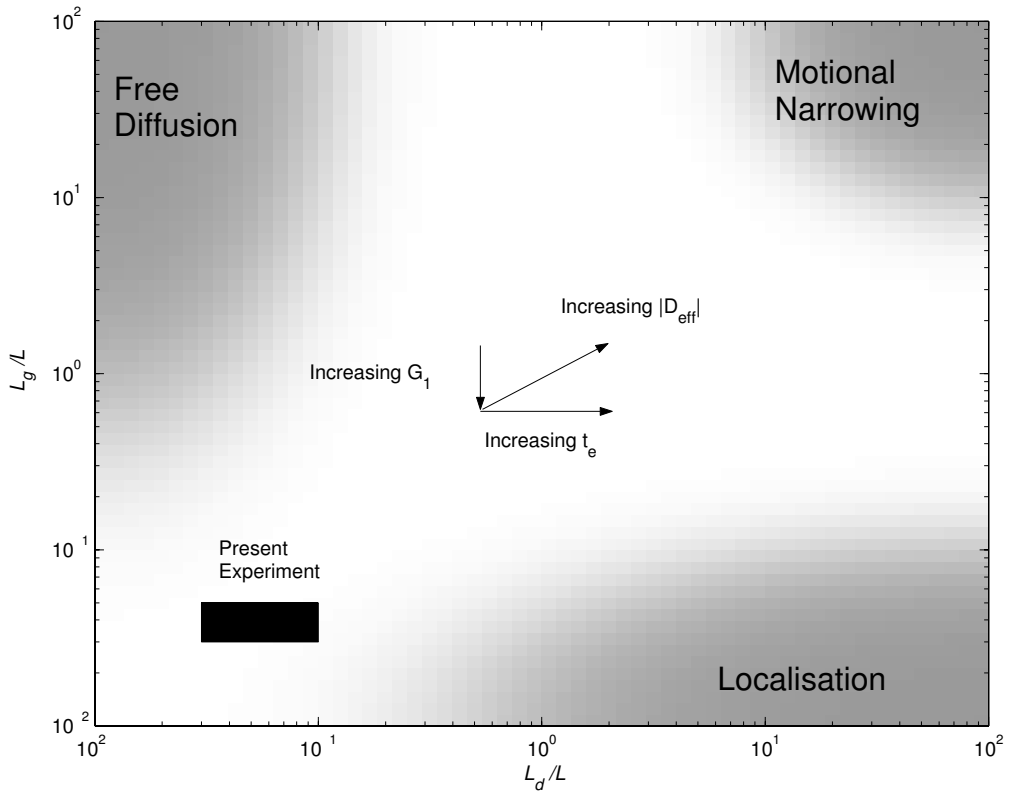

Figure 4.14: The three regimes of spin-echo attenuation: Free diffusion ($L_d \ll L, L_g$), motional narrowing ($L \ll L_d, L_g$), and localisation ($L_g \ll L, L_d$). There are smooth transitions between the regimes

L_d, L). These regimes are plotted in figure 4.14.

Consider $L_d \ll L_g, L$, or free diffusion. Here the quasiparticle lifetime is insufficient for the spins to interact with the boundary walls. In this case, Leggett's echo attenuation equation 4.3 gives the correct value for the echo magnitude. For $\mu M_0 = 0$, the equation simplifies to the classical echo attenuation relation. For quantum fluids, the phase of the echo is again given correctly by Leggett

$$\phi = -\mu M_0 \ln h \tag{4.5}$$

In the experiments at Nottingham, this case was rarely encountered due to the small dimensions of the cell, and the relatively low temperatures which increase the quasiparticle lifetime. The model created by Buu *et al.* [39] provides the relevant quantitative analysis for the spin-echoes accounting for the restricted diffusion and finite r.f. pulses used in the experiment. The

graphs displaying the modified fits, for both μM_0 and $D_\perp$ are seen in figure 4.15. The high-temperature points are not included in the fits, as the model does not extend accurately to these temperatures.

Although there are still differences between the results of this analysis and those of previous experiments, the essential point is that there is deviation of the curves from a T^{-2} dependence. The values of μM_0 and b_L (from which the value of $D_\perp$ is derived) are obtained by a least-square fitting of the data to the model ($b_L = \gamma G_1 L^3 \mu M_0 / D_\perp$). This was performed three times for each data point, each time using a different value for the stray field gradient. The values of μM_0 and b_L were obtained from the average of the three sets of parameters, with the error bars being the extremal values of the parameters. The relative uncertainty for $D_\perp$ was taken as the sum of those for μM_0 and b_L.

The fits of the data from the model provide values of $T_{aD} = 6.0 \pm 1$ mK and $T_{a\mu} = 6.2 \pm 0.7$ mK. These are significantly smaller than those values obtained using the simple Leggett-Rice result. The value of b_L is a very significant indicator as to whether restricted-diffusion effects have a significant impact on the measured values of μM_0 and $D_\perp$. It has been shown [39] that the limit for this effect is $b_L^{1/3} \simeq 1$. Knowing the experimental conditions for previous results, it is also possible to infer whether similar effects could have caused erroneous values for other groups. For the 6.2% mixture described herein, $b_L^{1/3} \simeq 23$, and for the data of Ager *et al.* [24] $b_L^{1/3} \simeq 13$. The apparent saturation of the spin-rotation parameter from purely restricted-diffusion effects for Ager *et al.* has been calculated as 12 mK, significantly less than that concluded by their experiments. This effect becomes less for the pure ^{3}He experiments of Wei *et al.* [23] ($b_L^{1/3} \simeq 43 \rightarrow$ apparent $T_a = 3$ mK for 8 T) and Candela *et al.* [26] ($b_L^{1/3} \simeq 80 \rightarrow$ apparent $T_a = 2$ mK for 11.3 T), and negligible for the dilute solutions of Akimoto *et al.* [27] ($b_L^{1/3} \simeq 110$)

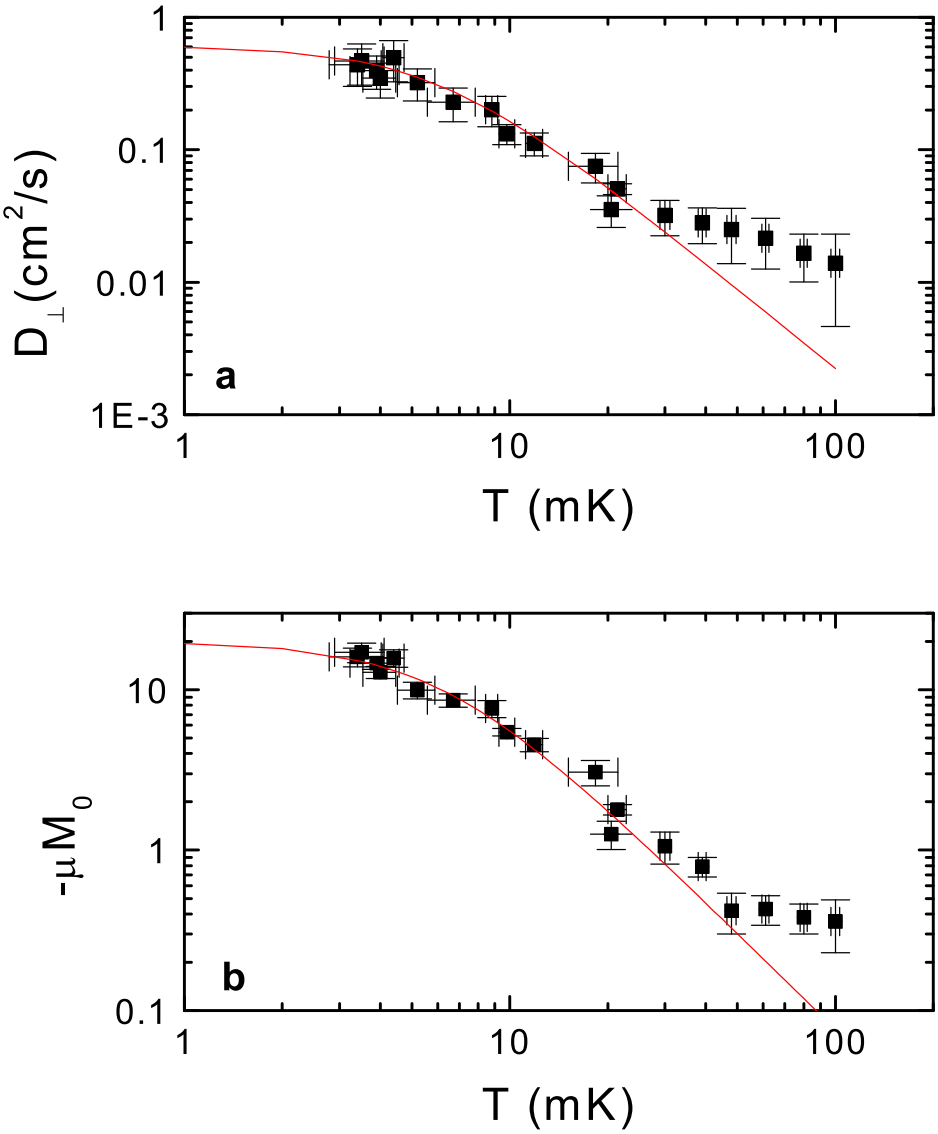

Figure 4.15: **a**: Transverse diffusion coefficient against temperature, to the fit $D_\perp = A/(T^2 + T_a^2)$ with A=22 cm^{2}s^{-1}mK^2 and T$_a$=6.0 mK. **b:** Spin rotation parameter against temperature, to the fit $\mu M_0 = B/\left(T^2 + T_a^2\right)$ with B=765 mK^2 and T_a=6.2 mK

and the 0.7% solution used in our experiments ($b_L^{1/3} \simeq 214$). Thus there can be reasonable confidence in the results outlined above, in terms of the restricted diffusion effects. What may be a far more complex question, is to what extent the demagnetising field plays a part in the determination of the relevant quantities. Until the necessary theoretical analysis is performed, it is impossible to reach a conclusion as to how valid are the results for pure ^{3}He.

Chapter 5

High-Field Thermometers

5.1 Background

The experiments performed by the ULT group at Nottingham typically take place in a field of 11.3 T and a temperature range of 1-100 mK. This presents a unique set of challenges for thermometry which rules out most commonly-used methods. It is from this perspective that the investigation of damping of quartz tuning forks, and the capacitance of plastic films, was undertaken. The viscosity of ^{3}He and its mixtures is known to vary as T^{-2} as $T \rightarrow$ low millikelvin temperatures, and this fact has been used to relate the damping of the amplitude of the tuning fork, and its frequency shift, to the temperature of the experimental cell. Quartz tuning forks have been used as timing devices, for example in wristwatches, for many years. They are ideally suited to this purpose as they have a very high intrinsic Quality factor(Q), of the order 500 000 at low mK temperatures under vacuum, and a frequency $f_{tf} = 2^n$, where n is typically 15 or higher. Using simple electronic components (e.g. J-K flip-flops) these frequencies can be divided to reach the desired output, normally 1 Hz. The reason for the high Q is the fact that the oscillations are symmetric about the centre of the base. This symmetry minimises the strain at the base of the fork, and hence minimises the mechanical damping of the fork. The frictional losses associated with this type of oscillation in quartz are also extremely low. Their ubiquitousness provides another advantage of

their use; they are very cheap (£0.20 each) and have extremely reproducible characteristics due to the consistency required for their use in reliable timing circuits.

The second type of thermometer investigated was the plastic film capacitor. Capacitors are field-independent and simple to construct and operate, though their disadvantages include lack of sensitivity and requirement for calibration. The dielectric permittivity varies with temperature, and the shape of this curve qualitatively follows the same shape for different choices of plastic. The ideal thermometer would have the greatest temperature sensitivity between 1 and 15 mK, and the experiments performed were to determine the suitability of the plastic selected.

Listed in the following sections are some of the choices of thermometer available, and the reasons for their unsuitability in the case of the experiment at Nottingham. In cases where the thermometer type has been used for the experiments detailed in this thesis, experimental details are also included.

5.1.1 ^{3}He Melting-Curve Thermometer

The melting pressure of ^{3}He has an extremely well-defined temperature dependence, and this has enabled it to be used in melting-curve thermometers (fig 5.1). ^{3}He does exhibit a slight field sensitivity, but this is well known and does not cause a problem for thermometry, particularly as several fixed points are available at low temperatures where the superfluid transitions take place. The advantages of such a system include very high resolution (of the order of 1 μK) and reproducibility, near-zero power dissipation and insensitivity to r.f. radiation. The disadvantages are the relative effort and cost of production and the need to have a gas-handling system.

A melting-curve thermometer is an impractical choice for our experiments, because the additional difficulty of incorporating it into the experimental

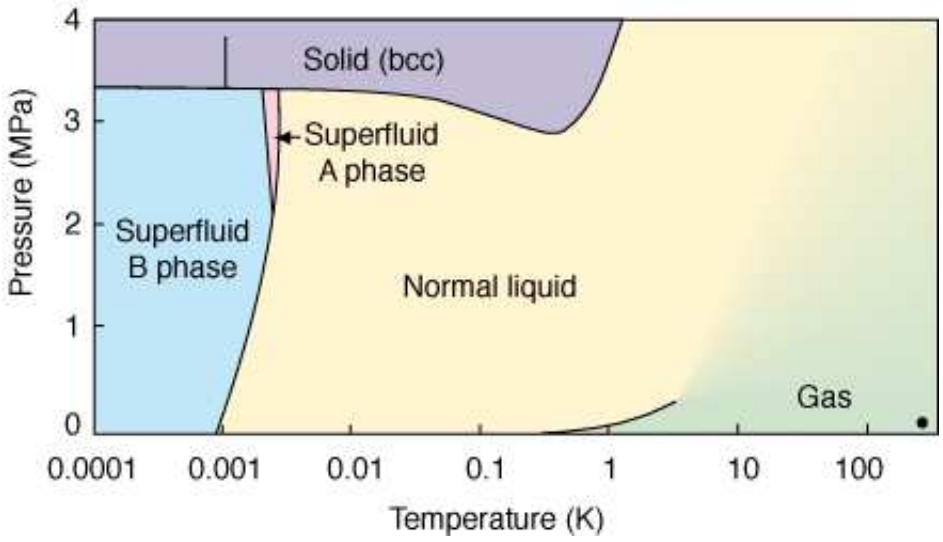

Figure 5.1: Phase diagram for ^{3}He

setup is not justified by the advantages offered when compared to other methods, in particular viscometry.

5.1.2 Coulomb Blockade Thermometer (CBT)

A relatively recent innovation in thermometry, the Coulomb Blockade Thermometer (CBT) is a primary (and secondary) thermometer which measures the conductance drop across a given number of tunnel junctions. The full width at half height is directly proportional to the temperature and is the primary temperature parameter (fig.5.2). The depth of the curve can be used as a secondary thermometer.

This thermometer is a commercially-produced system (e.g. Nanoway, Jyväskylä, Finland) which has an impressive range (∼20 mK- 30 K) and a field independence which has been tested to 30 T. The obvious disadvantage is its lower temperature limit. This is a consequence of the self-heating of the thermometer due to poor electron-phonon coupling. It is planned to install a CBT thermometer on the stage; this, however, does not solve the problem of thermometry at lower temperatures.

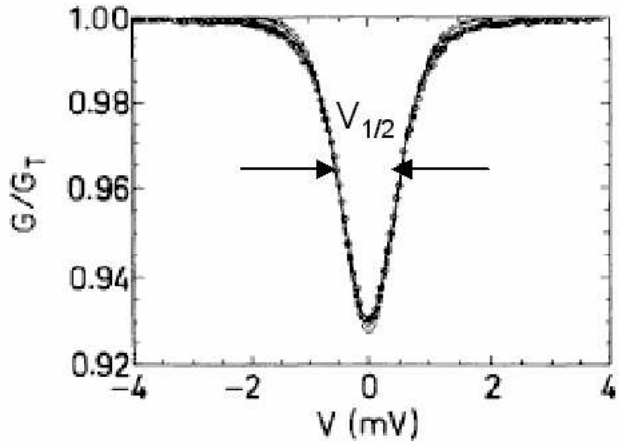

Figure 5.2: Typical conductance curve for a CBT system, $V_{1/2} \propto T$ (Primary) and $\Delta G/G_T \propto T^{-1}$ (Secondary)

5.1.3 Platinum NMR

To measure the temperature using our platinum NMR thermometer, the magnitude of the magnetic susceptibility is measured. This is done by measuring the integrated signal of an FID. The magnitude of the integrated signal is inversely proportional to the temperature. The magnetic susceptibility of platinum is believed to obey the Curie law ($\chi \propto T^{-1}$) down to μK temperatures, which makes this method of thermometry useful, in principle, down to the lowest temperatures currently attainable in dilution fridges equipped with demagnetisation stages. Unfortunately, a high applied field has significant effects on both NMR (e.g. Larmor frequency) and the metal itself (e.g. heat capacity), and this gives rise to particular problems.

In general, platinum NMR is based on a commercially-available system (e.g. PLM-3 platinum NMR thermometer manufactured by Instruments for Technology, Espoo, Finland) using a static field of 28.4 mT. This gives a Larmor frequency $f_0 = 250$ kHz. On application of a much higher field, however, both the heat capacity of the Platinum, and its Larmor frequency, increase significantly. In 10 T the heat capacity increases by a factor of 10^5 which

means much greater thermal equilibrium times. The use of a stronger magnetic field increases the signal ($\chi \propto B$, $\omega_0 \propto B$) but decreases the size of the bulk material which can be used due to enhanced skin-effect problems (eq. 5.1)

$$\delta = \sqrt{\frac{2}{\omega\sigma\mu}} \tag{5.1}$$

where σ is the conductivity, and μ the permeability of the metal. The skin-depth effect has the effect of reducing the potential signal available due to space constraints. It has the additional effect of emphasising the surface signal, which suffers from greater inhomogeneities and defects than does the bulk metal. Although Candela and McAllaster [59] used a field of 8 T down to 8 mK to successfully measure the temperature of platinum wire with very reasonable thermal equilibration times (< 20 s), the heat capacity of the platinum varies as $(B/T)^2$. For 11.3 T and 1 mK this implies another factor 128. Whilst a careful compromise between sample size and equilibration times was possible for the higher temperatures and lower fields mentioned, it seems highly unlikely that such a satisfactory outcome would be possible for our experiments.

5.1.4 Noise Thermometry

Noise thermometry is an area where there has been much recent work in improving the temperature range over which it can be used (e.g. [60]). The principles, however, remain based on work done in the 1920s by Nyquist and Johnson. Random thermal motion of electrons in a resistor causes instantaneous voltage fluctuations which appears as noise, normally an irritant in experimental measurements. There is, however, a time averaged mean square noise voltage (eq. 5.2)

$$U_{rms} = \sqrt{\langle u_t^2 \rangle} \tag{5.2}$$

which is proportional to the temperature (eq. 5.3), and if this voltage can be detected the temperature can be obtained directly.

$$\langle V_N^2 \rangle = 4k_B TR \tag{5.3}$$

In practice the noise voltage is extremely small, and SQUIDs are generally used to detect it. Performance has been improved to the point where minimum electron temperatures of ~ 300 μK have been attained, with a sensitivity of better than 1% and a measuring time of ~ 10 s. As it can be used as a primary or secondary thermometer, noise thermometry would seem to be a very useful tool. Unfortunately, SQUIDs are extremely sensitive to magnetic field, and even were the SQUID to be situated outside the main field, it is certain that the cables would pick up additional induced voltage from the magnetic field. This would render the system far less sensitive to the very small noise voltages which need to be detected.

5.1.5 Capacitor

Capacitance thermometry relies on the change of the dielectric permittivity ϵ with temperature. This quantity is directly proportional to the capacitance, and in glasses and other amorphous substances (e.g. Mylar), it has a simple $\epsilon \propto -\ln T$ dependence [55], [56].

The capacitor has several advantages apart from its field independence. These can be broken down into ease of construction, cost, simplicity of measurement and low heat-leaks.

The method used to construct the thermometer was to solder a twisted pair of niomax wires directly to either side of a copper-plated Kapton sheet. The thickness of the copper was 35.5 μm, with the Kapton being 94 μm thick. The use of solder was an improvement on previous attempts to use silver DAG to affix the leads to the capacitor, which had suffered greatly from a lack of robustness, with the leads often becoming detached over several

thermal cycles. The rectangular capacitor was then rolled into a cylinder, with cigarette paper being used to isolate the two sides from one another. The rolling-up of the sheet increased the risk of accidental contact between the sides, but it was felt that this was a necessary risk in order to obtain the highest possible value of capacitance, and hence sensitivity. In total, the construction time for such a capacitor was of the order of a day. The cost of the materials involved is relatively slight, with only small amounts being used from large sheets available commercially.

Three techniques were investigated for reading the capacitor. The first method involved using a capacitance bridge was used to balance the lead capacitance, then reading the offset. The second used a 'precise' capacitance bridge (Andeen Hagerling ultra-precise capacitance bridge) at 1 kHz to measure the capacitance directly. The final method was to use an inductive divider to balance the sample capacitance against a reference capacitor. Overall, the most suitable choice was deemed to be the capacitance bridge. The internal reference capacitor has a high degree of thermal stability, noise levels were lower, and the ability to take measurements overnight was very valuable. The only disadvantage to this method over the other two was that the excitation frequency cannot be varied. As the capacitor response depends on the excitation frequency (fig. 5.3), it is possible that the most temperature-sensitive frequency would not be used for the measurements.

The heat leaks through a capacitor are low (unless grounding occurs) due to the lack of a constant current through a resistive path. Power dissipation in a capacitor is determined by the losses through it, and typical values in the region of interest (< 10 mK) are ~ 2.5 nS ($0.4\times10^9\Omega$). For an r.m.s voltage of 88 mV and using

$$\overline{P} = \frac{V_{rms}^2}{R} \tag{5.4}$$

a heat leak of 19.4 fW is obtained, which is insignificant compared with other sources.

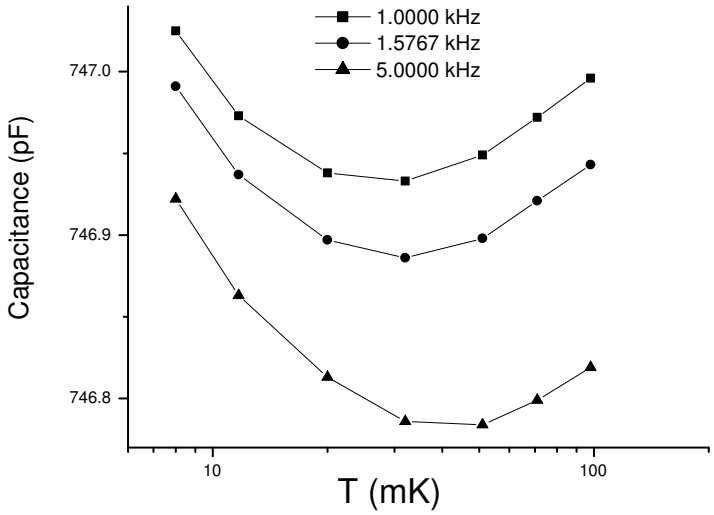

Figure 5.3: Capacitance against temperature for different values of measurement frequency (after *Naish* [52])

A variation on the capacitance thermometer would be to use two metallic contacts for the electrodes, with the Helium as the insulator [57]. This was considered in some depth, but rejected, as the physical structure required would have been too large to fit inside the Helium reservoir, and the number of electrical contacts available on the stage was limited.

In summary, whilst the disadvantages of this type of thermometry are too severe to consider relying on it as a principal thermometer, it has the potential to be a useful additional tool. The capacitor fulfils the requirements of field independence and has a reasonably good temperature range ($\sim 3 - 20$ mK). However, it needs calibration against a reliable thermometer at all temperatures, not just on first use, but after each thermal cycle, as the capacitance can vary between cycles. This drawback is mitigated significantly if the experiments carried out are of a long-term nature, e.g. many demagnetisations before returning to room temperature.

Results

The results of the measurements are plotted in graphs 5.4, 5.5 and 5.6.

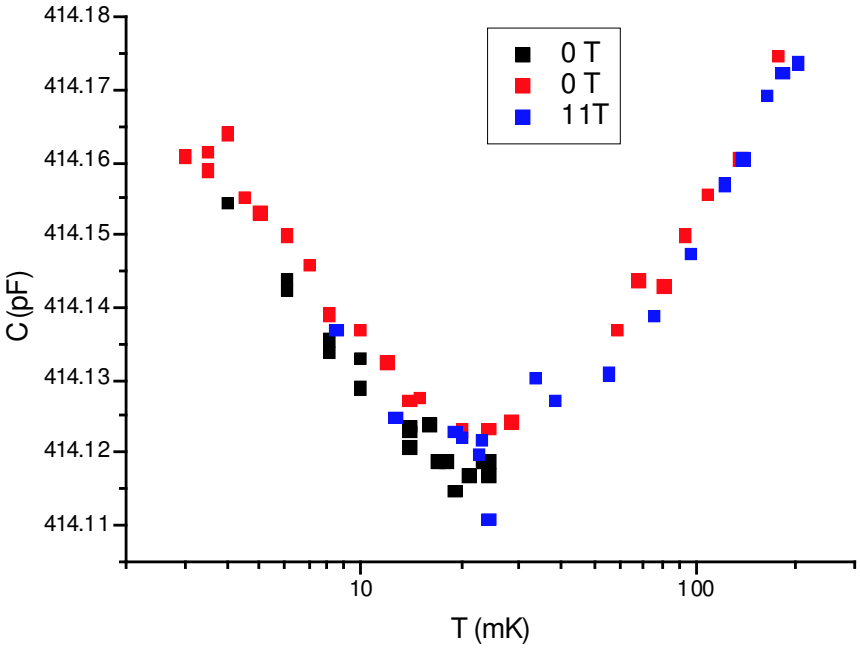

Figure 5.4: Capacitance against temperature, 0.1% mixture

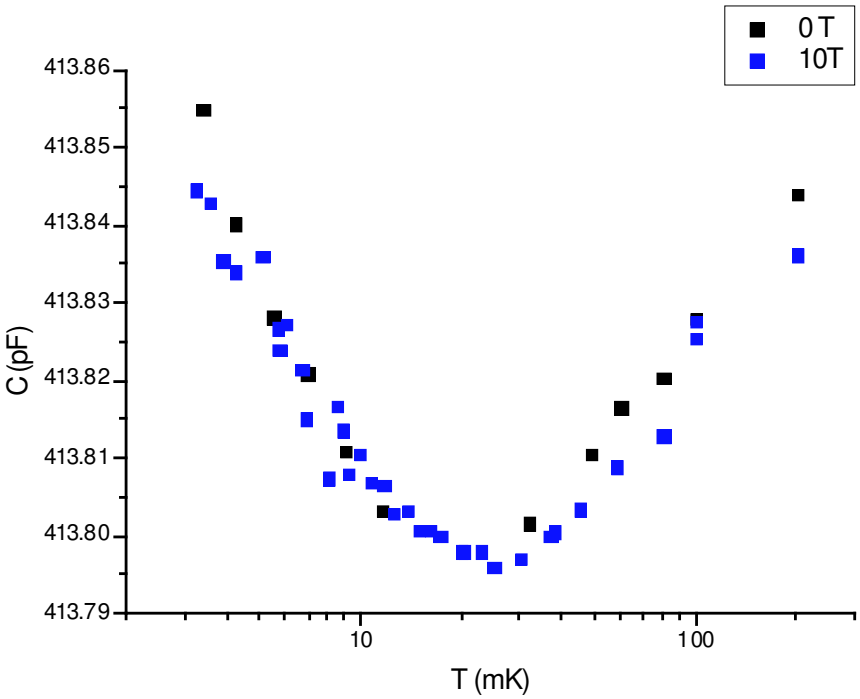

Figure 5.5: Capacitance against temperature, concentrated mixture

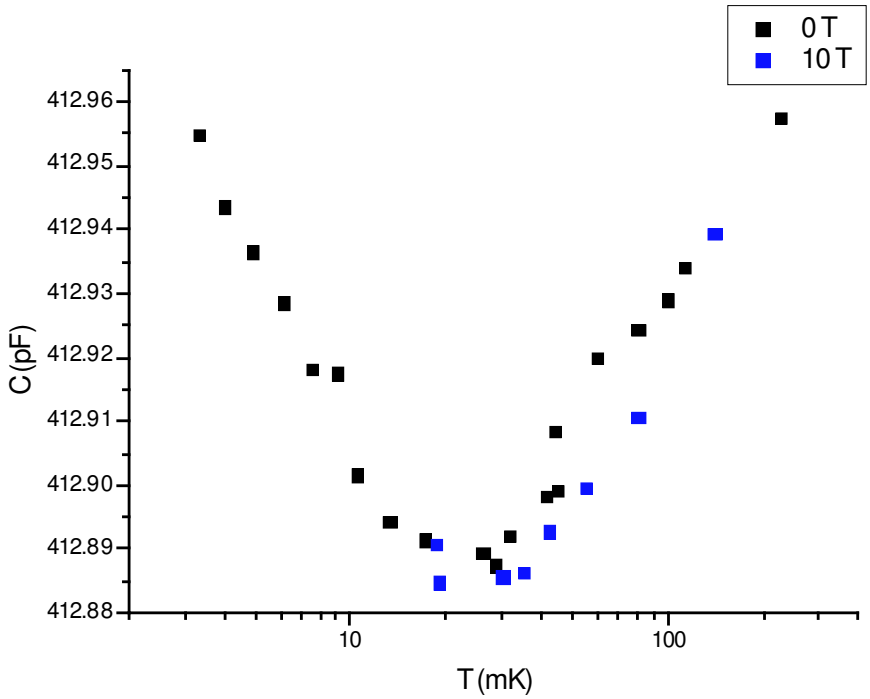

Figure 5.6: Capacitance against temperature, pure ^{3}He

5.1.6 Vibrating Wire Viscometers

At first glance, traditional viscometers, such as vibrating wire resonators (vwr's), would appear to be ideal. They are widely used for thermometry in ^{3}He and its mixtures, and can be used without calibration. They contribute little heat to the experiment and are relatively straightforward and inexpensive to construct. The damping of such resonators can be readily calculated, which means that calibration by a separate thermometer is unnecessary, once certain initial conditions (e.g. vacuum frequency) have been ascertained. The disadvantages of this technique to us are somewhat more subtle than the other methods, and it is worth discussing in some depth why there is difficulty in using vwr's in our experiment.

Initially the theory of a moving object in a fluid is considered. The force exerted on a cylindrical wire by an infinite, inviscous, irrotational, incompressible fluid is given by eq. 5.5

$$F_H = \pi a^2 \rho \omega^2 \mathbf{y} \left(k + ik'\right) \tag{5.5}$$

where A is the cross-sectional area, ρ is the density of the fluid, $\mathbf{y}$ is the displacement of the wire and k and k' are Stokes' dimensionless coefficients. The coefficients k and k' can be measured directly from the frequency shift and Quality factor of the vibrating wire:

$$\frac{\Delta f}{f_{vac}} = \left(\frac{\rho}{2\rho_{wire}}\right) + \left(\frac{\rho}{2\rho_{wire}}\right)(k-1) \tag{5.6}$$

$$\frac{1}{Q} = \left(\frac{\rho}{2\rho_{wire}}\right) k' \tag{5.7}$$

and from this the penetration depth δ, can be obtained

$$(1-k-ik')^{-1} = \frac{(1+i)\,a}{\delta}\frac{H_0^{(1)}(qa)}{H_1^{(1)}(qa)}$$

where $H_n^{(j)}$ are nth-order Hankel functions of the jth kind, a is the wire radius and, for viscosity η, $\delta = (2\eta/\rho\omega)^{1/2}$. To simplify,

$$Q^{-1} \approx \left(\frac{\rho_n}{\rho_{wire}}\right)\frac{\delta}{a}$$

Thus, to obtain a high Q, the wire radius or density needs to be increased. Unfortunately, the eddy-current damping increases with the radius and magnetic field:

$$\frac{1}{Q_{eddy}} = \frac{4B^2a^2}{\omega_0\rho_w\rho_r r^2} \tag{5.8}$$

The Q obtained therefore needs to be compromised with the fact that viscous damping will not be measured should eddy current effects become too severe. Another relevant factor to consider is the frequency of operation which should be around 10 kHz or less for best Q and induced voltage ($V_{ind} \propto 1/f$). The frequency of the wire can be calculated [61] using equation 5.9

$$\omega_0^{2\sim}\frac{Z_0^4 Y a^2}{4\rho_w L^4} \tag{5.9}$$

with Z_0=4.73.

The exact properties of the wire required is restricted by the range of wire available in the correct dimensions. Within these limits several factors may be varied to try to optimise the performance of the vwr, whilst reducing eddy

Material	Resistivity $\mu\Omega$cm	Density KgM^{-3}	Young's Modulus GPa
Manganin	45	8400	125
Bronze-Phosphorous	16	8780	90
CuBe	6	8260	120
Constantan	52	8900	150
Platinum-Tungsten	66.5	21300	120
Tantalum	13.5	16600	120
Tungsten	5.4	19300	120

Figure 5.7: Table showing useful physical properties of metals typically used in viscometry

current problems. Those parameters which can be selected, which affect the response of the vwr, are the radius a, length L, density ρ_w, Young's modulus Y, resistivity ρ_r, and drive current amplitude I. The relevant physical properties of the most commonly used metals used in viscometry are presented in table 5.7.

The most important part of the temperature spectrum for the vibrating wire is between $\sim$ 1 and 15 mK. Above this temperature, the superconducting fixed point transitions are used, which are extremely reproducible and accurate, and are now used as an international standard in low-temperature thermometry, and also a resistance thermometer. The aim was to produce a wire which would have a quality factor (Q) of about 5-10 at $\sim$ 1 mK, rising to about 500 at 10 mK.

The ideal metal for the purposes of our experiment is Platinum-Tungsten (PtW). Its resistivity is high which minimises the flow of eddy currents, and its density is also large which results in a better Q. Other high-density metals (e.g. Tantalum, Tungsten) suffer from superconductivity effects (flux motion inside the wire loop vastly reduces calculated Q) or have a low resistivity which allows high eddy current losses. It is straightforward to calculate the expected Q and eddy current Q for both pure ^{3}He and a 6.2% mixture. In table 5.8 the values are calculated for 2 mK.

Metal	Radius μm	Frequency kHz	Q Pure ^{3}He	Q 6.2% Mixture	Q_{Eddy}
PtW	62.5	10	20	110	1000
CuNi	62.5	10	10	80	600

Figure 5.8: Comparison of calculated Q values for PtW and CuNi wires, 2 mK, 10 T.

Unfortunately, PtW wire of the necessary radius was unobtainable. It was therefore decided to attempt to read a $\phi 125\mu$m Constantan (CuNi) wire at 10kHz and a $\phi 25\mu$m PtW wire at 5 kHz. The two wires were connected in series on the stycast washer which also housed the tuning fork (see fig. 5.14). The loop radius was 2 mm for the Constantan which gave a calculated operating frequency $f_{calc} = 11565$ Hz ($f_{\rm exp} = 12300$ Hz), and 1.0 mm for the PtW which gave $f_{calc} = 5000$ Hz ($f_{\rm exp} \sim 100000$ Hz). The vast difference between calculated and actual frequency for the PtW is a source of puzzlement. It might be that the measurement was not being made of the vwr itself, but of a stray lead in the thermometry cell.

These vibrating wires have been used for the 6.2% mixture. They were both a considerable disappointment. The small (PtW) wire was a significant source of heating and its use at low (< 5 mK) temperatures was discontinued. The large wire had a measurable but poor Q in the region of interest, and entered the ballistic regime where its sensitivity was minimised at low temperatures. Despite moves to fit the measurements of frequency shift and Q to the theory for this wire, it did not conform to the theory and its use as a thermometer was compromised.

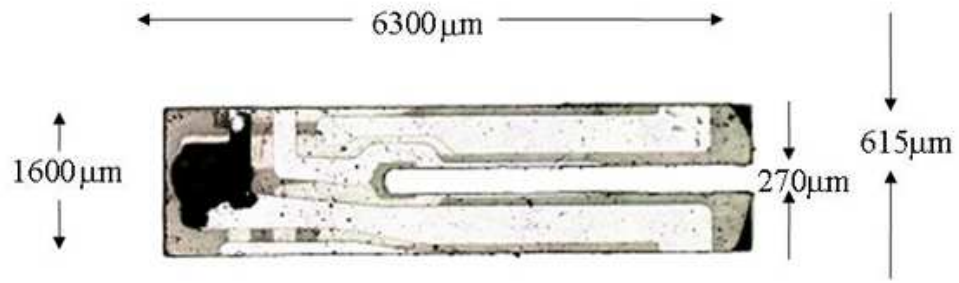

Figure 5.9: Close-up of tuning fork

5.2 Tuning Fork Experimental Details

5.2.1 Preliminary Tests

Tuning forks have been widely used in many different fields of microscopy [62] (e.g. scanning near-field acoustic microscopy, scanning near-field optical microscopy, scanning force microscopes, atomic force microscopes), and when used in this way the usual method of operation is for one 'tine' (beam) to be firmly glued to a massive body. The literature (e.g. [63]) demonstrates that Q values of up to several thousand in ambient pressures can be achieved, and for this method the system can be approximated to that of one tine oscillating. From the point of view of data analysis this is certainly an advantage over the double oscillation: the theory for a single oscillating cantilever is known [64], and used in this way the tuning fork has the potential to be used without calibration.

Initially the response of the fork on removal of one of the tines was investigated. For reasons of heat capacity, it was felt that the amount of matter in the cell which performed no essential function needed to be minimised. The addition of a massive object to improve the resonance would be detrimental in this case. This type of modified fork was tested in liquid nitrogen, cold nitrogen gas, cold helium gas and liquid helium. In no case of a removed tine was a resonance measured. This may have been due to the removal of electronic components which lie along both tines of the fork. Another reason

Substrate	Mass of Glued Object (g)	Q Air 300K	Q ^{4}He Gas 4.2K	Q ^{4}He Liquid	Q N_2 Gas 77K	Q N_2 Liquid
Silicon wafer	0.5	150	130	0		
Glass slide	5	4000	800	80	400	700
Silver washer	5	400	1200			600

Figure 5.10: Initial tests on a fork with one tine glued to a rigid object

may be that the Q was completely spoiled by the removal of an opposing mass. The next tactic was to glue one tine to a relatively massive object, as is done for microscopy. Initial attempts were made with a silicon wafer and a glass slide. The Q values obtained were very disappointing with the lighter Silicon, but increased on increasing the mass of the glued object. A summary of the results for forks with 1 tine glued can be seen in table 5.10.

Despite the comparatively good results obtained with the glass it was decided to use a silver washer in the cell. Glass would prove very difficult to work with, particularly as holes had to be drilled in order to incorporate a vwr. Silver was chosen, as its heat capacity would be acceptable to very low temperatures, compared with a similar amount of copper. This setup was created for use with the spherical NMR cell. Unfortunately, due to a very difficult procedure in inserting the cell the fragile quartz cell was always destroyed on insertion. After several attempts and breakages it was felt that the design of the cell should be modified to eliminate the need to remake the cell every time it was taken apart. It was felt that, in the new thermometry cell, a two-pronged fork could be used to increase the Q value. Tests therefore commenced in order to determine the suitability of an intact fork for use in our experiments.

Typical Q values for an intact tuning fork at STP are of the order 10000. In ^{4}He liquid a Q of $\sim$ 1000 was obtained, with a Q of several thousand

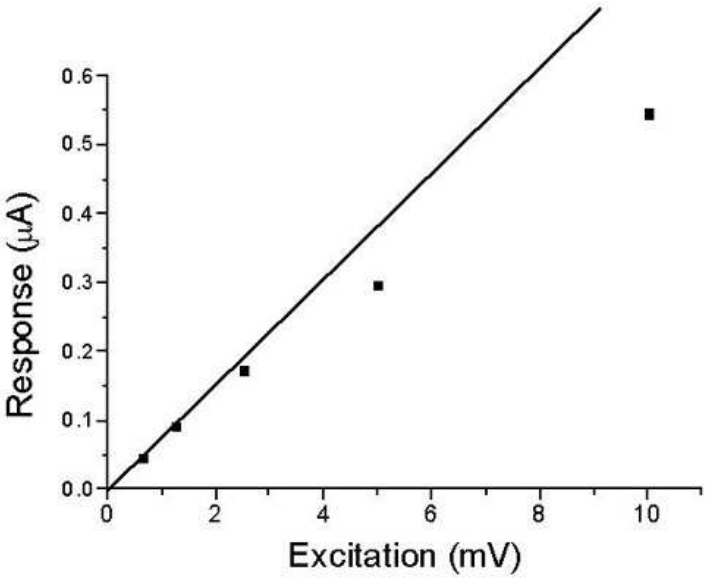

Figure 5.11: Excitation against response in vacuum (300 K)

in cold ^{4}He gas. It quickly became apparent that to obtain a useful Q, an unmodified fork was required.

Finally, in order to use the tuning fork successfully, a linear response, at the voltages to be used, was essential. The fork was tested in vacuum, air and, later, in ^{3}He-^{4}He mixture at 3 mK. The graphs of excitation voltage against response follow in figs. 5.11, 5.12 and 5.13.

The figure showing the response in the 6.2% mixture (fig. 5.13) also give a clear indication as to the amount of power dissipation which occurs. For an excitation of 100 mV the response is approximately 80 μA, giving a dissipation of $IV \sim 8$ μW. This is an unreasonable value for a dilution refrigerator to cope with at low temperatures, and from the fact that no substantial heat leaks were detected in the cell, it is assumed that this value is incorrect. Later measurements, using more simple measurement techniques (constant AC voltage excitation on one electrode, reading the frequency response of the current from the other and calculating power from IV) have produced values in the region of nW. It is believed that this more accurately reflects the true dissipation of the tuning fork.

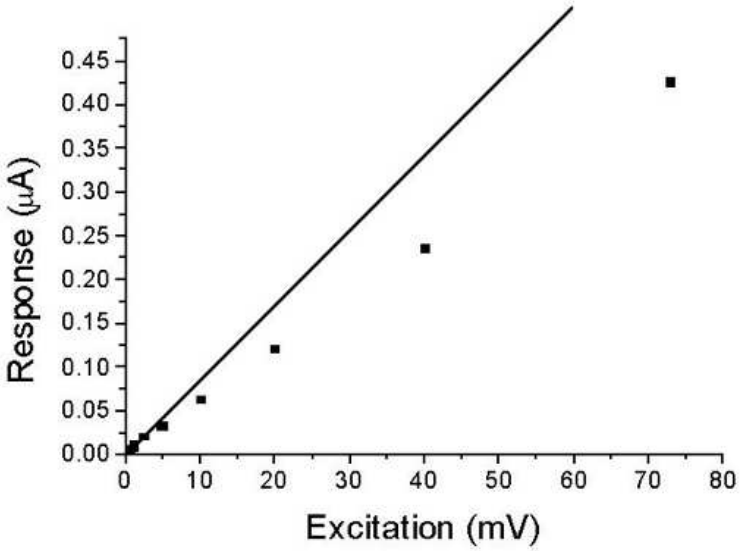

Figure 5.12: Excitation against response in air at S.T.P

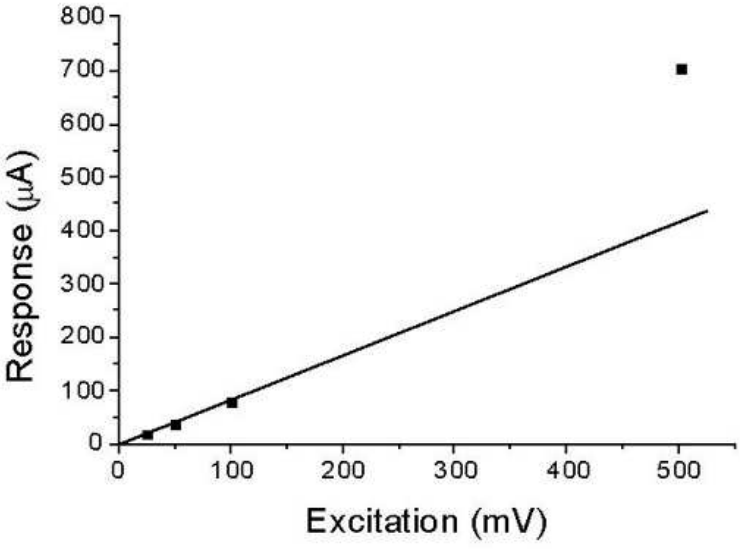

Figure 5.13: Excitation against response in 6.2% mixture

Attempts were also made to measure the linearity of the response in very dilute mixtures (0.1%). Tests at 5 mK showed an unexpected amount of heating which changed the local concentration of the mixture. At extremely low concentrations the effect of heating in changing the concentration is far more pronounced. Any heat gradient in the experimental cell will cause a supercurrent to flow to the higher temperature regions. The counterflow of normal fluid which results tends to sweep all the ^{3}He to the cold spots, hence distorting the sample concentration.

The details of the fork operation are covered in section 5.2.4, but it should be mentioned here that the excitation was maintained below 100 mV to ensure a linear response. Of particular interest in figure 5.13 is the deflection which *increases* non-linearly, in contrast to the cases for vacuum and air. Although the theory of tuning fork behaviour in Helium is very poorly understood, it may be that vortex creation has the effect of decreasing the viscous drag on the fork once the vortex creation threshold has been reached. It has been pointed out that, for all regimes, more points would have been useful in order to have a fuller picture of the limits of linearity. The author agrees with this analysis. The only mitigating factor in the lack of completeness was the urgent need to obtain data, after some 21 prior months with no results.

5.2.2 Fork Preparation

The tuning forks are factory-prepared in a sealed vacuum container. In this condition they have a Q of roughly 50000 and a resonant frequency of 32768 Hz. However, to use them as viscometers it is necessary to remove the vacuum can and allow the Helium free movement across the fork. The base of the fork, including the original electrical contacts ('legs'), is contained in cylindrical ceramic. This can be easily crushed using a pair of pliers, and the fork and legs simply fall out of the can. Ideally the legs need to be removed to solder leads of choice, in our case solderable copper, to the electrical contacts. When

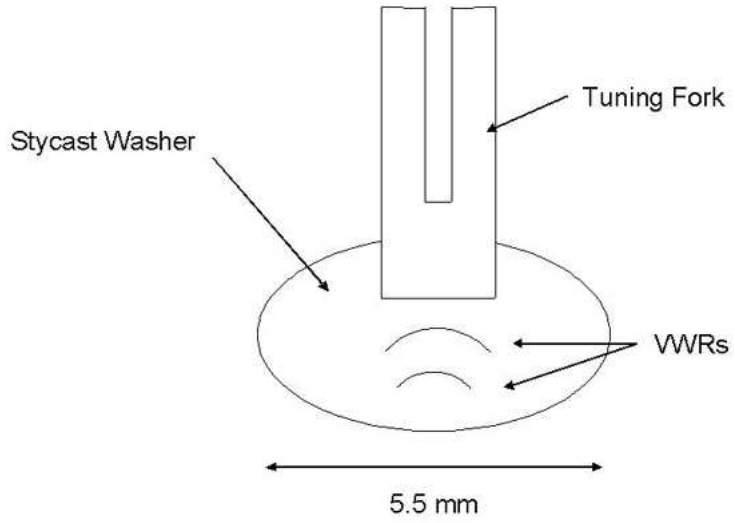

Figure 5.14: Simple diagram of the thermometry setup on the stycast washer

soldering new contacts, it is necessary to take considerable care, as the heat conductivity of Quartz is relatively high ($\sim$ $Wm^{-1}K^{-1}$) and the tendency is for one contact to fall off as another one is soldered on. Another difficulty was solder spreading beyond its original position on the fork causing electrical shorts of the resonance circuit.

To counter the first of these problems, the second wire was soldered to the fork whilst pressing down firmly on the already-soldered wire which lay on some paper sticking-tape. This tended to hold the first wire in place. The soldering iron was also modified. Wire was twisted around it and outwards to form a point which provided a more accurate tip and smaller heat transfer than the original tip of the soldering iron. Later attempts used a thin tipped soldering iron with a variable power input. The tuning fork was glued onto a "washer" made of stycast 1266 designed to fit inside a thermometry cell. To affix the fork onto the washer stycast 2850 was used. Care was taken to ensure at least 1 mm clearance between the two vibrating wires, the fork and the edges of the thermometry cell (fig. 5.14).

The vwr's were also glued into the washer using stycast 2850.

5.2.3 The Thermometry Cell

The original cell required screwing of a silver cap onto a silver reservoir, with stycast 2850 being applied to the threads to ensure a leak-tight seal. The feed-throughs were also made leak-tight by the application of stycast 2850, with the wires being pulled backwards and forwards through the holes to ensure maximum coverage. This design was extremely unforgiving of human error, in that if there was a problem with the thermometers inside the reservoir, or a connecting wire snapped close to the feed-through hole, very delicate work was required to fit a new cell, or the cap had to be physically unscrewed from the reservoir, a destructive process in itself. A diagram of the new upper-reservoir construction can be seen in fig. 5.15. The upper piece was made of titanium to increase the strength and decrease the heat capacity of the reservoir. A thread had to be machined on the inside of the silver to allow the titanium to be attached. This created a slight reduction in the diameter of the reservoir at the top end. The new cap was attached by bolts threaded through machined holes in a titanium cap. An indium 'o' ring allowed leak-proof seals to be established without the requirement of gluing with stycast 2850. This was a significant improvement, and allowed several modifications of the thermometry without complete destruction of the cell. The thermometry cell was dimensionally constrained by the size of the Helium reservoir which had an inner diameter of 8.1 mm at the top end.

Allowance was also required for wiring running along the outside of the thermometry cell. A stycast 1266 cylinder was machined into the appropriate dimensions (fig 5.16).

A 6mm outer diameter was selected to give sufficient clearance for wiring. The upper chamber is longer to accommodate the capacitor, the lower chamber contains the vibrating wires and the tuning fork, and has a generous

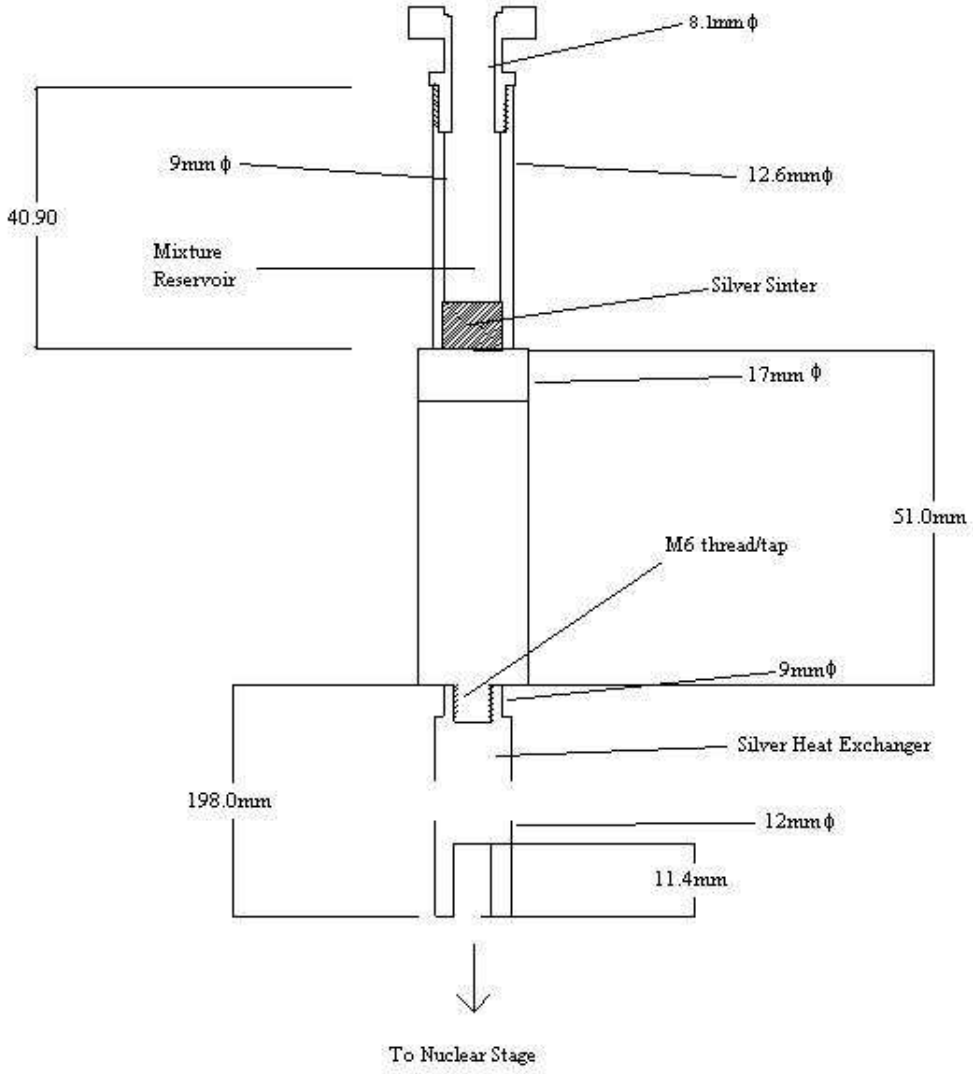

Figure 5.15: Diagram of new upper reservoir and heat exchanger

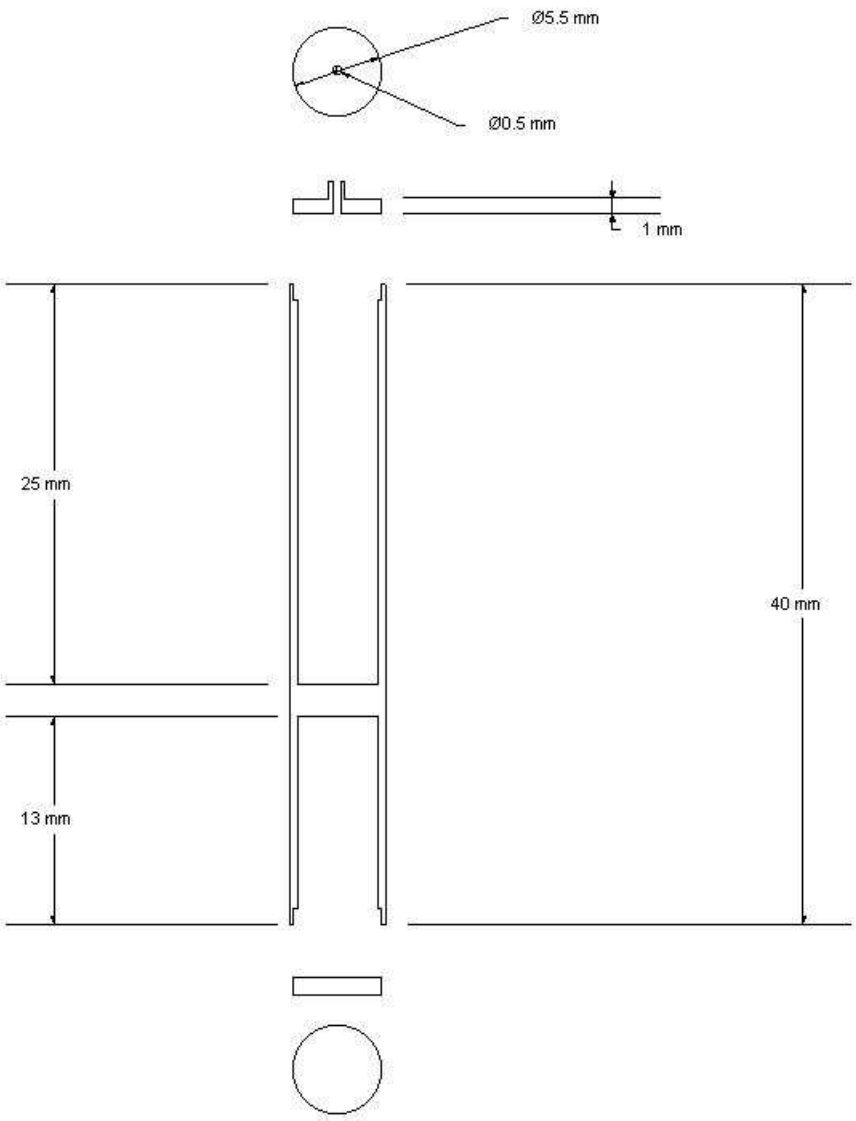

Figure 5.16: Diagram of the thermometry cell

clearance. Two washers were prepared, one which supported both vibrating wires and the tuning fork (fig. 5.14), the other, glued to the top of the capacitance chamber, which had a "fixing cylinder" which could be glued into the titanium cell cap (using GE varnish) to provide support for the whole thermometry cell. The "fixing cylinder" had a hole drilled through the centre of it to allow Helium to flow into the chamber via a connecting capillary through the cap. The wires were glued to the side of the stycast cylinder using GE varnish to prevent motion under high magnetic field. They were then passed through holes in the titanium cap which were sealed in place using stycast 2850 and were soldered to copper tracks on the outside of the reservoir.

5.2.4 Circuit Set-up

The tuning fork can be electrically excited through its electrodes or mechanically driven with an additional piezo element. The simplest form of operation is to use the existing electrodes by directly driving the tuning fork with a resonant voltage and measuring the induced current. To preserve linearity an excitation voltage of less than 100 mV was used (see fig. 5.13).

The equivalent circuit for the tuning fork is an LRC circuit in parallel with a static capacitance C_0, as seen in the diagram of the circuit set-up (fig. 5.17). When directly driven from a voltage source, the static capacitance yields both parallel and series resonances leading to a skewed lineshape. To eliminate this effect, C_0 was balanced with a capacitance bridge. Typical values of C_0 are of the order 20 pF. An operational amplifier circuit is used to convert the current to a voltage. A sample response in 6.2% ^{3}He-^{4}He is also shown in the circuit set-up diagram.

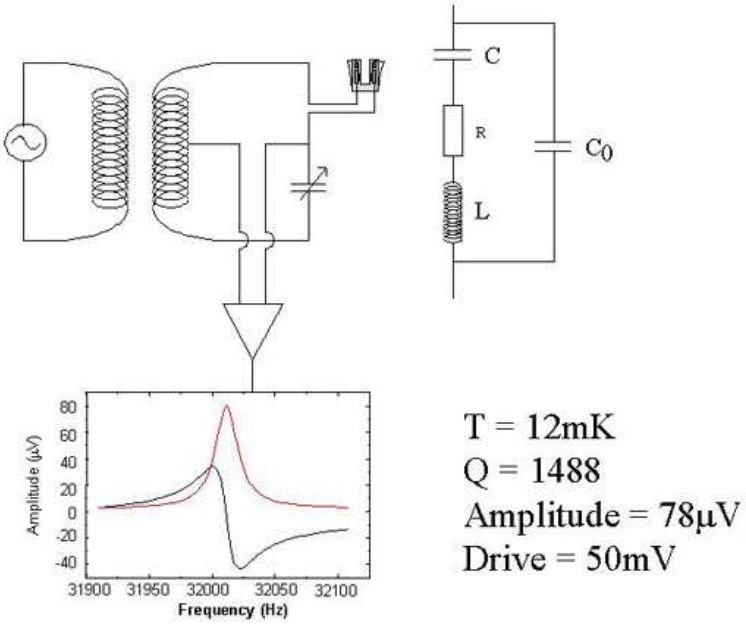

Figure 5.17: Schematic of the circuit setup and response

5.3 Results

5.3.1 6.2% Mixture

Quality Factor

The results of the tuning fork measurements require very careful analysis for several reasons. Foremost among these is that the thermometry below $\sim$ 20 mK is complicated, due to the vwr measurements failing to conform to the theory, and the lack of any reliable, reproducible means of thermometry, except for the temperature interpolated from the demagnetisation field, and the capacitor. Unfortunately, the capacitor requires calibration against another thermometer, and was not therefore useful in this situation.

Numerical simulations [65] show that the demagnetisation temperature should be matched with a reasonable degree of certainty down to 3 mK. Data were recorded below this point (the decreasing Q demonstrates that cooling occurs), but there is no knowledge about the exact temperature. Where appropriate, the Q and frequency shift have been plotted against the demagnetisation field, in order to demonstrate the unusual behaviour of the frequency

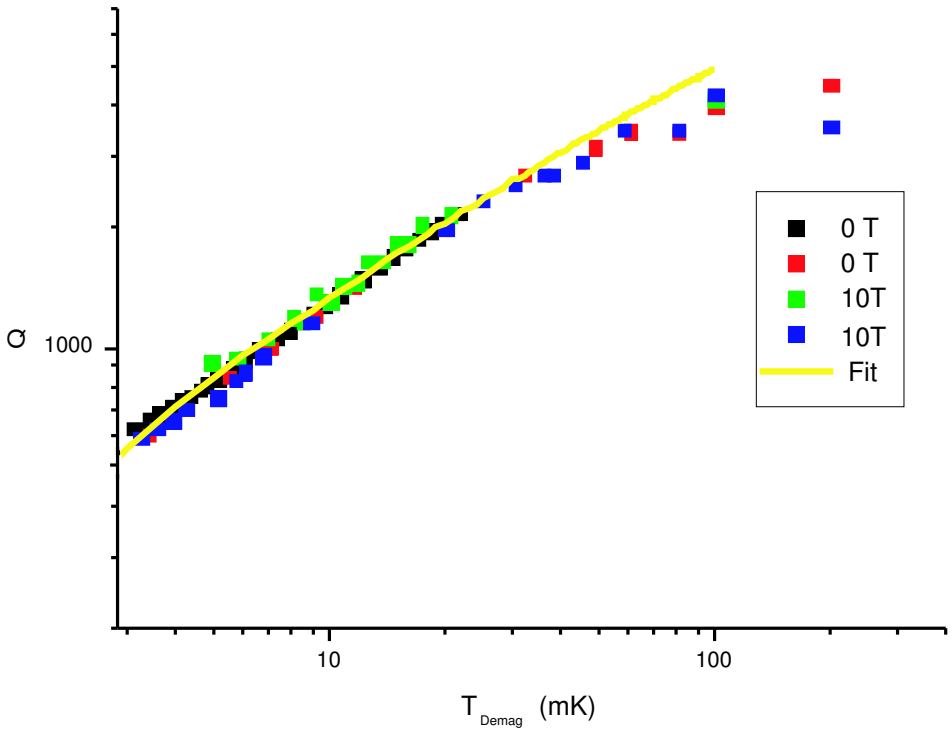

Figure 5.18: Graph showing tuning fork response of Q vs temperature, 6.2% mixture. The fit is calculated using eq. 5.11.

shift of the tuning fork in the region where there is the greatest uncertainty in temperature.

There are some important points to note from figure 5.18. The most striking point is that the application of a magnetic field has no effect upon the Q. This demonstrates the field-independence of the tuning fork. Secondly, it is clear that the data are extremely reproducible. The slope of the line between 3 and 30 mK is 0.669 with a correlation coefficient of 0.993 (see fig. 5.21). This means that the viscous damping follows a $T^{0.67}$ instead of a T power law, the first indication that mean free path effects are significant in this case. The errors in this fit mean that a $T^{2/3}$ power law can be established which simplifies the calibration (see section 5.3.1).

Third, the Q values lie within an easily-measurable range of several hundred at the lowest temperatures, rising by an order of magnitude up to 100 mK. Although there are no data above 200 mK the slope appears to be levelling off. This is probably due to the onset of acoustic damping, which is a greater

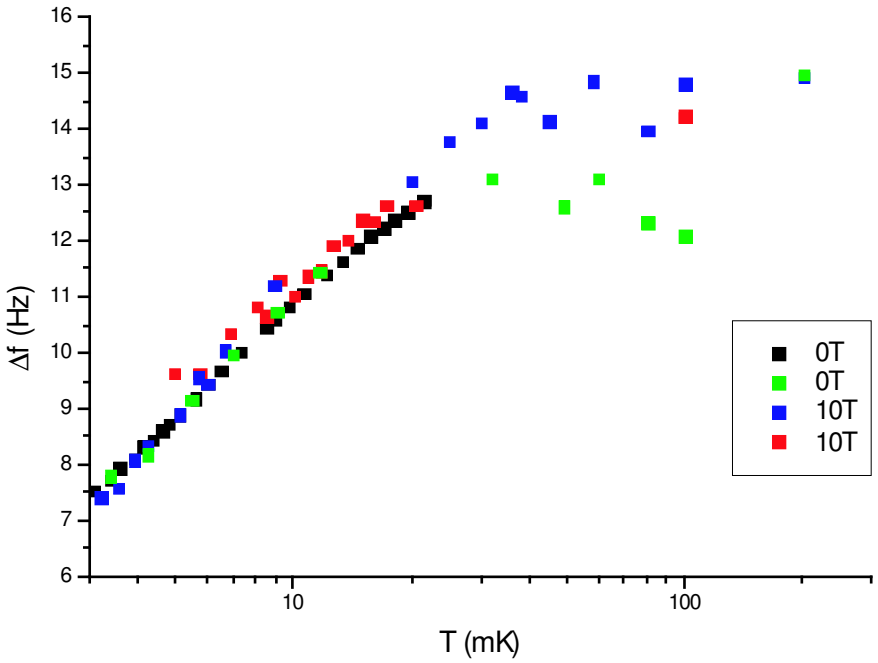

Figure 5.19: Graph showing tuning fork response, frequency vs temperature, 6.2% mixture ($f_0 = 32768$ Hz)

factor in tuning fork measurements than other viscometry techniques. Acoustic damping in general is stronger at high frequency, in particular where the oscillation of the resonator is small compared to its dimensions.

Frequency Shift

Figure 5.19 again demonstrates the reproducibility of the data at all fields. As in the previous graph attention should be drawn to several points. Firstly, the high-temperature (> 30 mK) points show a high degree of scatter thus limiting the useful range of the tuning fork to an upper limit of ~ 30 mK in concentrated mixture. Secondly, the frequency shift appears to decrease logarithmically with temperature. This is somewhat misleading as the frequency in fact *increases* as the temperature is further decreased. This can be seen in the final plot (fig. 5.20) where all the data are included. This shows that for decreasing Q (and hence temperature), the frequency shows a rapid increase. This behaviour is indicative of mean free path effects; this means that as the mean free path increases, so the onset of the ballistic regime is

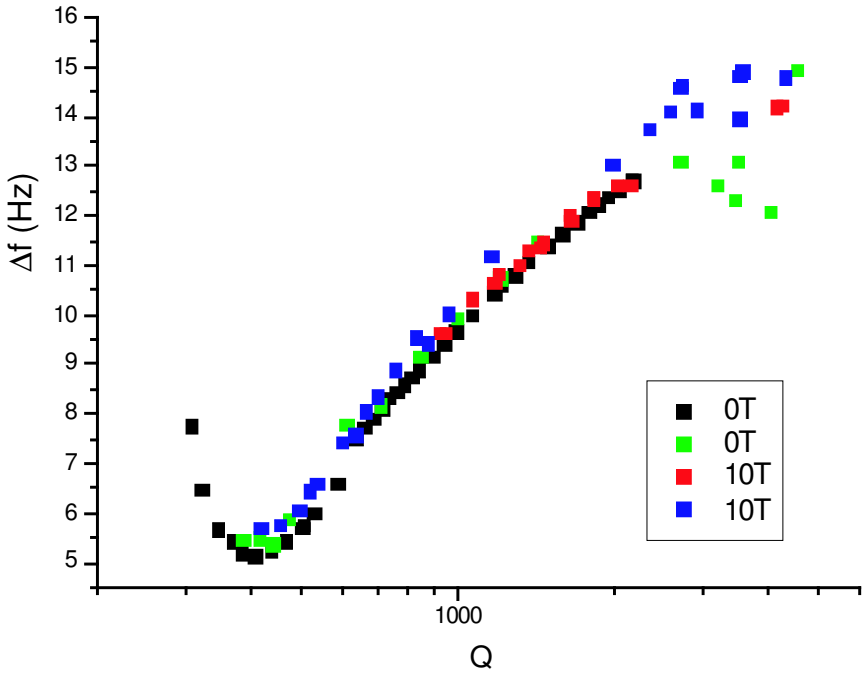

Figure 5.20: Graph showing tuning fork response of frequency against Q, 6.2% mixture ($f_0 = 32768$ Hz)

reached.

Mean free path effects are much more inconvenient in the concentrated mixture than pure ^{3}He; a qualitative analysis follows in section 5.3.4.

Calibration

The log fit through data between 3 and 30 mK (fig. 5.21) demonstrates a $T^{2/3}$ dependence of the quality factor. It is known that the viscosity η of the mixture varies as T^{-2}, and the Q can therefore be related to the temperature thus:

$$Q^3 = \frac{C}{\eta} \tag{5.10}$$

A phenomenological relationship between the Q and viscosity can be developed once the coefficient C in eq. 5.10 is determined from the slope. This can be seen in fig. 5.22. The correlation coefficient is close to unity. To create a working empirical formula, the usual formula of a straight line is

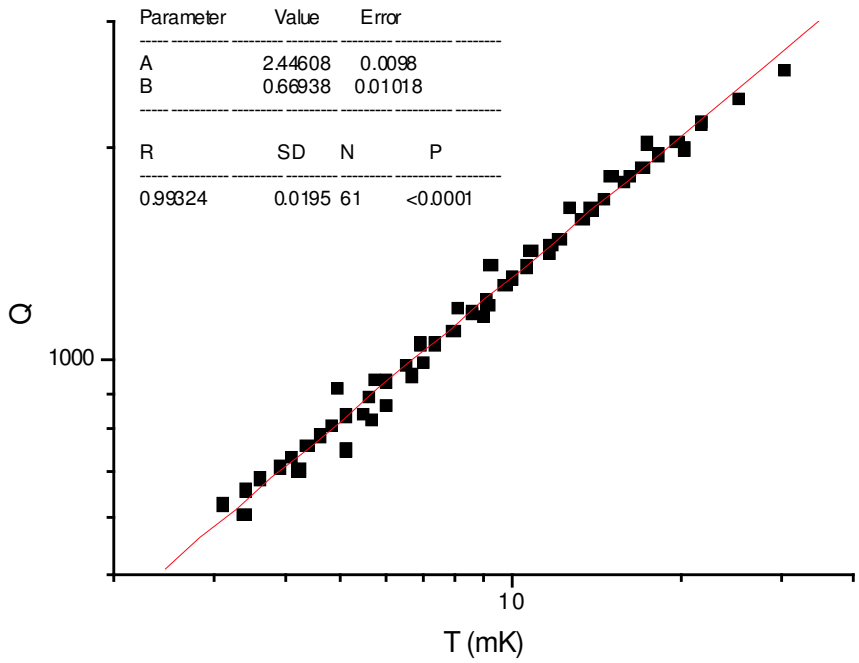

Figure 5.21: Log fit of Q vs T for all data (6.2% mixture), showing $T^{2/3}$ dependence

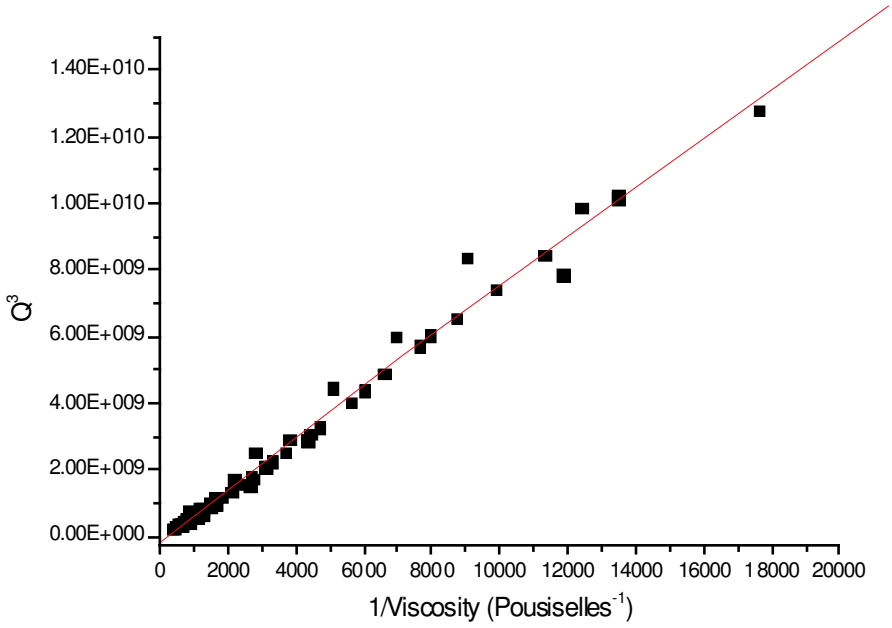

Figure 5.22: Dependence of Q^3 to the inverse of viscosity, 6.2% mixture

used to give

$$Q^3 = A + \frac{B}{\eta}$$

where A and B are the coefficients given by the fitting algorithm, and are shown in the figure. To produce a formula which relates the Q to the temperature, the viscosity must be related to the temperature. The values of η are obtained from reference [66]:

$$\eta T^2 = a + bT$$

where $a = 2.7 \times 10^{-8}$ PasK^2 and $b = 34 \times 10^{-8}$ PasK. $A = -5.80951 \times 10^7$ and $B = 735565.9$ Pas. The Q can then be related to the temperature:

$$A + \left[\frac{BT^2}{(a + bT)}\right] = Q^3 \tag{5.11}$$

with $A = -5.80951 \times 10^7$ and $B = 735565.9$ Pas. A simple calculation can provide a graph showing Q against T: this fit is included in figure 5.18.

5.3.2 Pure ^{3}He

Quality Factor

The data obtained for pure ^{3}He can be seen in fig. 5.23. The situation here is far more complicated. The Q values are lower than for the concentrated mixture, which is an expected result of the increased viscosity. What remains unclear is why one experimental run showed saturation of Q above 20 mK to ~ 200, whereas the other runs obtained a far higher Q at the same temperatures. Despite this anomalous behaviour, the saturation of Q above a certain limit is probably due to acoustic damping which becomes particularly significant in pure ^{3}He.

If the relevant graphs for 6.2% mixture and pure ^{3}He are compared, the reason for the much larger scatter of points in pure ^{3}He becomes apparent. The

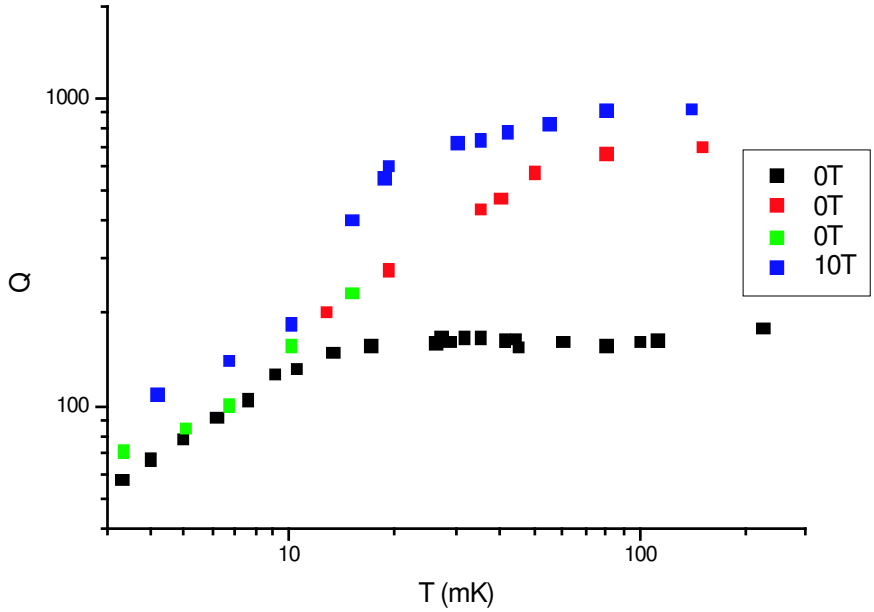

Figure 5.23: Relationship between Q and temperature, pure ^{3} He

Q values at low temperatures drops to as low as 50, which makes it exceedingly difficult to measure accurately. One indisputable point of reference, however, is the superfluid $\beta-$ phase transition, which occurs at 0.94 mK (at svp). This occurred at a demagnetisation field of 278 mT. The fact that the demagnetisation temperature was only regarded as reliable down to 3 mK, is clearly demonstrated by the fact that 278 mT corresponds to a 'demagnetisation' temperature of 0.53 mK. Using a crude linear interpolation between 3 and 0.94 mK, the temperature of any point between these poles may be determined from the value of the demagnetisation field. Unfortunately, only one experimental run pinpointed the 'precise' moment of transition using a chart recorder. For this reason, the relationship between the demagnetisation field and the quality factor is a more appropriate way of demonstrating the change in Q (fig. 5.24). As this necessarily neglects points above $\sim$ 20 mK, there is better agreement between the experimental runs.

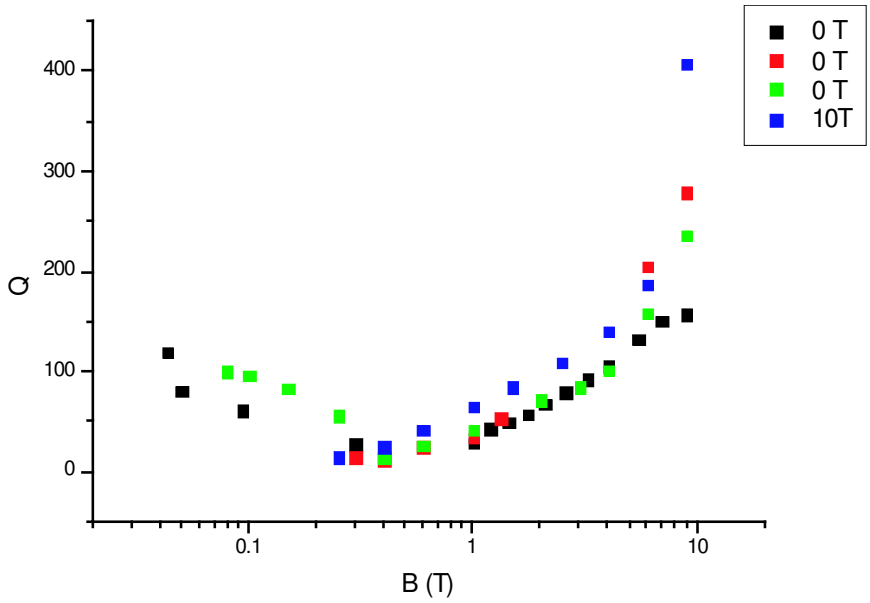

Figure 5.24: Graph showing Q against the demagnetisation field, B, pure ^{3}He

Frequency Shift

The frequency shift is a far more reproducible measure of the temperature than the Q for pure ^{3}He. This is demonstrated by the data in figure 5.25

A significant effect of crossing the superfluid transition is the increase of frequency as the temperature decreases. This is seen in figure 5.25, where the temperature is indicated by the demagnetisation field. It is assumed that the transition under high field is the A1-superfluid phase transition. However, there is little information currently available on the exact phase transition field profile, and exact identification requires further details on such a profile (see fig. 5.27).

5.3.3 0.1% Mixture

The data obtained from the dilute mixture are the least conclusive, and most puzzling, of the experiment. There are inconsistencies with data taken at the same temperature, but with a different capacitor excitation. This is almost certainly due to the 'heat flush' effect, whereby the local heat source causes ^{4}He atoms to flow to the source, displacing ^{3}He atoms, and causing a

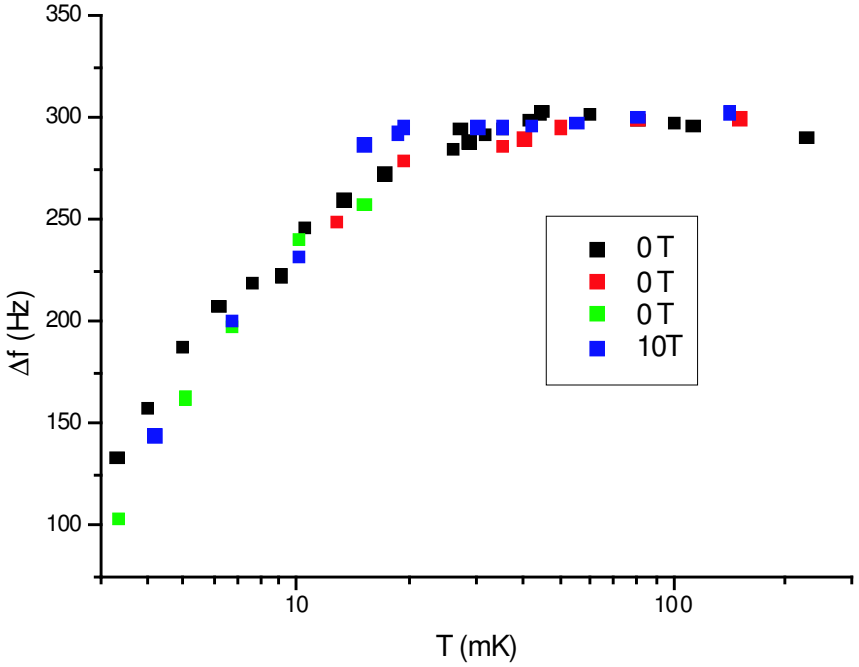

Figure 5.25: Graph showing frequency shift against temperature, pure ^{3} He ($f_0 =$ 32768 Hz)

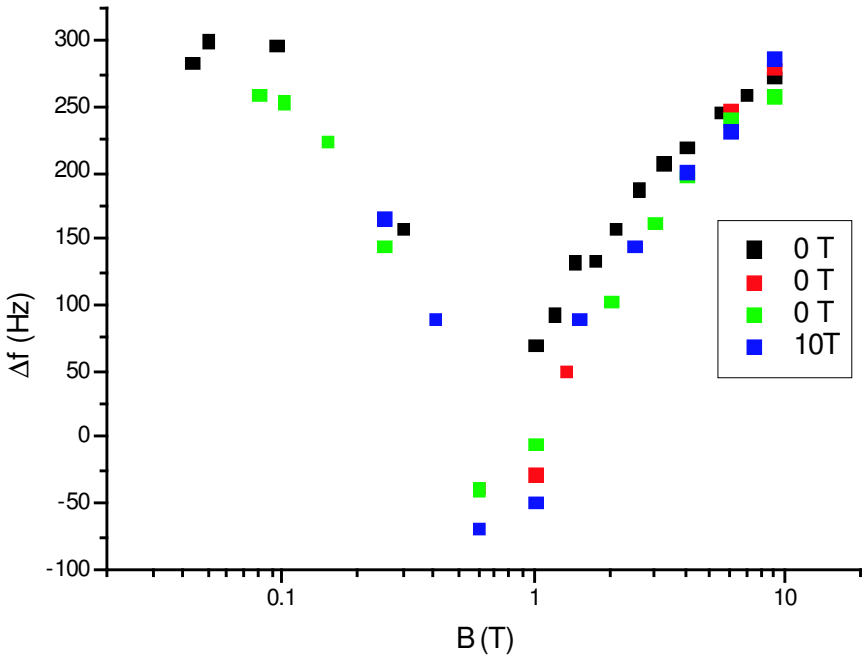

Figure 5.26: Frequency shift against demagnetisation field in pure ^{3} He. The superfluid A1 and B-phase transition can be clearly seen ($f_0 = 32768$ Hz)

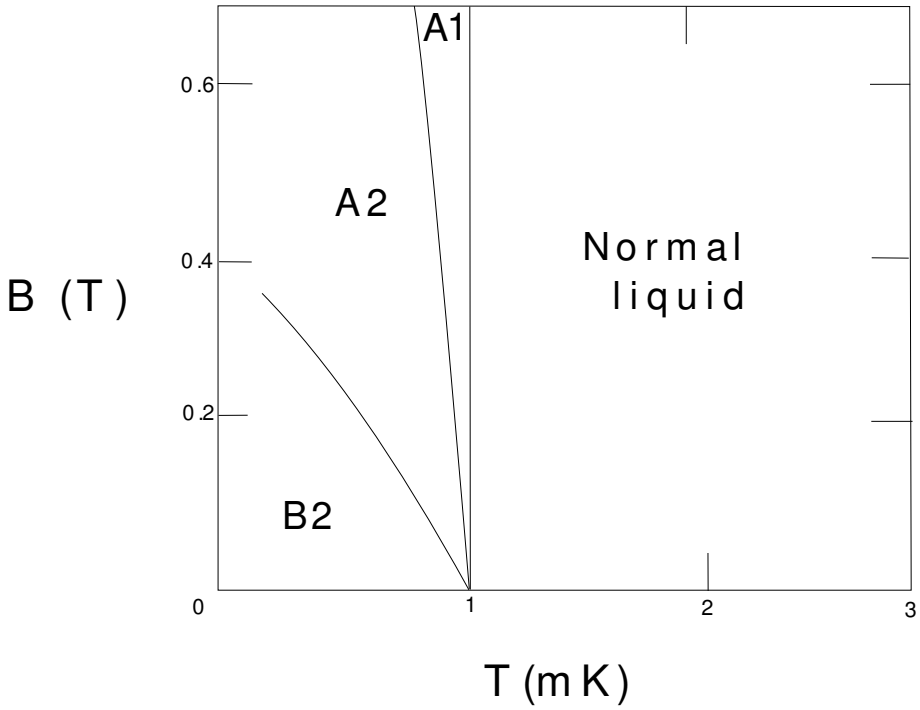

Figure 5.27: Phase diagram of superfluid ^{3}He.

change in the local concentration. An additional problem is that there were no reliable vwr measurements. This is because the main field was applied at the latter stages of the experiment, at the same time as the helium liquefier had to be shut down, necessitating a winding-up of the experiment. There are, nonetheless, some interesting points to be taken from the data. The following discussion concerns only the quality factor of the tuning fork, as the frequency shift was a comparatively insensitive indicator of temperature change.

The data are presented in figure 5.29, and the first point to note is that, for zero applied field, the Q peaks at $\sim$ 15 mK, and thereafter decreases with temperature. This behaviour is qualitatively consistent with the viscosity of a 0.1% mixture, as measured by Guenault *et al.* (see fig. 5.28)

Another major, and puzzling, point of interest was the difference in Q between the two data sets at different applied fields, 0 and 10 Tesla (fig. 5.29). It is very clear from this that the application of a strong magnetic field causes a dramatic drop in the quality factor. There are several possibilities for this.

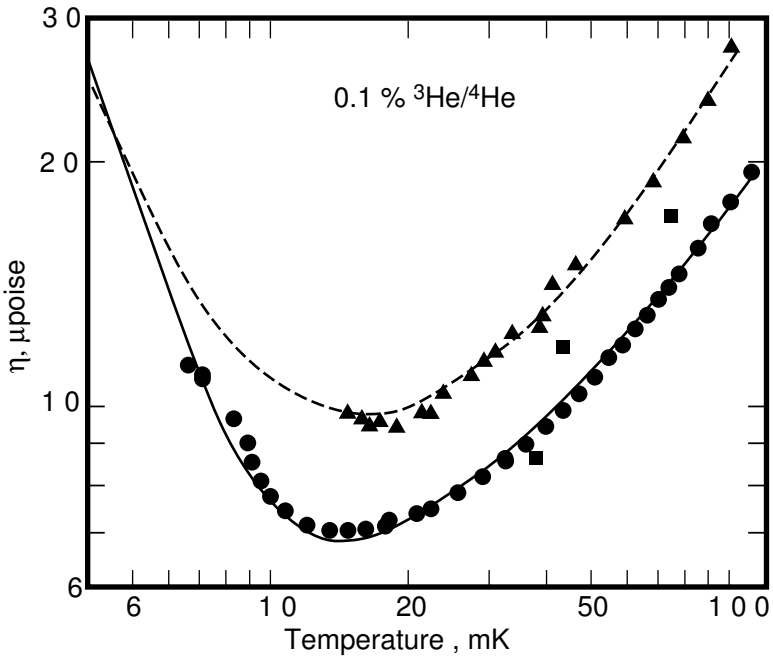

Figure 5.28: Viscosity of dilute mixtures (after Guenault *et al.* [67]). Circles are from ref. Guenault *et al.* [67] (vwr measurements), triangles from ref. [68] (second sound measurements), and squares from ref. [69] (capillary method)

With a vwr, the first inference is that eddy-current effects might be causing internal damping. This was not initially thought to be a factor, as the tuning fork is made of quartz. Additionally, the vacuum measurements at high field (fig. 5.30) indicate that eddy-current damping is negligible at the fields used for these experiments. The second idea is that the increased polarisation would cause an increase in the viscosity, as recorded by Candela et al [3]. The Fermi temperature of a 0.1% mixture is approximately 25 mK. This implies that there should be no departure of the behaviour of the tuning fork from that of the hydrodynamic system, until significantly below the temperatures of this experiment (ruling out significant mean-free-path effects). The polarisation of the mixture can be calculated directly [2], but an approximation [40] gives a polarisation P of 40% at 15 mK. This is determined by using a magnetic field size

$$b \equiv \hbar\gamma B/k_B T_F$$

giving $b = 2.78$ for the 10 T run. The change in viscosity due to this polari-

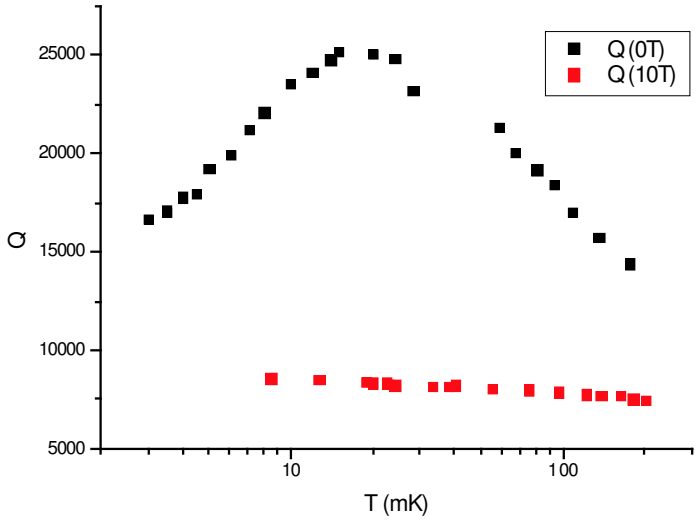

Figure 5.29: Graph showing the distinctive drop in Q on application of a 10 T field for dilute mixture

sation can be determined by a simple ratio

$$\frac{\eta(P)}{\eta(0)} = \frac{1 + \frac{3}{5}P^2}{1 - P^2}$$

in the hydrodynamic regime, giving a factor 1.3 for 15mK. The response of the tuning fork in the concentrated mixture has been given by equation 5.10, which would indicate a factor 2.2 between the two Q values. This would account for a large part of the difference between the two values, but further questions remain. From the shape of the curves, the Q of the 10 T sample increases with decreasing temperature, whilst that of the 0 T sample decreases. Thus as the polarisation, and hence viscosity ratio, increases as $T \rightarrow 0$, so the difference between the two data sets diminishes, contrary to initial expectations. Another attempt to justify the apparent contradiction between the two data sets at different fields is to consider the effective mass. This drops with increasing polarisation, and it is reasonable to assume that its value is of the order 1.5 m, rather than the 2.3 m considered for the unpolarised situation. Unfortunately, this exacerbates the situation: a lower effective mass would appear to mean an increasing Q, rather than the results observed. Finally, it may be that the high applied field causes migration of ^{3}He atoms from the heat exchanger to the experimental cell. This would seem

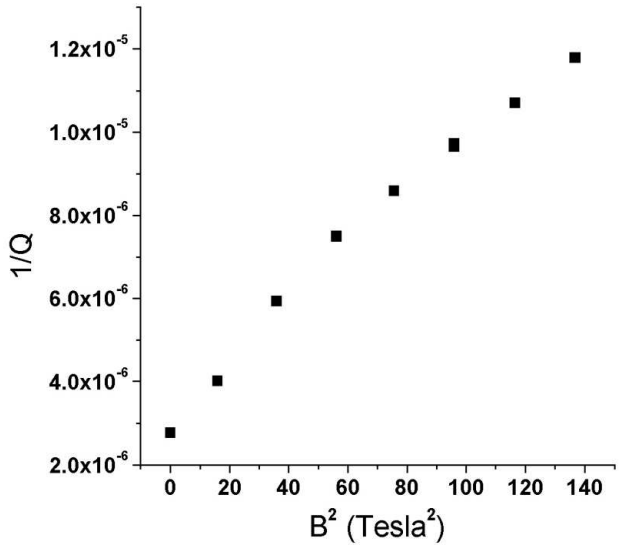

Figure 5.30: 1/Q against B^2, vacuum at 4.2 K

to be a fairly likely scenario, although it is uncertain why the change in Q is so pronounced at the high-temperature region (fig. 5.29) where polarisation is likely to be insignificant. Measurements in dilute mixtures are difficult in general, as there is poor thermal contact between the refrigerant and the ^{3}He atoms, and also because "heat-flush" effects caused by slight thermal gradients are particularly severe. There remain more questions than answers for the case of the dilute mixture; hopefully future experiments will be able to produce more emphatic results.

Further measurements were carried out in vacuum at 4.2 K in order to ascertain the relationship between the magnetic field and the quality factor in vacuum. The results of these measurements are given in figure 5.30. The data confirm an extremely strong field dependence of the fork response, which can only be put down to some unspecified field-dependent effect. A further set of measurements was taken at 50 mK, with the results plotted in figure 5.31. These data reinforce the fact that the Q-factor damping is field-dependent.

Much time was spent trying to determine the reason for the drop in Q under application of a strong field. In fact, the real reason is very obvious, and

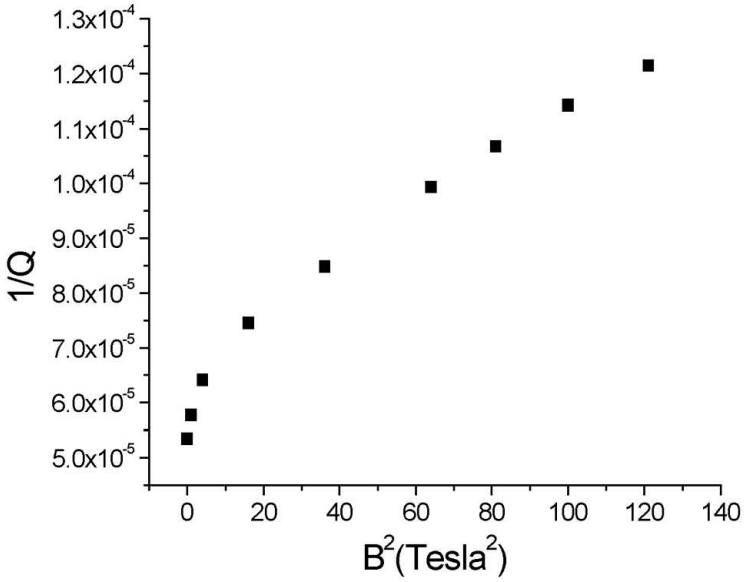

Figure 5.31: 1/Q against B^2, 50 mK in dilute (0.1%) mixture

was only realised after a break of several months, when the data could again be considered in a fresh light. From fig. 5.31 it can be seen that the "eddy current Q" (strictly speaking, the field-dependent effect) of the tuning fork at 50 mK is approximately 9000. This alone would account for the levelling off of the curve which is seen in fig. 5.32. To summarise:

1. The field dependence of the tuning fork is insignificant compared with acoustic losses or viscous damping for both pure ^{3}He and 6.2% ^{3}He-^{4} He mixtures (of course this statement is a reflection of the fact that the highest static fields "commonly" available at this moment in time are of the order 10-15 Tesla). The field dependence for the dilute mixture is significant. At present this is thought to be due to a combination of polarisation effects, and due to magnetic pumping which causes an increase in concentration at the high field region.

2. The fork in the ^{3}He and 6.2% mixture share a common Q response as $T \rightarrow 0$, i.e. relatively unchanged until a certain threshold is reached, and thereafter a decrease in temperature results in a decrease in Q, as expected

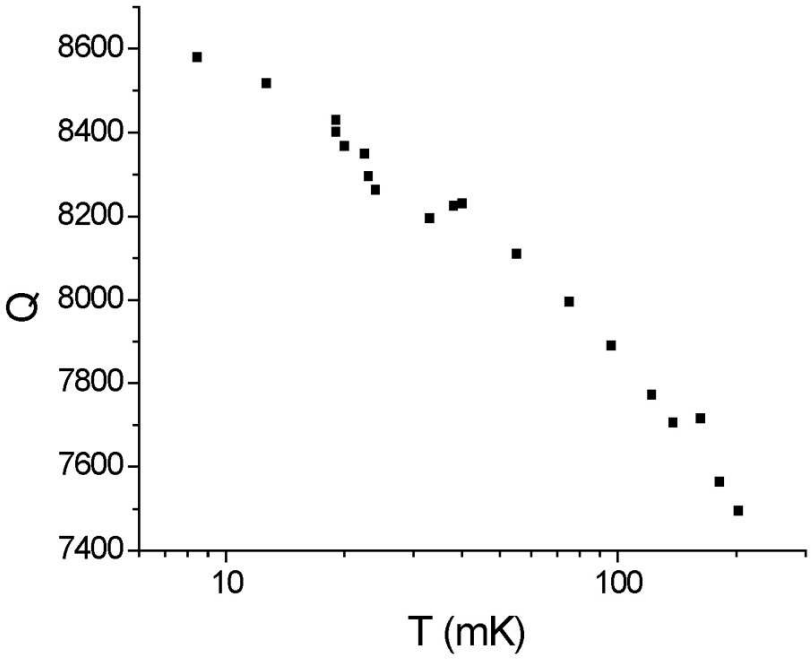

Figure 5.32: Q against temperature, dilute mixture at 10 T

for a Fermi liquid. This is probably due to acoustic damping being the primary damping mechanism until viscous damping takes over. The acoustic damping for the dilute mixture is far less due to the small number density of ^{3}He atoms. This explains the high Q values recorded for the dilute mixture (a maximum of $\sim$ 25000, compared with $\sim$ 4000 and $\sim$ 1000 for the 6.2% mixture and pure ^{3}He respectively).

5.3.4 Analysis

If the tuning fork is to be used as a thermometer without calibration, a working model which calculates the values of k and k', and fits to the experimental data, is required. Although the analysis for a single oscillating beam has been made [64], the fork was not usable with a single tine. The approximation used is therefore the theory for an oscillating cylinder (section 5.1.6). The values for k and k', obtained from the theory, are plotted with the experimental points, to see how closely the approximation works. For

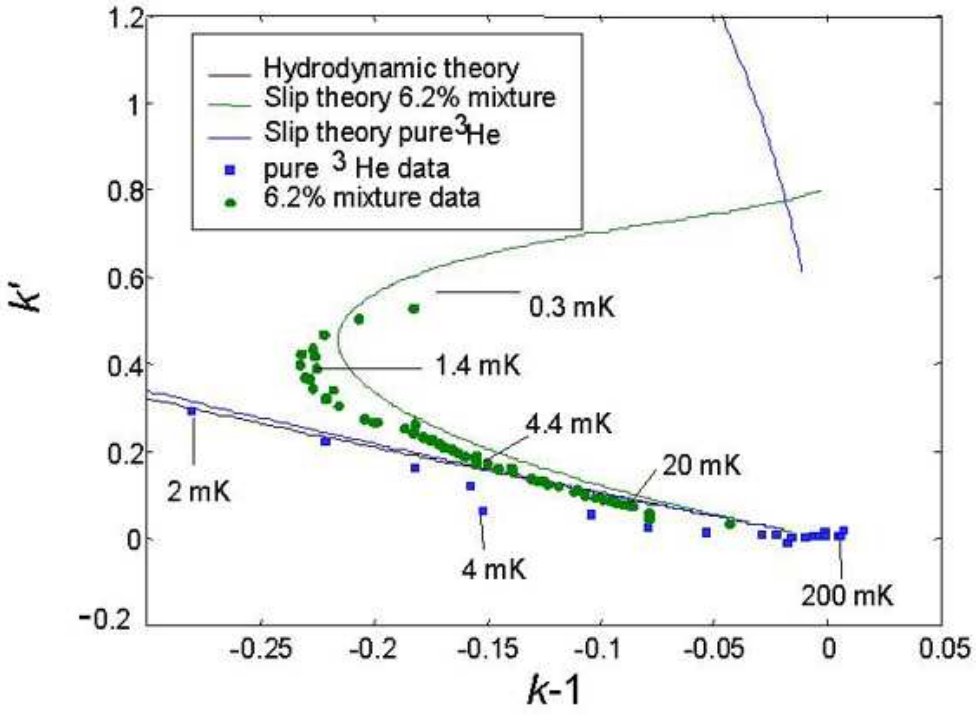

Figure 5.33: Values of k and k', obtained experimentally and the theoretical curves. k is proportional to the frequency width due to the viscous damping: k' gives a measurement of the frequency shift δf_1 calculated from $\delta f_1 = f_0^{vac} - f_0$, where f_0 is the resonant frequency.

a behaviour of the fork which exactly followed the model of a cylinder, the experimental and theoretical points should overlap. The plot can be seen in fig. 5.33. At such low temperatures, the transition from the hydrodynamic regime to ballistic regime begins to be breached. The values of k and k' therefore need to be modified by using the 'slip corrections' [70]. The existence of a 'slip' in aerodynamics had been noted since the 19th century [71]. Results of experiments performed on rarified gases were explicable on assumption that the gas 'slipped' at a wall, or, more precisely, that the tangential flow velocity relative to the wall extrapolates linearly to zero at a distance ζ (the slip length) behind the wall.

^{3}He quasiparticles can be thought of as a rarified gas of thermal excitations which obey quantum statistics, and the theory of slip correction can be correctly applied to the case of viscometers in ^{3}He and its mixtures. In the hydrodynamic regime the viscometer is damped normally by the fluid in

which it is immersed. In the ballistic regime the mean free path becomes comparable to the size of the viscometer, and the quasiparticles no longer impinge on the viscometer, proportional to their number density. Although there is still considerable discussion on the subject, the slip corrections described in equations 5.12 and 5.13 represent the best model of the behaviour in the ballistic regime.

$$k(m) = 1 + \frac{k_0(m) - 1}{[1 + m^2\beta k_0'(m)]^2 + m^4\beta^2[k_0(m) - 1]^2} \tag{5.12}$$

$$k'(m) = \frac{k_0'(m) + m^2\beta([k_0(m) - 1]^2 + [k_0'(m)]^2)}{[1 + m^2\beta k_0'(m)]^2 + m^4\beta^2[k_0(m) - 1]^2} \tag{5.13}$$

where $\beta = \xi\ (\xi + a)$, with ξ the slip length and a the wire radius. The slip corrections have also been plotted in figure 5.33. It can be seen that the theory and experiment have a very close correlation for the pure ^{3}He. This is not the case for the concentrated mixture, however, which can be said to follow the theoretical curve in a qualitative fashion (thus indicating that the slip effect is significant) but not being a good quantitative match.

The conclusion of the analysis is that the fork can be used in pure ^{3}He modelling it using the theory of an oscillating cylinder; the Q obtained in the critical region (< 10 mK) however does not lend itself to being a useful thermometer. Conversely, the same theory could not be used for the concentrated mixture, which is unfortunate as the experimental data recorded would indicate its usefulness in this regime. The relative lack of experimental data for the very dilute mixture indicates that further work should be carried out in order to understand fully the fork behaviour for this regime. The author would also suggest that there is the potential to use the tuning fork as a viscometer in the superfluid regime; obviously this will require more specialised facilities to prove than are currently available at Nottingham.

Chapter 6

Discussion

The main part of the work carried out for this thesis was the NMR experiments on ^{3}He and its mixtures with ^{4}He. These experiments were specifically targeted at determining the value of the anisotropy temperature. An important by-product of these experiments, was the subsequent work performed on restricted-diffusion effects, which enabled precise analysis of the 6.2% mixture NMR data. This is significant, not just in the scale of the change in value for T_a for the experiments at Nottingham, but in providing an independent benchmark to determine the effects, if any, of restricted diffusion for past and future experiments. This benchmark is the magnitude of the dimensionless parameter, b_L, which can be calculated in a straightforward way by any group performing experiments on this topic. Also to be considered, however, are those effects which have been *excluded* from this modified analysis.

The first of these are any non-linearities in the system, which are assumed to be negligible for tipping angles of the order 20^0. The second, and most important, is the demagnetising field. As has been previously mentioned, there is no instantaneous transition between a regime of strong interactions, and that where they can be completely neglected. Despite this, there can be a high degree of confidence that the effects for the 6.2% mixture are dwarfed by those due to the cell geometry. The same can certainly not

be said to be true for the case of pure ^{3}He. This case requires theoretical work in creating a model to include the effects of the demagnetising field. A possible additional benefit of such work would be to confirm the assumption that the effect in a concentrated mixture is negligible. Another piece of the puzzle which would greatly benefit from further theoretical work, would be the extension of Fomin's theory to finite temperatures. This would either support or rebut Meyerovich's contention that there is an intrinsic damping of spin diffusion as $T \rightarrow 0$. Whilst there is plenty of scope for work by theoreticians, the experimental side also has a rich variety of possibilities to further the knowledge base in this area. Certainly, increasing the magnetic field at which the experiments take place is a useful step, as the value of T_a is expected to scale with the field. The temperature of the experiments also plays a role in enhancing the information retrieved from experiments. As the technology of superconducting magnets improves, and the design of dilution refrigerators and nuclear demagnetisation cryostats is enhanced, so the improvement of greater B/T ratio should automatically follow. Yet, even beyond this, there are further avenues of investigation. The use of aerogel is one such avenue. The inhomogeneity introduced by the gel occurs on length scales which are smaller than the coherence length of the superfluid coherence length [72], thus the gel appears to the ^{3}He as a dirty impurity. In any such ^{3}He system it may be that any modes present are distorted by the presence of the aerogel. In pure ^{3}He, large NMR signals can be picked up from the solid-like layer of ^{3}He which coats the walls. The dimensions of the aerogel structure also affect the response of the system; for example, the ^{4}He in a mixture will preferentially fill smaller pores in aerogel due to its larger Van der Waals attraction. Work currently underway at Nottingham and elsewhere [73] investigates the spin dynamics of a system made up of a large reservoir connected to an NMR cell containing aerogel. Results from these experiments will help to complete the models of behaviour of spin-polarised

Fermi systems under different conditions.

One significant failure experimentally, was to create a leak-proof spherical cell which could be used to produce data which would be simpler to analyse. Several factors hampered attempts in this direction, not least of which is the unconventional design of the demagnetisation stage, which requires very careful handling to ensure the survival of the quartz cell. Although several different approaches were used, the cell never survived the insertion process unscathed. Despite this, salutary lessons were learned. Foremost amongst these, which should be quickly learned by people unfamiliar with the process of constructing a leak-proof seal, is that it is virtually impossible to repair a suspected leak on stycast simply by adding further layers of the same material. In the long run, it is far less time consuming to remove all the old stycast, and to clean it thoroughly, before beginning again. With the ample time provided by reconstructing the cell several times, a new resonator was constructed, which was also used to try to protect the cell during insertion. Eventually the whole cell design was altered in order to make the turn-around time between attempts much quicker. This new design has since been adopted as the template for future experiments on the same cryostat.

The second major piece of work was the construction and testing of a tuning fork viscometer. This development took many months to complete, with many different excitation methods (one-tine removed, free-standing; one tine removed, glued to rigid body; whole tuning fork, glued to rigid body; whole tuning fork, free-standing) attempted. The testing for each of these methods included immersion in different gases and liquids, in order to approximate the viscosity changes which could be expected at low temperatures. What was not anticipated at the start of the trial, was how well the tuning fork would perform. In concentrated mixture, it is a tool which produces extremely reproducible results, and has a useful range of an order of magnitude upwards from ~ 3 mK. In some respects, this does not completely solve the thermom-

etry problems we encounter at very low temperatures. It still needs to be calibrated against another thermometer, which, unfortunately, due to poor vwr response, was not available during the experimental run. There is no reason why, once calibrated, it may not prove to be useful for each run in the same mixture, much in the same way as for a vwr.

In pure ^{3}He the fork has been used to detect the superfluid transition (something that has not previously been possible with vwr's in the apparatus at Nottingham), although, due to its low Q, there is a much greater uncertainty in the values of Q and frequency shift recorded. In most apparatus which can perform at these temperatures, vwr's are currently the instrument of choice. Very few of these systems use a field as high as 11 T, so it may be that for such conditions the tuning fork may deserve more attention. It may be that at ultra-high fields the quality factor will be completely spoilt by eddy current damping (estimates based on the vacuum measurements made herein suggest that fields of order several hundred Tesla would be required to cause this magnitude of eddy current damping). Also, at ultra-low (μK) temperatures, there may be no damping at all from ballistic quasiparticles, and its use will be somewhat limited as a thermometer (though there is the further possibility of using it to generate vortices). Despite these caveats, there is the possibility that it could be used below the superfluid transition very successfully, and this work has aroused some considerable interest from other researchers [74], which will hopefully yield the focussed testing that such an instrument merits.

Bibliography

[1] J R Owers-Bradley, *Reports on Progress in Physics*, **60**, 1174 (1997)

[2] J R Owers-Bradley, R M Bowley and P C Main, *J. Low Temp. Phys.*, **60**, 243 (1985)

[3] D Candela, L J Wei, D R McAllaster and W J Mullin, *Phys. Rev. Lett.*, **67**, 330 (1991)

[4] D Candela, N Masuhara, D S Sherrill and D O Edwards, *J. Low Temp. Phys.*, **63**, 369 (1986)

[5] V P Silin, *J. Exptl. Theoret. Phys.*, **6**, 945 (1958)

[6] P M Platzman and P A Wolff, *Phys. Rev. Lett.*, **18**, 280 (1967)

[7] A J Leggett and M J Rice, *Phys. Rev. Lett.,* **20**, 586 (1968)

[8] A J Leggett, *J. Phys. C*, **3**, 448 (1970)

[9] D Einzel, G Eska, Y Hirayoshi, T Kopp and P Wolfle, *Phys. Rev. Lett.*, **53**, 2312 (1984)

[10] G Nunes, Jr., C Jin, A M Putnam, D L Hawthorne and D M Lee, *Physica B*, **165**, 721 (1990)

[11] A E Meyerovich, *Phys. Lett.*, **107A**, 177 (1985)

[12] A E Meyerovich and K A Musaelian, *J. Low Temp. Phys.*, **94**, 249 (1994); *J. Low Temp. Phys.*, **95**, 789 (1994); *Phys. Rev. Lett.*, **72**, 1710 (1994)

[13] I A Fomin, *J.E.T.P. Lett.*, **65**, 749 (1997)

[14] O Buu, D Clubb, R Nyman, J R Owers-Bradley and R König, *J. Low Temp. Phys.*, **128**, 123 (2002)

[15] L R Corruccini, D D Osheroff, D M Lee and R C Richardson, *Phys. Rev. Lett.*, **21**, 650 (1971)

[16] L R Corruccini, D D Osheroff, D M Lee and R C Richardson, *J. Low Temp. Phys.*, **8**, 229 (1972)

[17] G A Vermeulen and A Roni, *Phys. Rev. Lett.*, **86**, 248 (2001)

[18] J D Feder, Ph.D. Thesis, Ohio State University (1979), Unpublished; H N Scholz, Ph.D. Thesis, Ohio State University (1981), Unpublished; N Masuhara, D Candela, R Combescot, D O Edwards, R F Hoyt, H N Scholz and D S Sherrill, in Proceedings of the 17th International Conference on Low Temperature Physics LT17, U Eckern, A Schmid, W Weber and H Wuhl, eds. (North-Holland, Amsterdam, 1984), Part I, p. 555.

[19] N Masuhara, D Candela, D O Edwards, R F Hoyt, H N Scholz, D S Sherrill and R Combescot, *Phys. Rev. Lett.*, **53**, 1168 (1984)

[20] J R Owers-Bradley, H Chocholacs, R M Mueller, Ch. Buchal, M Kubota and F Pobell, *Phys. Rev. Lett.*, **51**, 2120 (1983)

[21] G Nunes, Jr., C Jin, D L Hawthorne, A M Putnam and D M Lee, *Phys. Rev. B,* **46**, 9082 (1992)

[22] W J Mullin and J W Jeon, *Phys. Rev. Lett.*, **62**, 2691 (1989); *J. Low Temp. Phys.*, **112**, 265 (1998)

[23] L-J Wei, N Kalechofsky and D Candela, *Phys. Rev. Lett.*, **71**, 879 (1993)

[24] J H Ager, A Child, R Konig, J R Owers-Bradley and R M Bowley, *J. Low Temp. Phys.*, **99**, 683 (1995)

[25] J R Owers-Bradley, R M Bowley, O Buu, D Clubb, *J. Low Temp. Phys.*, **121**, 779 (2000)

[26] D Candela, H Akimoto, R M Bowley, O Buu, D Clubb and J R Owers-Bradley, *J. Low Temp. Phys.,* **121**, 767 (2000)

[27] H Akimoto, J S Xia, E D Adams, D Candela, W J Mullin and N S Sullivan, *J. Low Temp. Phys.*, **126**, 109 (2002)

[28] D Candela, D R McAllaster, L-J Wei and N Kalechofsy, *Physica B.*, **197**, 406 (1994)

[29] R K Harris, Nuclear Magnetic Resonance Spectroscopy, Longman Scientific & Technical (1983)

[30] F Bloch, *Phys. Rev.*, **70**, 460 (1946)

[31] C Lhuillier and F Laloë, *J. Phys. (Paris),* **43**, 197, 225 (1982)

[32] E R Dobbs, Helium Three, Oxford Science Publications (2000)

[33] B Castaing and P Nozières, *J. Physique*, **40**, 257 (1979)

[34] A Roni and G Vermeulen, *Physica B*, **280**, 87 (2000)

[35] R L Garwin and H A Reich, *Phys. Rev.*, **115**, 1478 (1959)

[36] C Ebner, *Phys. Rev.*, **156**, 156 (1967)

[37] D Hone, *Phys Rev.*, **121**, 669 (1961)

[38] W R Abel, A C Anderson, W C Black and J C Wheatley, *Physics* **1**, 337 (1965)

[39] O Buu, R Nyman, R M Bowley and J R Owers-Bradley, *Phys. Rev. B*, **65**, 1345 (2002)

[40] W J Mullin and K Miyake, *J. Low Temp. Phys.*, **53**, 313 (1983)

[41] W J Mullin and J W Jeon, *J. Low Temp. Phys.*, **88**, 433 (1992)

[42] G Vermeulen, Private correspondence

[43] P L Krotkov, V P Mineev, G A Vermeulen, *Phys Rev B*, **65**, 054301 (2002)

[44] H C Torrey, *Phys. Rev.*, **104**, 563 (1956)

[45] L D Landau, *Zh. Eksp. Teor. Fiz.* **30**, 1058 (1956), and **33**, 59 (1957) [*Sov. Phys. JETP,* **3**, 920 (1957), and **5**, 101 (1957)]

[46] E L Hahn, *Phys. Rev.* **80**, 580 (1954)

[47] A S van Steenbergen, S A J Wiegers, P E Wolf, J A A J Perenboom and J C Maan, *Phys. Rev. B*, **58**, 925 (1998)

[48] P C Hammel and R C Richardson, *Phys. Rev. Lett.*, **52**, 1441 (1984)

[49] E N Smith, D J Bishop, J E Berthold and J D Reppy, *J. Phys. (Paris)*, Colloq **39**, C6-342 (1978)

[50] D F Brewer, D J Creswell, T Goto, M G Richards, J Rolt and A L Thomson, in *Monolayer and Submonolayer Helium Films*, ed. J G Daunt and E Lerner (Plenum, New Yorkm 1973)

[51] T Perry, K De Conde, J A Sauls and D L Stein,*Phys. Rev. Lett.,* **48**, 1831 (1982)

[52] F Pobell, Matter and Methods at Low Temperature, Springer-Verlag, 265 (1996)

[53] Th Wagner, S Götz and G Eska, *Cryogenics*, **34**, 655 (1994)

[54] H Akimoto and D Candela, *J. Low Temp. Phys.*, **121**, 791 (2000)

[55] J. Naish, Ph.D. Thesis, Nottingham University (1997)

[56] R.J. Rogge and W.J. Mullin, *J. Low Temp Phys.*, **102**, 461 (1996)

[57] H A Kierstad, *J. Low Temp. Phys.*, **24**, 497, (1976)

[58] O Buu, R Nyman, D Clubb, J R Owers-Bradley and R König, *J. Low Temp. Phys.*, **128**, 143 (2002)

[59] D Candela and D R McAllaster, *Cryogenics*, **31**, 94 (1990)

[60] C P Lusher, J Li, V A Maidanov, M E Digby, H Dyball, A Casey, J Nyéki, V V Dmitriev, B P Cowan and J Saunders, *Meas. Sci. and Technol.*, **12**, 1 (2001)

[61] W. Ruesink, J.P. Harrison and A. Sachrajda, *J. Low Temp. Phys.*, **70**, 393 (1988)

[62] J Rychen, T Ihn, P Studerus, A Hermann, K Ensslin, H J Hug, P J A van Schendel and H J Guntherodt, *Rev. Sci. Instr.*, **71**, 1695 (2000)

[63] F J Giessibl, *Appl. Phys. Lett.*, **73**, 3956 (1998)

[64] M Christen, *Sensors and Actuators*, **4**, 555 (1983)

[65] O Buu, Private correspondence

[66] J C H Zeegers, A Th A M de Waele and H M Gijsman, *J. Low Temp. Phys.*, **84**, 37 (1991)

[67] A M Guenault, T R Nichols and G R Pickett, *J. Low Temp. Phys.*, **81**, 179 (1990)

[68] E P Bashkin, *Adv. Phys.*, **30**, 1 (1981)

[69] A E Meyerovich, *Prog. Low Temperatur.*, **11**, 1 (1987)

[70] H H Jensen, H Smith, P Wolfle, K Nagai and T M Bisgaard, *Journ. Low Temp. Phys.*, **41**, 473 (1980)

[71] A Kundt and E Warburg, *Ann. Physik*, **155**, 337 (1875)

[72] D T Sprauge, T M Haard, J B Kycia, M R Rand, Y Lee, P J Hamot and W P Halperin, *Phys. Rev. Lett.*, **77**, 4568 (1996)

[73] H Götz and G Eska, *The 23rd International Conference on Low Temperature Physics* LT23, (2002)

[74] P Skyba, M Bartkowiak, Private correspondence